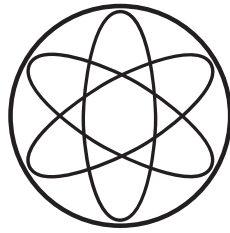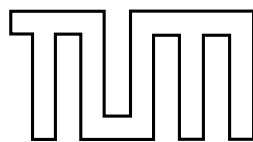Physik Department

Dissertation

Light Dark Matter in Theory and Experiment

by

Martin Wolfgang Winkler

TECHNISCHE
UNIVERSITÄT
MÜNCHEN

TECHNISCHE UNIVERSITÄT MÜNCHEN

T30e Theoretische Astroteilchenphysik

Light Dark Matter in
Theory and Experiment

Martin Wolfgang Winkler

Vollständiger Abdruck der von der Fakultät für Physik der Technischen Universität München zur Erlangung des akademischen Grades eines

Doktors der Naturwissenschaften

genehmigten Dissertation.

Vorsitzender:	Univ.-Prof. Dr. Stefan Schönert
Prüfer der Dissertation:	1. Univ.-Prof. Dr. Michael Ratz
	2. Univ.-Prof. Dr. Andrzej J. Buras, i.R.

Die Dissertation wurde am 14.08.2012 bei der Technischen Universität München eingereicht und durch die Fakultät für Physik am 29.08.2012 angenommen.

Abstract

The existence of dark matter in the universe is well-established, but its nature still remains unknown. Various ongoing experiments aim at detecting the constituents of dark matter directly via the recoil originating from their scattering off nuclei. The measured nuclear recoil rates which exhibit first hints for light weakly interacting particles with a mass of around 10 GeV (light WIMPs) shall comprehensively be analyzed in this thesis. Further, the data of the neutrino telescope Super-Kamiokande and the antiproton detector BESS-Polar II are investigated in view of signals for secondary particles from the annihilation of dark matter in the sun and the galactic halo. The fact that no indications are found is used to derive strong constraints on theoretical models. Finally, a supersymmetric extension of the Standard Model of particle physics is introduced which offers a candidate for the light WIMPs possibly detected in the above-mentioned experiments.

Zusammenfassung

Die Existenz Dunkler Materie im Universum gilt heute als bewiesen, deren Natur ist aber noch immer unbekannt. Ziel verschiedener derzeit laufender Experimente ist es, die Konstituenten der Dunklen Materie direkt mittels des Rückstoßes nachzuweisen, der bei ihrer Streuung an Atomkernen entsteht. Die dort gemessenen Streuraten, die erste Hinweise auf schwach wechselwirkende Teilchen mit einer Masse von etwa 10 GeV (leichte WIMPs) aufweisen, werden in dieser Dissertation umfassend analysiert. Zudem werden die Daten des Neutrinoteleskops Super-Kamiokande sowie des Antiproton-Detektors BESS-Polar II auf Sekundärteilchen hin untersucht, die bei der Annihilation Dunkler Materie in der Sonne und im galaktischen Halo entstehen. Die Abwesenheit solcher Signale führt auf eine strenge Einschränkung theoretischer Modelle. Zuletzt wird eine supersymmetrische Erweiterung des Standardmodells der Teilchenphysik eingeführt, die einen Kandidaten für die leichten WIMPs enthält, die möglicherweise in den oben genannten Experimenten nachgewiesen wurden.

Contents

CONTENTS

Chapter 1

Introduction

The origin of dark matter is one of the great mysteries of our present time. Since it was first proposed by Jan Oort in 1932 [1] overwhelming evidence for its existence has been collected. Today, we know that dark matter affects the kinematics of stars, galaxies and galaxy clusters and that it played a major role in the formation of structure. However, the presence of dark matter is established solely on gravitational grounds, its nature still remains a secret. In one of the most plausible scenarios, the role of dark matter is played by a stable particle with weak scale interactions and mass (WIMP) [2–4]. As we shall discuss in detail, the abundance of WIMPs from thermal production in the early universe would rather naturally match the dark matter abundance. While WIMP candidates are absent in the Standard Model of particle physics, they exist in some of its most attractive extensions. In the supersymmetric version of the Standard Model [5] the field content gets augmented by new superparticles. The lightest of these, the LSP, is protected against decay by a discrete symmetry [6] and perfectly matches the prerequisites of a WIMP.

Within the last two decades great efforts were made to directly detect WIMPs by their interactions with ordinary matter. Several dedicated experiments aim at measuring the tiny amount of recoil energy stemming from WIMP scattering off nuclei. Recently, three of these – DAMA [7, 8], CoGeNT [9, 10] and CRESST [11] – have reported signals which seem to hint at the existence of rather light WIMPs with masses of a few GeV. This interpretation is, however, challenged by the experiments XENON [12, 13], CDMS [14, 15] and SIMPLE [16, 17] which have reported scattering rates consistent with their expected backgrounds. In this work we perform a comprehensive analysis including all relevant direct detection data sets. We systematically determine the associated confidence regions and exclusion curves in the WIMP parameter space. For this, we take into account recent updates from the collaborations, e.g. a newly found contamination of the CoGeNT data by so-called surface events [18]. Assuming standard spin-independent elastic WIMP scattering we find that the confidence regions corre-

sponding to the DAMA, CoGeNT and CRESST signals are intriguingly close although they do not perfectly match. Furthermore, the null searches seem to exclude at least the DAMA and the CRESST favored regions. We comment on the possibility that the tension may be resolved by experimental and/or astrophysical uncertainties, and also consider possible non-standard WIMPs with isospin violating couplings [19, 20].

We then study the indirect detection of dark matter. Galactic WIMPs on their passage through the sun may scatter off nuclei and get gravitationally trapped [21]. Subsequent annihilation of the captured WIMPs induces daughter particles which are typically instantly stopped through their interactions with ordinary matter. If, however, neutrinos are among the annihilation products, they escape from the interior of the sun and are detectable by earth-bound neutrino telescopes (see e.g. [22, 23]). We extend the existing formalism of WIMP capture and annihilation in the sun [21, 24–26] by including the case of velocity suppressed annihilation which is especially relevant for the Majorana fermions of supersymmetric theories. We perform a model-independent analysis taking into account all relevant dark matter annihilation channels and investigate the corresponding neutrino signals at Super-Kamiokande. We concentrate on event types in which the incoming neutrino induces a muon which is stopped inside the detector volume. This class of events has not been considered previously in the dark matter context, but is particularly sensitive to light WIMPs. As we find no indications for a WIMP signal in the data, we set constraints on the WIMP nucleon cross section which are competitive to those from direct searches, especially for leptonic annihilation.

In order to gain sensitivity to the hadronic channels, we turn to WIMP annihilation in the galactic halo. If the annihilation products of dark matter include quarks, these would contribute to the antiproton flux in cosmic rays [27]. The galactic background of antiprotons originates from the spallation of primary cosmic rays (protons and helium) on the interstellar matter [28]. Due to its purely secondary origin, it is suppressed such that the detection prospects for a dark matter induced primary component are quite promising. While earlier studies have not found any indications of primary antiprotons (see e.g. [29, 30]), a new dedicated search which was recently performed by the BESS-Polar II collaboration [31] suggests a reanalysis. Due to the high precision of the released data, we decided to reevaluate the secondary antiproton background taking into account recent updates on the cosmic ray propagation parameters [32] as well as on the antiproton production cross sections [33]. We find the BESS-Polar II results to be consistent with a purely secondary origin of antiprotons. This fact is used to derive strong limits on the annihilation cross section of dark matter. In combination with the constraints from Super-Kamiokande these exclude thermal WIMPs as the origin of the DAMA, CoGeNT and CRESST signals, unless they dominantly annihilate into electrons or muons, or their annihilation cross section is velocity suppressed.

Finally, we want to clarify whether light WIMPs can be accommodated in supersymmetric extensions of the Standard Model. Within the minimal supersymmetric model

(MSSM) only the bino, the superpartner of the weak hypercharge boson, can be as light as a few GeV [34]. But its interaction strength is insufficient to give rise to a thermal annihilation cross section and to the mentioned direct dark matter detection signals (see e.g. [35]). Therefore, we introduce an extension of the MSSM by a singlet superfield which is only weakly coupled to the MSSM sector. A striking prediction in this scheme is the existence of a light scalar which resembles the Standard Model Higgs boson apart from its mass and an overall suppression factor of its interactions. The singlet fermion naturally plays the role of light dark matter. Its cross section with nucleons, mediated by the light scalar, is in the correct range to explain the DAMA, CoGeNT and CRESST signals. Annihilations within the singlet sector ensure that the singlino relic density matches the dark matter density. We verify that the scenario is consistent with constraints from flavor physics, collider searches as well as indirect dark matter detection.

This thesis is organized as follows: in chapter 2 we review the evidence for dark matter, introduce WIMPs as possible candidates and study the properties of the galactic dark matter halo. In chapter 3 the concept of direct dark matter detection is discussed, the relevant experiments are described and their data are analyzed. The hints for light WIMPs and the tension between experiments with a signal and the null searches is examined. In chapter 4 we study indirect dark matter detection where we focus on the possible neutrino and antiproton signals from WIMP annihilation in the sun and the galactic halo. We derive strong constraints on the WIMP cross sections. In chapter 5 Supersymmetry and the MSSM are introduced. Then the above-mentioned extension with singlet fermions as light dark matter is studied.

Parts of this thesis have been published in the following articles:

Improved Constraints on Inelastic Dark Matter,
K. Schmidt-Hoberg and M. W. Winkler, JCAP 09 (2009), arXiv:0907.3940 [astro-ph.CO].

Light dark matter in the singlet-extended MSSM,
R. Kappl, M. Ratz and M. W. Winkler, Phys. Lett. B695 (2011), arXiv:1010.0553 [hep-ph].

New Limits on Dark Matter from Super-Kamiokande,
R. Kappl and M. W. Winkler, Nucl. Phys. B850 (2011), arXiv:1104.0679 [hep-ph].

Dark Matter after BESS-Polar II,
R. Kappl and M. W. Winkler, Phys. Rev. D85 (2012) , arXiv:1110.4376 [hep-ph].

Chapter 2

WIMPs as Dark Matter

It is strongly believed that at an early stage the universe went through a period of inflation [36] – a very rapid expansion driven by the potential energy stored in a scalar field called the inflaton. Once the inflaton decayed, a hot and dense plasma of particles was created which contained the quarks, leptons, gauge and Higgs bosons as well as possible exotic particles predicted in extensions of the Standard Model. Due to the high temperature the particles were in thermal equilibrium unless their couplings were highly suppressed.

During its subsequent expansion the universe cooled down and went through a series of phase transitions. At a temperature $T \sim 250$ GeV the breaking of the electroweak symmetry occurred and particles acquired their mass through the Higgs mechanism. Later, at $T \sim 200$ MeV, color confinement led to the binding of quarks in color singlet states, the baryons and mesons. The formation of light elements in the primordial nucleosynthesis followed at $T \sim 1$ MeV. Finally, at $T \sim 1$ eV, matter decoupled from radiation and the first atoms were formed.

If an additional stable particle was present in the thermal bath, the evolution of its number density would depend on the strength of its interactions. After summarizing the evidence for dark matter, we will describe the Boltzmann formalism to calculate the relic density of stable a species. We will determine the cross section at which a particle can account for the dark matter as a function of its mass. Then, we will revisit the properties of the galactic dark matter halo.

2.1 Observation of Dark Matter

The existence of dark matter was first proposed by Jan Oort in 1932 [1]. The dutch astronomer had measured the motion of stars in the Milky Way by examining the Doppler shifts in their emission spectra. Their velocities turned out to be higher than expected if only luminous matter contributed to the gravitational force acting on them. Oort

inferred that some additional non-luminous mass component was present in our galaxy. A similar conclusion on the scale of galaxy clusters was drawn one year later by Fritz Zwicky. He had analyzed the velocities of galaxies in the Coma cluster and – by applying the viral theorem – found that the dynamical mass of the cluster was ~ 400 times higher than the luminous mass [37].

New hints for the existence of dark matter arose in the 1960s and 70s especially due to the pioneering work of Vera Rubin and Albert Bosma (see e.g. [38]). The two astronomers performed a systematic measurement of the circular velocities of stars in several spiral galaxies. They illustrated their results in form of galaxy rotation curves similar to the one shown in figure 2.1.
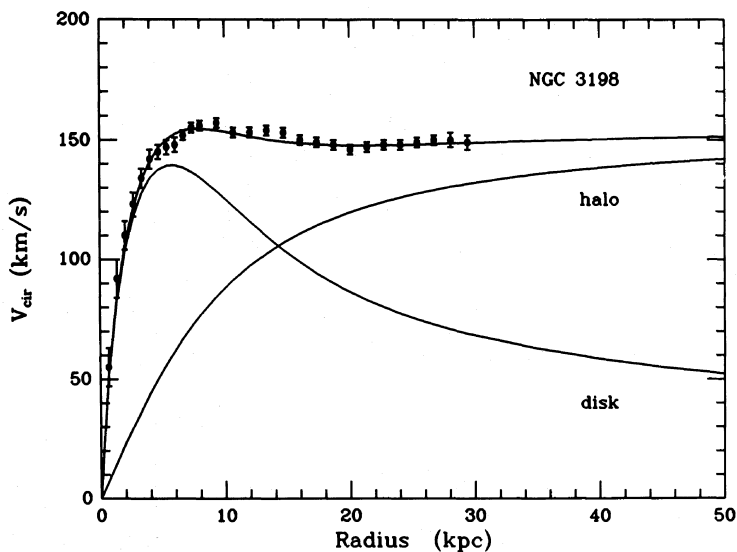
Figure 2.1: Rotation curve for the spiral galaxy NGC 3198. The image was taken from [39].

The rotation curves revealed that the circular velocity v_{cir} of stars far away from the galactic center does not significantly decrease with their distance r. Naively, one would have expected v_{cir} to scale as $v_{cir} \propto 1/\sqrt{r}$ in the outer regions of the galaxies where the density of stars is negligible. The flatness of the rotation curves thus suggests the presence of a dark matter halo which extends further in the galaxy than the luminous matter.

While dark matter offers a simple explanation to these observations, alternative concepts which invoke a modification of Newtonian gravity have been proposed [40]. The study of colliding galaxy clusters through gravitational lensing has clearly decided the case in favor of dark matter [41, 42]. Figure 2.2 is an X-ray image of 1E0657-558 (Bullet Cluster) which shows two colliding galaxy clusters. Overlaid is the distribution of mass obtained from weak lensing. It can clearly be seen, that there is a mismatch between the distributions of mass and baryonic matter, the latter mainly consisting of
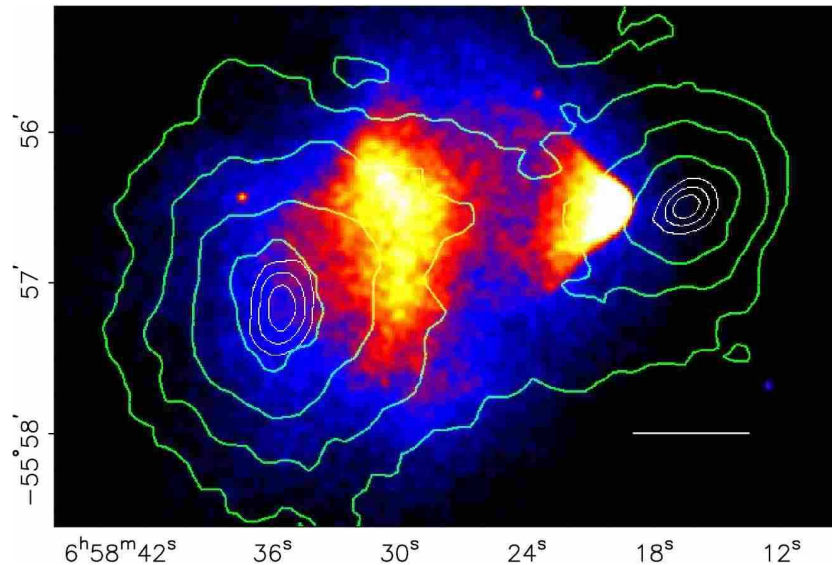
Figure 2.2: Image of the merging cluster 1E0657-558 (Bullet Cluster) from the Chandra X-ray telescope. The contours trace the distribution of mass obtained from weak lensing [42].

the gas clouds seen in X-ray. The dark matter and the stars of the clusters have simply traversed each other, while the gas clouds were slowed down by the friction arising from their interactions.

The observations described so far can consistently be explained by the presence of dark matter on all cosmological scales, however, they leave its nature unknown. After the measurement of the rotation curves, there still existed the possibility that dark matter was baryonic. After all, baryons must not necessarily contribute to the luminous matter. There were e.g. speculations about a high population of so-called brown dwarfs, celestial bodies with a mass slightly too low to trigger nuclear burning. This possibility is now disfavored: searches for such objects using gravitational lensing found an insufficient number of them to account for the dark matter [43–45].

Clear evidence that dark matter is dominantly non-baryonic came from measurements of the cosmic microwave background (CMB) as well as the light element abundances. The CMB provides us with a snapshot of the universe at the time of last scattering. The CMB photons follow – almost perfectly – a Planck distribution of temperature 2.7 K. Small fluctuations in the distribution at the level of 10^{-5}, however, encode important information about the energy content of the universe. In the standard picture of cosmology they ultimately stem from quantum fluctuations in the inflaton field which were stretched to astrophysical scales during inflation [46]. When the inflaton decayed these were converted into density fluctuations of matter and radiation. Baryons and photons formed a strongly coupled fluid, inhomogeneities evolved by acoustic oscillations and collisionless damping [47]. The CMB photons inherited the density inhomogeneities in form of energy or temperature fluctuations. In this context the Sachs-Wolf effect

plays an important role: photons coming from a region with higher density were more redshifted as it took energy to overcome the potential well [48]. The CMB fluctuations were first detected by the COBE satellite in 1993 [49], high precision data were later collected by its successor WMAP [50] which was operating between 2001 and 2010. Important measurements of the fluctuations at small angular scale were also performed by ground based detectors like ACBAR [51] and QUaD [52].

To obtain a quantitative measure of the CMB fluctuations one decomposes the temperature field $T(\hat{n})$ into spherical harmonics Y_{lm}

$$T(\hat{n}) = \sum_{l=0}^{\infty} \sum_{m=-l}^{l} a_{lm} Y_{lm}(\hat{n}) , \tag{2.1}$$

where $\hat{n}$ denotes the unit direction vector. The power spectrum is defined by the multipole moments

$$C_l^{TT} = \frac{1}{2l+1} \sum_{m=-l}^{l} |a_{lm}|^2 . \tag{2.2}$$

The index l of the multipole moment is closely related to the (angular) scale of perturbations, a large l corresponds to a small scale and vice versa. Assuming standard cosmology the shape of the power spectrum is entirely fixed by a handful of parameters. These include the total energy density of the universe Ω_{tot} as well as the dark matter and the baryon densities Ω_{DM} and Ω_{b}. By convention these are expressed as fractions of the critical density for which the universe is flat. The WMAP collaboration published the following values for the energy densities [53]

$$\Omega_{\text{tot}} = 1.0023^{+0056}_{-0054} , \tag{2.3a}$$

$$\Omega_{\text{b}} = 0.0456 \pm 0.0016 , \tag{2.3b}$$

$$\Omega_{\text{DM}} = 0.227 \pm 0.014 . \tag{2.3c}$$

These numbers are based on their CMB analysis in combination with searches for baryon acoustic oscillations by the Sloan Digital Sky Survey [54] and with measurements of the Hubble parameter [55]. They suggest that the universe is flat or very close to flat. Baryons contribute only weakly to the total density, dark matter makes up a significant part, but the dominant component of the universe is vacuum energy. This is consistent with observations of distant supernovae which indicate an accelerated expansion of our universe [56, 57]. Figure 2.3 depicts the CMB power spectrum measured by WMAP and ground based detectors. The solid line corresponds to the best-fit choice for the cosmological parameters. The dependence of the power spectrum on the cosmological parameters is highly non-trivial. Nevertheless, some qualitative remarks are in order: the position of the first peak at $l \sim 200$ is related to the angular size of the horizon at last
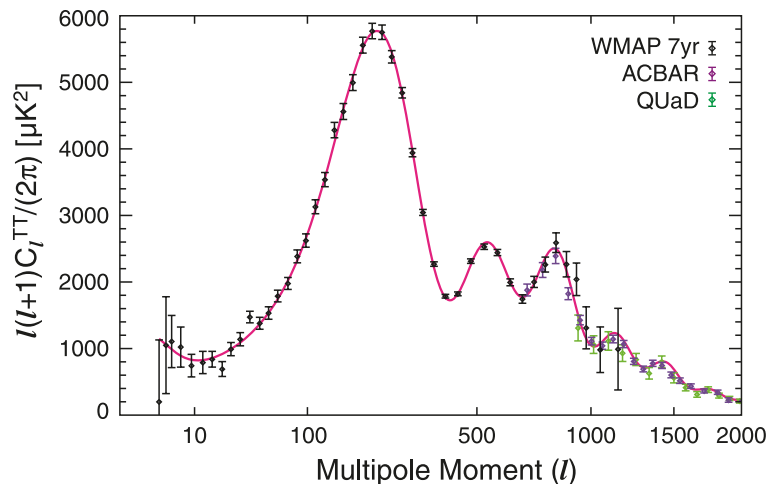
Figure 2.3: The WMAP 7-year temperature power spectrum along with the temperature power spectra from the ACBAR and QUaD experiments [58].

scattering. It is a good tracer of the geometry and thus the total density of the universe. The higher peaks corresponding to smaller cosmological scales are very sensitive to the baryon to photon ratio. Modes with small wavelength started oscillating first, i.e. already during the time when the universe was radiation dominated. They were thus subject to gravitational driving: during the compression phase photons generated their own gravitational potential which decayed away at the subsequent expansion, leading to an enhancement of the amplitude. Baryons on the other hand tend to suppress small scale oscillations through the Silk damping [47]. A higher baryon density would thus imply a reduced power in the higher peaks. An important difference between dark matter and baryons is that perturbations in baryons cannot grow before the decoupling from photons, while those in dark matter increase as soon as the universe is matter dominated. The high power in the third peak indicates that dark matter dominates over baryons.

Additional evidence for non-baryonic dark matter comes from primordial nucleosynthesis (BBN). When the universe had a temperature $T \sim 1\,\mathrm{MeV}$, free neutrons and protons formed deuterium, helium and lithium. Most free neutrons were bound in ^{4}He, the energetically most favorable configuration. The production of the other light elements is, however, very sensitive to the baryon density. Figure 2.4 compares the measured abundances with the theoretical prediction as a function of Ω_b. It can be seen that – consistent with the CMB observations – the relative element abundances indicate a baryon density of only $\Omega_\mathrm{b} h^2 \sim 0.02$ where $h \simeq 0.71$ [54]. A higher baryon density would have delayed the freeze-out of several nuclear reactions which is inconsistent with the large amount of primordial deuterium.
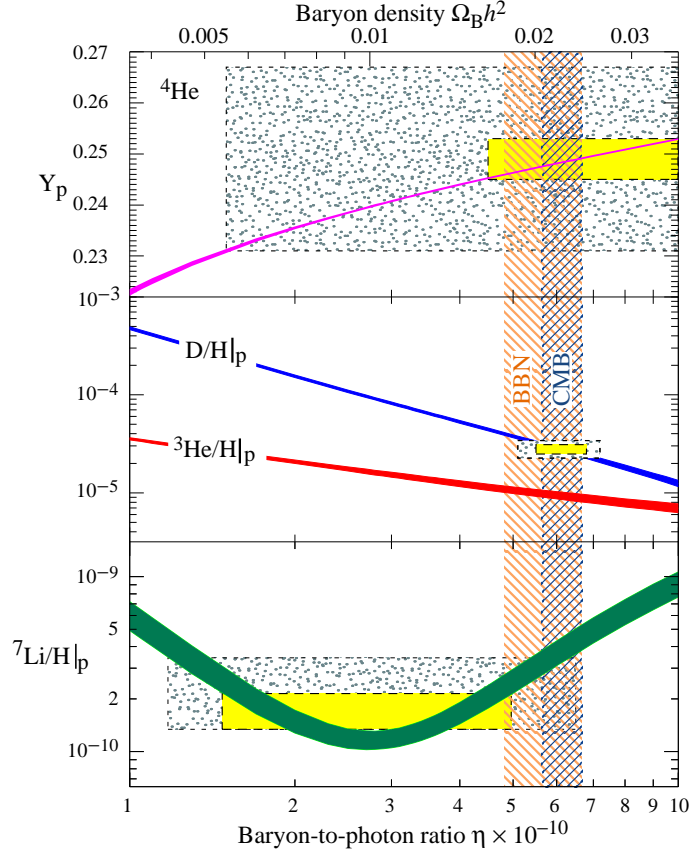
Figure 2.4: The abundances of the light elements as a function of the baryon density. The boxes depict the 2σ envelopes of the measured abundances (small boxes consider only the statistical error, large boxes the statistical and systematic errors). The bars indicate the baryon density inferred from the BBN and CMB measurements respectively. The image was taken from [59].

2.2 WIMPs and Their Production

Arguably, it is among the most plausible possibilities that the dark matter is made up by a new particle species which is stable within cosmological time scales. The most prominent extensions of the Standard Model offer promising dark matter candidates, typically, their stability is guaranteed by a new symmetry. Here we will consider the case of a stable particle χ with weak scale interactions and mass, commonly called a WIMP. Given their existence, WIMPs were copiously produced during the reheating process at the end of inflation. The subsequent evolution of their number density n_χ is determined by the Boltzmann equation which can be written in the form[1] [4]

$$\dot{n_\chi} + 3Hn_\chi = -\langle \sigma v_{\rm rel} \rangle \left(n_\chi^2 - n_{\chi,\rm eq}^2 \right) , \qquad (2.4)$$

---

[1]Here we assume that χ is its own antiparticle.

The second term on the left hand side accounts for the expansion of the universe with the Hubble rate H, the term on the right hand side for particle creation and annihilation. The equilibrium density of WIMPs is given by

$$n_{\chi,\text{eq}}(T) = g_\chi \frac{m_\chi^2 T}{2\pi^2} K_2\left(\frac{m_\chi}{T}\right) , \tag{2.5}$$

where m_χ and g_χ denote the WIMP mass and internal degrees of freedom respectively. In the following we assume $g_\chi = 2$ which strictly holds for Majorana fermions. But this choice does virtually not affect the final WIMP abundance. Further, T is the temperature and K_2 the modified Bessel function of the second kind. The term $\langle\sigma v_{\text{rel}}\rangle$ stands for the thermally averaged annihilation cross section[2] which ultimately has to be fixed by the particle physics model under consideration. For most applications it can be written in terms of a velocity expansion[3], i.e.

$$\langle\sigma v_{\text{rel}}\rangle = \sigma_{\text{s-wave}} + \sigma_{\text{p-wave}}\, v_{\text{rel}}^2 + \mathcal{O}(v_{\text{rel}}^4) . \tag{2.6}$$

If the constant term $\sigma_{\text{s-wave}}$ is unsuppressed, the higher order terms can be neglected. This scenario is called s-wave annihilation. There exists, however, the possibility that $\sigma_{\text{s-wave}}$ is forbidden due to a symmetry. This case, for which the term $\propto v_{\text{rel}}^2$ dominates, is called p-wave annihilation. In the relevant time epoch the WIMP velocities follow a Maxwell-Boltzmann distribution. Using the velocity expansion (2.6) one thus finds

$$\langle\sigma v_{\text{rel}}\rangle = \sigma_{\text{s-wave}} + \frac{6\,T}{m_\chi}\sigma_{\text{p-wave}} . \tag{2.7}$$

There exist two important limits of the Boltzmann equation:

- $n_\chi\langle\sigma v_{\text{rel}}\rangle \gg H$. The annihilations proceed fast enough to keep the species in thermal equilibrium, i.e. $n_\chi = n_{\chi,\text{eq}}$.

- $n_\chi\langle\sigma v_{\text{rel}}\rangle \ll H$. Annihilation can be neglected. The number density only changes by the expansion, i.e. $n_\chi \propto a^{-3}$ with a being the scale factor of the universe.

In order to determine the WIMP density after freeze-out, one has to solve the Boltzmann equation numerically. For this purpose, it is convenient to introduce the WIMP abundance $Y_\chi = n_\chi/s$ with the entropy density

$$s = \frac{2\,\pi^2}{45}\,g_*T^3 . \tag{2.8}$$

Here, g_* is the effective number of degrees of freedom contributing to the entropy density. Assuming an adiabatic evolution of the universe, the entropy density scales as $s \propto a^{-3}$,

---

[2]Note that in this expression v_{rel} denotes the relative velocity between two WIMPs.
[3]The velocity expansion does not hold for resonant annihilation.

i.e. Y_χ is preserved after the freeze-out. Further, by using $H = -\dot{T}/T$ one can replace the time derivative by a derivative with respect to the temperature. This leads to the following form of the Boltzmann equation in terms of the WIMP abundance

$$\frac{\mathrm{d}Y_\chi}{\mathrm{d}T} = \frac{4\pi}{\sqrt{90}} M_P \sqrt{g_*(T)} \langle \sigma v_{\mathrm{rel}} \rangle \left(Y_\chi^2 - Y_{\chi,\mathrm{eq}}^2 \right) , \tag{2.9}$$

where M_P is the Planck mass. Note that g_* is itself a function of the temperature: it changes whenever particles freeze out from the background plasma or when the number of degrees of freedom is reduced by phase transitions. A recent evaluation of g_* which we use in the following can be found in [60]. In figure 2.5 we depict the solution to the Boltzmann equation for several choices of $\langle \sigma v_{\mathrm{rel}} \rangle$.
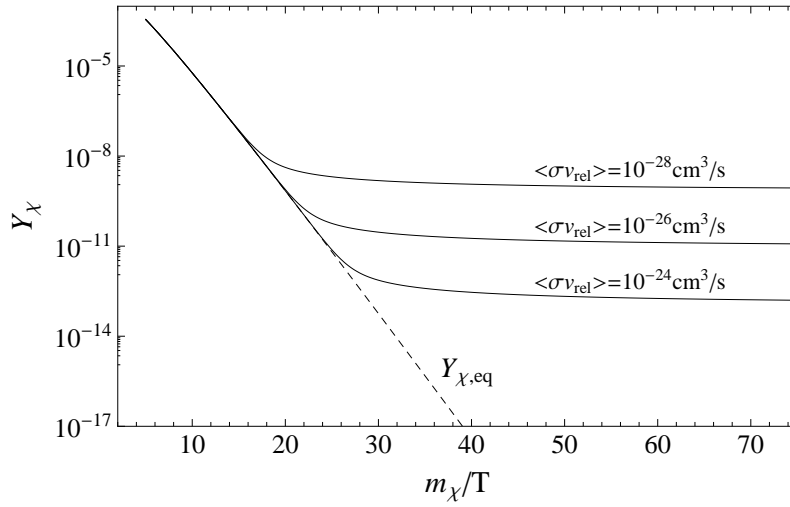
Figure 2.5: Evolution of the WIMP abundance ($m_\chi = 100\,\mathrm{GeV}$) with temperature for several choices of $\langle \sigma v_{\mathrm{rel}} \rangle$. The dashed line represents the equilibrium abundance $Y_{\chi,\mathrm{eq}}$.

It can be seen that Y_χ initially follows the equilibrium abundance and becomes fixed after the freeze-out. The final WIMP abundance $Y_{\chi,\infty}$ scales inversely with the annihilation cross section. A very precise semi-analytical approximation reads [61]

$$Y_{\chi,\infty} = \frac{1}{1.3\, m_\chi\, M_P \sqrt{g_*(T_F)} \left(\frac{T_F}{m_\chi} \sigma_{\text{s-wave}} + 3 \frac{T_F^2}{m_\chi^2} \sigma_{\text{p-wave}} \right)} . \tag{2.10}$$

The freeze-out temperature T_F is defined implicitly by [62]

$$\frac{m_\chi}{T_F} = 20.5 + \log \left(\frac{m_\chi \sqrt{\frac{m_\chi}{T_F}}}{\left(\frac{m_\chi}{T_F} - 1.5 \right) \sqrt{g_*(T_F)}} \frac{\langle \sigma v_{\mathrm{rel}} \rangle}{10^{-26}\,\mathrm{cm^3\,s^{-1}}} \right) . \tag{2.11}$$

The logarithmic term is typically suppressed, i.e. $T_F \sim m_\chi/20$. Finally, the relic density of WIMPs Ω_χ is related to $Y_{\chi,\infty}$ by

$$\Omega_\chi = \frac{m_\chi\, s_0\, Y_{\chi,\infty}}{3 H_0^2 M_P^2} \simeq 5.5 \times 10^{11} \left(\frac{m_\chi}{1\,\mathrm{TeV}} \right) Y_{\chi,\infty} . \tag{2.12}$$

Here, we have used $H_0 = 71 \, \text{km s}^{-1}/\text{Mpc}$ for the Hubble constant and $s_0 = 2900 \, \text{cm}^{-3}$ for the present entropy density [63]. Note that the WIMP density depends only on its mass and annihilation cross section. If we require that the WIMPs make up the dark matter in the universe, we can fix the cross section for a given mass. The corresponding cross section, for which $\Omega_\chi = \Omega_{\text{DM}}$, is called the thermal cross section. It is plotted for the limiting cases of pure s-wave and pure p-wave annihilation in figure 2.6.
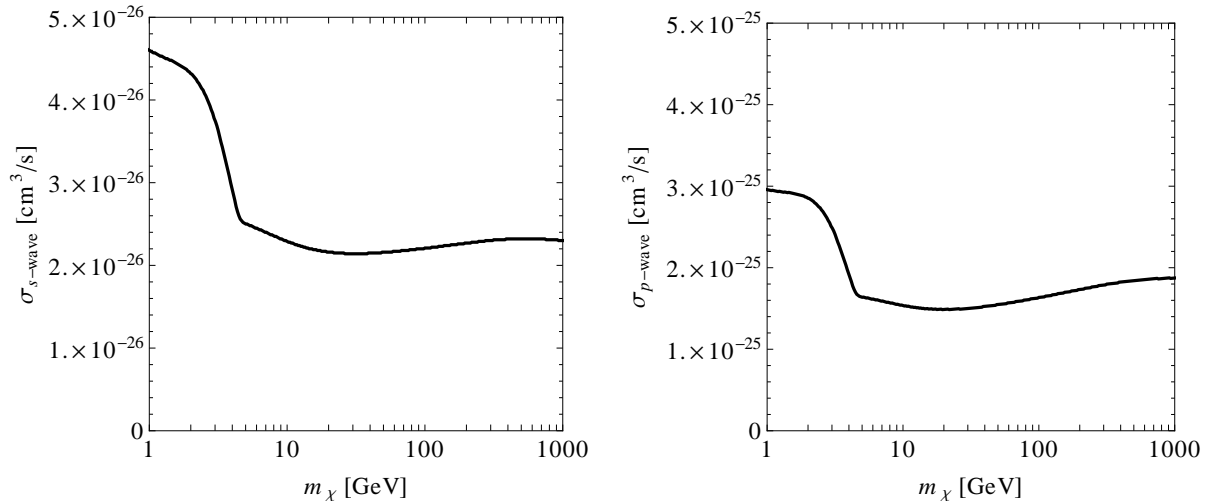
Figure 2.6: Thermal cross section for the case of s-wave annihilation (left) and p-wave annihilation (right).

2.3 The Galactic Dark Matter Halo

The seeds of galaxies were the density fluctuations in the universe which ultimately stem from the quantum fluctuations in the inflaton field, stretched by the expansion. Dark matter was a key ingredient to the formation of structure as its fluctuations started growing earlier than those in baryons, the latter being subject to Silk damping until recombination. If an overdense region exceeds the Jeans length its internal gravity overcomes the pressure and it collapses [64]. In this regime, linear perturbation theory breaks down and the subsequent evolution cannot be traced by analytical means. The mechanism of violent infall provides a qualitative explanation for the dark matter forming a halo rather than collapsing to a singularity [65]. During infall, the gravitational field changes rapidly with time. The dark matter particles experience chaotic gravitational forces. This resembles a microscopic interaction and leads to an energy exchange among them, their phase space distribution becomes well-mixed. The baryons condense in the potential wells generated by the dark matter. Due to dissipative processes they lose kinetic energy and reside closer to the galactic center than the dark matter. If they

carried initial angular momentum the movement parallel to their main rotation axis is damped and they develop disc-like structures as in the Milky Way. Only in the region close to the galactic center, the density of baryons becomes so high that they form a cusp.

Simple analytical approximations to the infall predict a galactic dark matter density profile of the form of an isothermal sphere. However, more realistic distributions are expected from dedicated N-body simulations like Millennium [66], Aquarius [67] and Via Lactea-II [68] which were performed in order to trace the dark matter on galactic scales. These seem to hint at steeper profiles like the Navarro-Frenk-White (NFW) profile [69] or the Einasto profile[4] [70]:

$$\rho_\chi(r) = \frac{\rho_s}{1 + \left(\frac{r}{r_s}\right)^2} \qquad \text{(Isothermal)}, \qquad (2.13a)$$

$$\rho_\chi(r) = \frac{\rho_s}{\frac{r}{r_s}\left(1 + \frac{r}{r_s}\right)^2} \qquad \text{(NFW)}, \qquad (2.13b)$$

$$\rho_\chi(r) = \rho_s \exp\left(-\frac{2}{0.17}\left[\left(\frac{r}{r_s}\right)^{0.17} - 1\right]\right) \qquad \text{(Einasto)}. \qquad (2.13c)$$

Here, r denotes the distance from the galactic center. The scale radius r_s and the scale density ρ_s depend on the considered profile and on the properties of the galaxy. For the case of the Milky Way, these parameters can be fixed by measuring the velocities and velocity dispersions of stars. Here we extract the scale radii from [71] and normalize the profiles such that the local dark matter density at the position of the sun ($r_\odot = 8.5$ kpc) takes the value[5] $\rho_0 = 0.39$ GeV cm^{-3}, recently found in [72] with an error of 0.02 GeV cm^{-3}. The corresponding values for ρ_s and r_s are given in table 2.1.

Profile	ρ_s [GeV/cm^3]	r_s [kpc]
Isothermal	1.86	4.4
NFW	0.247	24.4
Einasto	0.044	28.4

Table 2.1: Scale radii and scale densities for different dark matter profiles.

These were used in figure 2.7 to depict an isothermal, NFW and Einasto profile for the Milky Way. The three distributions are similar for distances $r > 4$ kpc, however, the NFW and Einasto profiles are steeper towards the galactic center. Notice that the NFW and the Einasto profiles differ substantially at distances $r \lesssim 1$ kpc. In this regime,

---

[4]Note that for the Einasto profile the exponent of r/r_s is sometimes taken to be a free parameter. Here we fix it to 0.17.

[5]We neglect here the very mild dependence of the local dark matter density on the considered profile. A similar value for ρ_0 as in the analysis by Catena et al. [72] was independently found in [73].
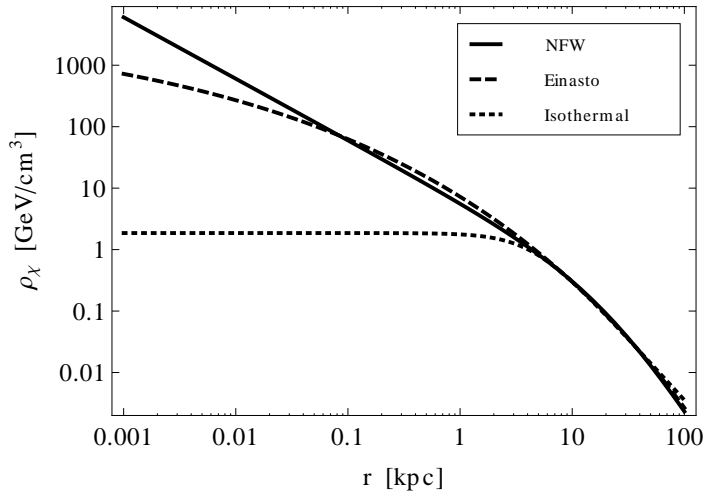
Figure 2.7: Possible dark matter profiles for the Milky Way. Scale parameters were taken from table 2.1.

large uncertainties on the density distribution exist. The results of N-body simulations are hardly trustable as they typically neglect baryons which become the dominant mass component at small distances. Further, they are limited by the resolution. This makes it difficult to predict e.g. the annihilation signals from dark matter which are expected from the center region.

On the other hand – as we shall discuss later – direct searches for dark matter are only sensitive to the local properties of the halo: the local density and the local velocity distribution $f(\vec{v})$. If one assumes that our galaxy is spherically symmetric, Eddington's formula gives a one-to-one correspondence between the dark matter density profile and its velocity distribution [74]. In the isothermal model $f(\vec{v})$ is a Maxwell-Boltzmann distribution (in the galactic rest frame) of the form

$$f(\vec{v}) = \left(\frac{3}{2\pi\sigma_v^2}\right)^{3/2} \exp\left(-\frac{3\,v^2}{2\sigma_v^2}\right) \quad \text{for} \quad v < v_{\text{esc}} . \tag{2.14}$$

In this simple model, the velocity dispersion σ_v is related to the circular velocity of the sun $v_{\odot,\text{cir}} = 220 \text{ km s}^{-1}$ [75] by $\sigma_v = \sqrt{3/2}\, v_{\odot,\text{cir}}$. The distribution is truncated at the local galactic escape velocity v_{esc}. The latter was determined to be in the interval $498 \text{ km/s} < v_{\text{esc}} < 608 \text{ km/s}$ at 90% confidence level by the RAVE survey [76]. The more advanced dark matter profiles like NFW and Einasto lead to a similar local velocity distribution as they differ from the isothermal sphere mainly in the region far away from the sun. Note also that the Maxwell-Boltzmann distribution is in good agreement with the outcome of N-body simulations (see e.g. [77]).

Chapter 3

Direct Dark Matter Searches and Hints for Light WIMPs

Up to now all evidence for the existence of dark matter is purely based on gravity. But if the dark matter is constituted by WIMPs, it is quite likely that their interaction strength with ordinary matter is sufficient to directly detect them with earth-bound detectors. Assuming a local dark matter density of $\rho_0 = 0.39\,\mathrm{GeV\,cm^{-3}}$ and velocities of a few $100\,\mathrm{km\,s^{-1}}$ the incident dark matter flux is $\sim 10^5\ \mathrm{cm^{-2}\,s^{-1}}$. For a weak scale cross section ($\sigma \sim \mathrm{pb}$) this corresponds to $\mathcal{O}(10)$ scatterings per year in a detector with a target mass of 1 kg. The recoil energy transferred to the nucleus in such a collision depends on the mass and velocity of the incoming particle, typically it is in the keV range.

In this chapter we will describe the different techniques of direct dark matter detection and the expected signals. Then we will analyze – using a similar method as in [78] – the data sets obtained by the relevant experiments and study possible hints for light dark matter particles.

3.1 Detector Types

The experimental search for dark matter is highly challenging as backgrounds exceed the expected signal by orders of magnitude. As a protection against cosmic radiation the detectors are typically placed in underground facilities like Gran Sasso or the Soudan mine where they are shielded by several kilometers of rock. But further background rejection is clearly required and various different technologies are employed. We will now briefly describe the most important classes of detectors which are used in the search for WIMPs. Comprehensive reviews can be found in [79, 80].

3.1.1 Cryogenic Detectors

The detector material of cryogenic detectors is a radiopure crystal which is run at very low temperatures. Recoiling ions dissipate their energy in a series of collisions with the electrons and ions of the crystal lattice. A large fraction of the initial kinetic energy is converted into collective excitations of the lattice. These phonons correspond to a temperature rise in the crystal of $\mathcal{O}(\mu K)$. Such tiny temperature differences can e.g. be measured by transition edge sensors. These consist of superconducting tungsten films which are operated close to the transition temperature to the conductor state where their resistance changes rapidly. Due to the scattering with electrons parts of the kinetic energy of the recoiling nucleus get transferred into ionization. If one covers the detector with electrodes, the electron hole pairs can be measured through the application of an electric field. Alternatively, one can search for the scintillation light which originates from the recombination of the deflected electrons.

The relative amount of heat, ionization and scintillation is vastly different for nuclear recoils compared to electron recoils. Therefore, cryogenic experiments aim at measuring two of the named signals. They typically use phonons for setting the energy scale of an event and the scintillation or ionization signal as a discriminator between electromagnetic background and signal. The remaining dangerous backgrounds for cryogenic detectors, which could mimic a WIMP signal, are mainly neutrons. The latter may stem from radioactive contaminations or get induced by traversing muons. To take care of them, additional shields and a muon veto are typically used.

In the last years, the search for light WIMPs gained importance and several ultra-low-energy germanium detectors were built, CoGeNT [9,10] being a prominent example. These are only sensitive to the ionization output of an event and, therefore, suffer from sizable backgrounds. Nevertheless, they have produced competitive results due to their low thresholds.

3.1.2 Liquid Noble Detectors

Similar to crystals, also targets consisting of noble liquids offer the possibility to measure recoil energies in different channels. A recoiling nucleus loses its energy by ionization and excitation of electrons. As in cryogenic detectors, the ionization output can be measured by applying an electric field. Additionally, liquid nobles are excellent scintillators. The light output from the deexcitation of atoms can be detected by photomultipliers. Liquid noble detectors use the scintillation output of an event for energy calibration and the ionization signal for discrimination of the signal against electromagnetic backgrounds. While the background rejection is less efficient compared to cryogenic detectors, the target mass can be increased much more easily than in the case of crystals.

3.1.3 Superheated Droplet Detectors

Superheated droplet detectors employ a technique very similar to the bubble chambers used in the early times of particle physics. Incident ionizing radiation leads to bubble nucleation within the droplets which are filled with superheated liquids. This causes an acoustic shock wave which is detected by piezoelectric sensors (see e.g. [16]). Bubble chambers are insensitive to gamma radiation and thus reject electromagnetic backgrounds very efficiently. A disadvantage of droplet detectors is their insensitivity to the spectral distribution of events.

3.2 The Recoil Spectrum

As we discussed, direct detection experiments aim to measure the deposited energy of a WIMP when it interacts with a nucleus in the detector. Let us now discuss the event rate in some detail.

3.2.1 The Event Rate

A WIMP which scatters off of a target nucleus transfers the recoil energy

$$E_R = \frac{\mu_N^2 \, v^2 \, (1 - \cos\theta)}{m_N} \; , \tag{3.1}$$

where $\mu_N = m_\chi m_N / (m_\chi + m_N)$ is the WIMP nucleus reduced mass, m_N the nucleus mass, θ the scattering angle in the center of mass frame and v the WIMP velocity. Unless the mediator is massless, the momentum transfer between WIMP and nucleus in the propagator can be neglected. This implies that the WIMP nucleus scattering can be viewed as a contact interaction, and the cross section is independent of the scattering angle. However, one has to account for losses of coherence due to the nucleus not being a point-like particle. This is encoded in the so-called form factor $F(E_R)$. By use of (3.1) we can express the differential WIMP nucleus cross section as

$$\frac{\mathrm{d}\sigma_N}{\mathrm{d}E_R} = \frac{m_N}{2 \, \mu_N^2 \, v^2} \, \sigma_N \, F^2(E_R) \; . \tag{3.2}$$

Here σ_N denotes the cross section at zero momentum transfer. The differential scattering rate of WIMPs at a target with mass M_{tar} can then be written as [81]

$$\frac{\mathrm{d}R}{\mathrm{d}E_R}(E_R, t) = M_{\mathrm{tar}} \frac{\rho_0}{2 \, m_\chi \mu_N^2} \, \sigma_N \, F^2(E_R) \int\limits_{v_{\mathrm{min}}}^{\infty} \mathrm{d}^3 v \, \frac{f_{\mathrm{earth}}(\vec{v}, t)}{v} \; . \tag{3.3}$$

As discussed in section 2.3, we assume a local dark matter density $\rho_0 = 0.39 \; \mathrm{GeV \, cm^{-3}}$, and further a Maxwellian form of the velocity distribution $f(\vec{v})$ in the galactic rest frame

(c.f. (2.14)). The distribution in the earth rest frame can be obtained by a Galilean boost,

$$f_{\text{earth}}(\vec{v}, t) = f(\vec{v} + \vec{v}_{\text{earth}}(t)) . \tag{3.4}$$

The velocity of the earth relative to the galactic center can be parameterized as

$$\vec{v}_{\text{earth}}(t) = \vec{v}_{\text{sun}} + \vec{v}_{\text{an}}(t) . \tag{3.5}$$

Using the convention for galactic coordinates as in [82] we can write

$$\vec{v}_{\text{sun}} \simeq \begin{pmatrix} 0 \\ 220 \\ 0 \end{pmatrix} \text{km/s} + \begin{pmatrix} 10 \\ 5.2 \\ 7.2 \end{pmatrix} \text{km/s} \tag{3.6}$$

describing the motion of the solar system [75, 83] and

$$\vec{v}_{\text{an}}(t) \simeq 29.8 \, \text{km/s} \left[\begin{pmatrix} 0.9931 \\ 0.1170 \\ -0.01032 \end{pmatrix} \cos\left(2\pi(t - t_1)\right) + \begin{pmatrix} -0.0670 \\ 0.4927 \\ -0.8678 \end{pmatrix} \sin\left(2\pi(t - t_1)\right) \right] \tag{3.7}$$

parameterizing the time-dependent velocity of the earth relative to the sun [81,82]. Here t is measured in years and $t_1 = 0.219$ corresponds to the spring equinox on March 21. The maximal and minimal velocities of the earth with respect to the galactic rest frame are reached on June 2 and December 2 respectively.

3.2.2 Cross Section and Form Factors

We should now take a closer look at the cross section of WIMPs with nuclei. It is convenient to split the cross section and the form factor into a spin-dependent (SD) and a spin-independent (SI) part, i.e.

$$\sigma_N F^2(E_R) = \sigma_N^{\text{SI}} F_{\text{SI}}^2(E_R) + \sigma_N^{\text{SD}} F_{\text{SD}}^2(E_R) . \tag{3.8}$$

Scalar and vector interactions contribute to σ_N^{SI}, pseudoscalar and axialvector interactions to σ_N^{SD}. In order to compare dark matter searches with different target materials one needs to express σ_N in terms of the WIMP proton cross section σ_p. In the case of spin-independent scattering the contributions to σ_N from the individual nucleons add coherently and one finds

$$\sigma_N^{\text{SI}} = \frac{\mu_N^2}{\mu_p^2} \left(\frac{Z f^p + (A - Z) f^n}{f_p} \right)^2 \sigma_p^{\text{SI}} , \tag{3.9}$$

where μ_p denotes the WIMP proton reduced mass[1], Z and A the proton and mass numbers of the nucleus, f_p and f_n the effective (spin-independent) WIMP couplings to protons and neutrons respectively. In a large class of models one has $f_p = f_n$ and the term in brackets simplifies to A^2. This is e.g. the case if the WIMP nucleon interaction is mediated by a Higgs-like scalar. The latter would mainly couple to the strange quark and gluon content of the nucleon which is identical for protons and neutrons. We will, therefore, mostly concentrate on the case $f_n = f_p$. As all nuclei have roughly the same ratio of protons to neutrons, isospin violating couplings $f_p \neq f_n$ typically affect all experiments in a similar way. Only if there are strong cancellations between the proton and neutron contribution to σ_N, i.e. if $f_n \sim -f_p$, the exact composition of the nucleus becomes relevant. In this case the sensitivity of an experiment depends strongly on its target material, we will later discuss this possibility separately.

If we turn to spin-dependent interactions, the WIMP couples to the total neutron and proton spin of the nucleus. The WIMP nucleus cross section reads [84]

$$\sigma_N^{\text{SD}} = \frac{\mu_N^2}{\mu_p^2} \left(\frac{a_p \langle S_p \rangle + a_n \langle S_n \rangle}{a_p} \right)^2 \frac{4}{3} \frac{J+1}{J} \sigma_p^{\text{SD}} , \qquad (3.10)$$

where a_p and a_n are the effective (spin-dependent) WIMP proton and WIMP neutron couplings, $\langle S_p \rangle$ and $\langle S_n \rangle$ the proton and neutron spin expectation values in the nucleus and J the total nuclear spin. It depends critically on the relative coupling a_p/a_n which is the most suitable target material to search for spin-dependent interactions. This is because – depending on the size of $\langle S_p \rangle$ and $\langle S_n \rangle$ – enhancements or cancellations in the cross section can occur for certain combinations of a_p and a_n. A rule of thumb is that nuclei with an uneven number of protons (neutrons) are especially sensitive to WIMP proton (neutron) couplings.

Note also that in the spin-dependent case there is no coherent enhancement of the WIMP nucleus cross section with the number of nucleons, i.e. heavy target materials like germanium or xenon are not favored. Nevertheless, the search for spin-dependent interactions should not be neglected as there exist theoretical models which predict $\sigma_p^{\text{SD}} \gg \sigma_p^{\text{SI}}$.

For spin-independent scattering we use the Fourier-Bessel parametrization of the form factors, the coefficients are taken from [85,86]. If, for a certain nucleus, the Fourier coefficients have not been determined, we use Woods-Saxon form factors with the parameters from the same reference. Note that the commonly used Helm form factors are less accurate than those employed here [87]. In the spin-dependent case, the form factors depend on the nuclear structure functions S_{00}, S_{01}, S_{11} and on the couplings a_p, a_n:

$$F_{\text{SD}}^2(E_R) = \frac{(a_p + a_n)^2 S_{00}(E_R) + (a_p^2 - a_n^2) S_{01}(E_R) + (a_p - a_n)^2 S_{11}(E_R)}{(a_p + a_n)^2 S_{00}(0) + (a_p^2 - a_n^2) S_{01}(0) + (a_p - a_n)^2 S_{11}(0)} . \qquad (3.11)$$

---

[1]We neglect the small mass difference between proton and neutron.

22

A model-based evaluation of S_{00}, S_{01}, S_{11} can be found in [88].

3.2.3 Annual Modulation

As discussed in section 3.1, several dark matter experiments distinguish nuclear from electromagnetic recoils which drastically reduces the background in the search for WIMPs. There exists, however, another distinctive feature of the WIMP signal which one can use to discriminate it from possible backgrounds: the motion of the earth around the sun leads to an annual modulation in the WIMP velocity distribution with respect to the earth (see figure 3.1). Assuming a Maxwellian form of $f(\vec{v})$ in the galactic rest frame, the differential rate of WIMP scattering has a constant and a nearly sinusoidal time-dependent contribution,

$$\frac{\mathrm{d}R}{\mathrm{d}E_R}(E_R, t) = S_0(E_R) + S_m(E_R) \cos\left(2\pi(t - t_0)\right) , \tag{3.12}$$

where the phase t_0 corresponds to June 2.
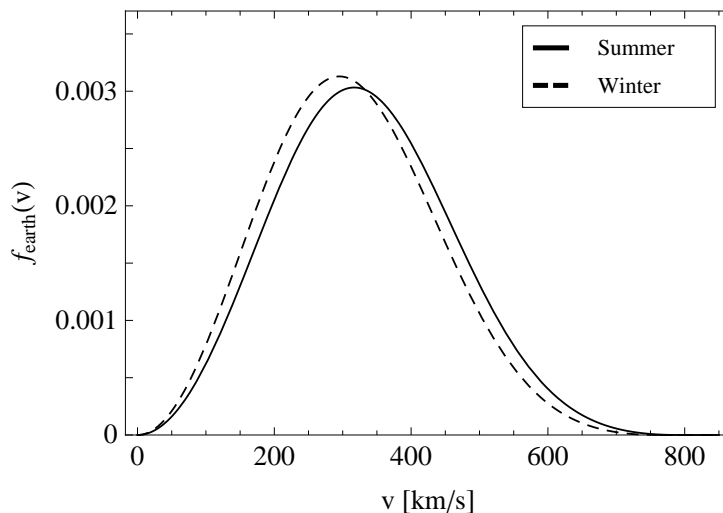
Figure 3.1: Velocity distribution of dark matter in the earth rest frame in summer (June 2) and winter (December 2).

Depending on the scattering energy, there may occur either a maximum or a minimum at t_0, implying either a positive or a negative modulation amplitude S_m. The latter can be defined as

$$S_m(E_R) = \frac{1}{2} \left(\frac{\mathrm{d}R}{\mathrm{d}E_R}(E_R, t_0) - \frac{\mathrm{d}R}{\mathrm{d}E_R}(E_R, t_0 + 0.5\,\mathrm{yr}) \right) . \tag{3.13}$$

For a Maxwellian velocity distribution, the modulation fraction S_m/S_0 is typically at the level of a few per cent. Note, however, that for non-standard velocity distributions, which have additional features, the time dependence could in principle have a more complicated non-sinusoidal form and the modulation fraction could be enhanced.

3.2.4 Detector Effects

The interpretation of data from direct dark matter searches requires the inclusion of detector effects. First of all, only a fraction of the recoil energy E_R is transferred into visible energy E', i.e.

$$E' = Q\,E_R \; . \tag{3.14}$$

The conversion factor Q – typically called the quenching factor – depends on the target material and on the channel which is used to detect the energy of an event, e.g. ionization or scintillation. Some experiments present their results already in terms of recoil energy by rescaling with the quenching factor. This may, however, not be possible if the detector consists of multiple target materials. In any case, it is very important to be aware of the distinction between E_R and E'.

Another aspect of realistic detectors is their finite energy resolution. The measured energy follows a probability distribution around the expected recoil energy. Typically, the distribution can be approximated by a Gaussian with an energy dependent standard deviation $\sigma(E')$. The differential event rate corrected by the resolution can thus be obtained as

$$\frac{\mathrm{d}R}{\mathrm{d}E'}_{\text{corrected}}(E',t) = \int\limits_0^\infty \mathrm{d}E'' \; \frac{\mathrm{d}R}{\mathrm{d}E''}(E'',t) \; \frac{1}{\sqrt{2\pi}\sigma(E'')} \exp\left(-\frac{(E'-E'')^2}{2\sigma^2(E'')}\right) \; . \tag{3.15}$$

We should mention that this formula does not hold in case of very small statistics, i.e. if the recoil signal consists only of a few photo-electrons. For such a case, one has to replace the Gaussian by a Poisson distribution.

Finally, experiments typically perform a number of cuts to reduce the level of backgrounds. This affects the possible WIMP signal and must be considered by introducing an (energy-dependent) detector efficiency.

3.3 Analysis of Direct Searches

In this section we will analyze the data taken by direct dark matter searches. To start with, we will briefly introduce the most relevant experiments. Direct dark matter searches can be divided into two categories:

- experiments with a possible WIMP signal, i.e. DAMA, CoGeNT and CRESST,

- various null searches.

Out of the second category we will restrict our attention to those experiments which provide the strongest constraints on the WIMP nucleon cross section. These include CDMS, XENON and SIMPLE.

3.3.1 Experiments with a Signal

3.3.1.1 DAMA

DAMA's target consists of several radiopure NaI(Tl) crystals located in the Gran Sasso underground laboratory. Recoils on sodium and iodine can a priori not be distinguished. The energy of an event is measured by its scintillation output in 36 bins over the energy range $E' = 2 - 20$ keV. The collaboration has published the quenching factors $Q_I = 0.09$ and $Q_{Na} = 0.3$ for sodium and iodine nuclear recoils respectively [89], the energy resolution is given in [90]. The background rejection in the DAMA experiment is very limited, there is no separation between nuclear recoils and electromagnetic events. Therefore, DAMA is only sensitive to the annual modulation of a possible WIMP signal, the constant part is indistinguishable from backgrounds.
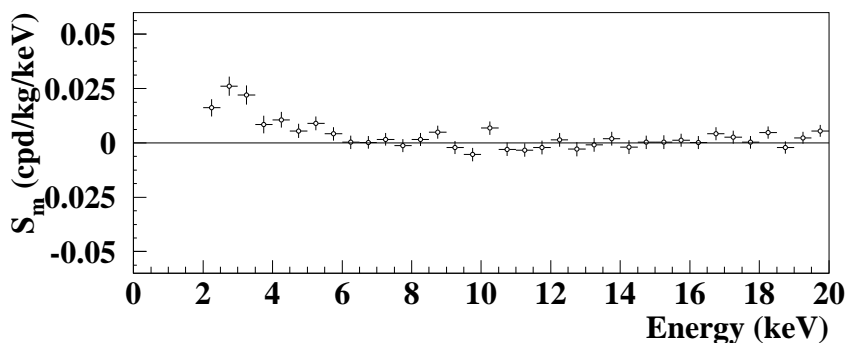
Figure 3.2: Energy distribution of the modulation amplitude S_m in the combined DAMA/NaI and DAMA/LIBRA data set. The image was taken from [91].

In this work we consider the 1.17 t yr data set accumulated over 13 annual cycles in the DAMA/NaI (1995-2002) and DAMA/LIBRA (2003-2009) runs [8]. It exhibits an annual modulation of the nuclear recoil rates which is present at a significance of $8.9\,\sigma$. The period and the phase of the signal is consistent with the scattering of WIMPs in the detector. The binned modulation amplitude and statistical error is shown in figure 3.2. It can be seen that the modulation is present in the range $E' = 2 - 6$ keV, while at higher energies the amplitude fluctuates statistically around zero.

3.3.1.2 CoGeNT

The CoGeNT detector is made up by a 440 gram high purity germanium crystal cooled to liquid nitrogen temperatures, it is located in the Soudan Underground Laboratory. Nuclear recoils are measured by their ionization output, the germanium quenching factor

was determined by the collaboration to be $[9,92]$[2]

$$Q_{\mathrm{Ge}} = 0.19935 \left(\frac{E_R}{\mathrm{keV}} \right)^{0.1204} . \tag{3.16}$$

For the energy resolution we use the scaling given in [94] with the parameters taken from [9]. Due to its low energy threshold, the CoGeNT detector is especially competitive in the search for light WIMPs. The background rejection is, however, limited to shielding and rise-time cuts which are intended to suppress surface events.
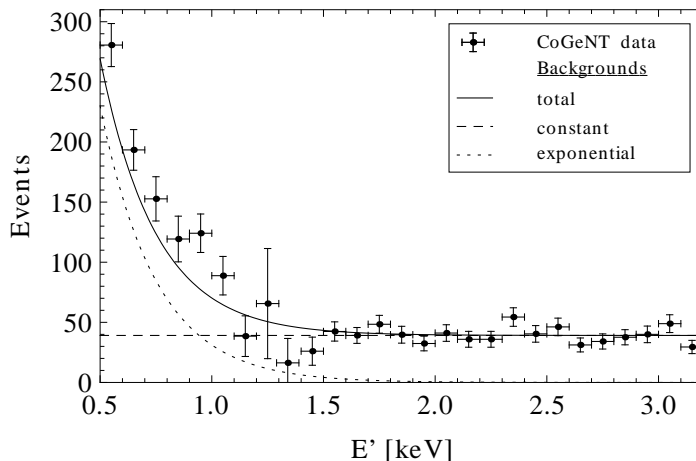
Figure 3.3: CoGeNT event spectrum after efficiency correction and subtraction of the cosmogenic lines. Also shown is the constant and the exponential background assumed in this analysis.

The current sample consists of 442 live days of data taken between December 2009 and March 2011 [10]. The recoil spectrum in the range $E' = 0.5 - 3.2$ keV is shown in figure 3.3 where the cosmogenic lines stemming from intrinsic contamination have already been subtracted. There remains a constant signal as well as an exponential rise of events towards low energies. The collaboration has speculated about a possible dark matter origin of the exponential signal in $[9,10]$. However, an improved rise-time study has revealed that at least part of the excess is explained by surface events which have not been rejected previously due to too loose cuts [18]. Based on the available experimental information (presented in $[18,95]$), we will assume a constant background of $391\,\mathrm{keV}^{-1}$ and an exponential background of $17000\,\mathrm{keV}^{-1} \times \exp(-E'/0.25\,\mathrm{keV})$. We will later determine the regions in the WIMP parameter space which could explain the remaining signal. Note, however, that the dark matter interpretation of the CoGeNT signal is rather controversial as additional sources of background e.g. from electronic noise are hard to exclude at this moment.

---

[2]Note, however, that there is an unresolved discrepancy between the quenching factor measurements of CoGeNT and CDMS (see $[15,93]$).

A time analysis of the CoGeNT events further revealed an annual modulation present at the level of $2.8\,\sigma$ [10]. In order to investigate a possible dark matter origin of the modulation one can fit a sine function to the modulated spectrum. For the phase fixed to June 2 (the prediction of an isotropic dark matter velocity distribution) this procedure leads to the modulation amplitudes [96]

$$S_m\,(0.5 - 1\,\mathrm{keV}) = (0.75 \pm 0.54)\,\mathrm{d}^{-1}\,\mathrm{kg}^{-1}\,\mathrm{keV}^{-1}\,, \tag{3.17a}$$

$$S_m\,(1 - 3.2\,\mathrm{keV}) = (0.37 \pm 0.16)\,\mathrm{d}^{-1}\,\mathrm{kg}^{-1}\,\mathrm{keV}^{-1}\,. \tag{3.17b}$$

We use only these two energy bins for the modulation analysis in order not to dilute the power of the statistical test.

3.3.1.3 CRESST II

The CRESST II cryogenic dark matter search at the Gran Sasso laboratory employed 18 crystal detectors with a mass of 300 gram [11]. Eight of them – all consisting of $CaWO_4$ – were fully operational and used in the analysis of the collaboration. A very efficient discrimination between electron and nuclear recoils is achieved by considering the scintillation to phonon ratio of an event. The current data set corresponds to an exposure of $730\,\mathrm{kg\,d}$ accumulated between 2009 and 2011.
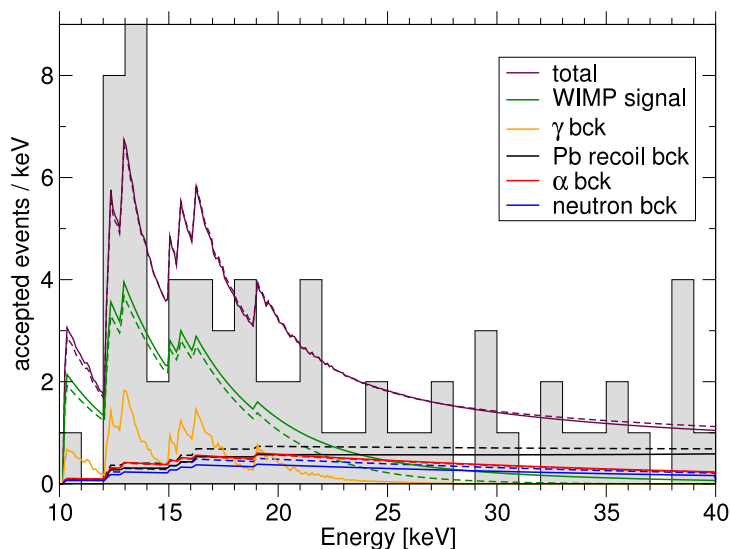
Figure 3.4: Energy spectrum of events in the signal region from all operational detector modules. Also shown are the modeled backgrounds and the WIMP signal inferred from a likelihood analysis. The image was taken from [11].

Figure 3.4 shows the observed number of events which occur within the signal region, where the latter is defined as the union of the tungsten, calcium and oxygen bands[3].

---

[3]For each nuclear species, the band is defined as the region in the light yield plane which would

As the detectors vary in light resolution, they are subject to different energy thresholds which are given in table 1 of [11]. The high number of events observed by CRESST can partially be explained by various backgrounds which mainly stem from contaminated clamps used in the experiment. Based on the discussion in [11] we use the following estimates of the lead, neutron[4] and alpha backgrounds

$$\left(\frac{\mathrm{d}R}{\mathrm{d}E_R}\right)_{\mathrm{Pb}} = 4.5\,\mathrm{keV}^{-1} \times \left[0.13 + \exp\left(\frac{E_R - 90\,\mathrm{keV}}{13.72\,\mathrm{keV}}\right)\right] , \tag{3.18a}$$

$$\left(\frac{\mathrm{d}R}{\mathrm{d}E_R}\right)_{\mathrm{neutron}} = 1\,\mathrm{keV}^{-1} \times \exp\left(-\frac{E_R}{23.54\,\mathrm{keV}}\right) , \tag{3.18b}$$

$$\left(\frac{\mathrm{d}R}{\mathrm{d}E_R}\right)_{\alpha} = 1\,\mathrm{keV}^{-1} - \frac{0.02\,E_R}{\mathrm{keV}^2} . \tag{3.18c}$$

The background due to leakage of electromagnetic events is extracted from figure 11 in [11]. While the backgrounds are sizable, they seem to explain only $\sim 60\%$ of the events observed at CRESST. The search for additional background sources is clearly indispensable, however, WIMPs offer an intriguing possibility to explain the remaining events.

3.3.2 Null Searches

3.3.2.1 XENON

XENON 10 and its successor XENON 100 are liquid noble detectors in the Gran Sasso laboratory using highly purified liquid xenon as target material. Fiducial volume cuts reduce the background from surface contamination. An incident WIMP would produce direct scintillation (S1 channel) and ionization which is detected via the proportional scintillation mechanism (S2 channel). In the main XENON 10 and XENON 100 runs, the direct scintillation channel is used for energy calibration. The expected number of photo-electrons S1 is related to the nuclear recoil energy by [12]

$$\mathrm{S1} = 3.6\,\mathrm{keV}^{-1}\, L_{\mathrm{eff}}\, E_R . \tag{3.19}$$

The scintillation efficiency L_{eff} is equivalent to a quenching factor. While in earlier analyses a constant value $L_{\mathrm{eff}} = 0.19$ was assumed [97], more recent measurements revealed that L_{eff} decreases towards low E_R [98, 99]. Uncertainties in the determination of the scintillation efficiency play a major role in the interpretation of the XENON data

---

contain 80% of the WIMP scattering events, 10% would occur above, 10% below. We thus estimate the nuclear recoil acceptance to be 90% for oxygen and tungsten, 100% for calcium.

[4]The estimate of the neutron background is based on the observed number of coincidence events. The normalization of this background depends, however, on whether the neutrons are muon-induced or whether they stem from a source. Our normalization is a compromise between both possibilities, but the CRESST confidence regions are not very sensitive to this particular choice.

and have been controversially discussed by several authors [100–104]. We will come back to this issue in section 3.3.4, but for the moment we use the L_{eff} curve provided in [12]. The latter is based on a recent dedicated measurement [99] and employs a logarithmic extrapolation of L_{eff} below 3 keV towards zero at 1 keV. The photo-electrons are also subject to resolution effects. We assume that the measured number of photo-electrons follows a Poisson statistics around the expectation.

The ionization channel (more precisely the S2/S1 ratio) is used for background discrimination. The number of ionization electrons is given by

$$S2 = Q_y \, E_R \tag{3.20}$$

where Q_y denotes the so-called electron yield. The functional form of Q_y was provided in [13]. It is, however, again subject to controversy (see [105]).

In our analysis we use the 4843 kg d data sample from the XENON 100 run which was collected between January 13 and June 8 2010 [12]. The detector efficiency after several background cuts is given in figure 2 of [12]. The energy threshold was set to 4 photo-electrons, i.e. events with $E_R < 8$ keV require an upward fluctuation in S1 to be detected as a signal. Further, events with S2 < 15 ionization electrons are rejected as background which gives an additional reduction to the detector efficiency at threshold. This can be accounted for by converting the recoil energy into an S2 signal (c.f. (3.20)) and calculating the Poisson probability of detecting at least 15 ionization electrons. The XENON 100 data sample contains three candidate events with 6, 18 and 22 photo-electrons respectively (roughly consistent with the expected background of 1.8 ± 0.6).

In addition, we consider a short run of XENON 10 with 12.5 kg d exposure accumulated between August 23 and September 14 2006 [13]. In this run, only the S2 channel was used as it allows for a lower energy threshold compared to the S1 channel. Background reduction is performed by several cuts which reduce the efficiency for nuclear recoils to 94%.[5] The signal region was set to S2 = 5 − 43 ionization electrons, 23 candidate events were observed. We use the form of electron yield Q_y suggested in [13] with a sharp cut-off at $E_R = 1.4$ keV. Resolution effects are considered by convolving the number of ionization electrons with a Poisson distribution. Unfortunately, the XENON 10 constraint turns out to be extremely sensitive to the form of Q_y. This is especially problematic as Q_y was not measured below 3 keV and only model-based extrapolations were used (see [105] for a critical inspection of this procedure). In addition, we will therefore provide a conservative XENON 10 constraint where we set Q_y to zero below 3 keV.

---

[5]More precisely, the efficiency rises from 94% to almost 100% in the considered energy range. To be conservative we will, nevertheless approximate the efficiency by 94%.

3.3.2.2 CDMS

The cryogenic dark matter search CDMS is run in the Soudan laboratory. The detector setup is similar to CRESST, the target material, however, being germanium. Further, CDMS uses the ionization rather than the scintillation signal for background rejection. The CDMS collaboration has published a large data sample (612 kg d exposure) in 2009 [14]. Due to the rather high energy threshold of 10 keV, the corresponding constraints on the WIMP parameter space have been outperformed by XENON 100. Therefore, in this study we will consider only the data from a subsequent low threshold analysis [15]. The lowering of the threshold to 2 keV came at the price of a reduced background rejection, especially electromagnetic events leak into the nuclear recoil regime. We use the sample from the detector T1Z5 with the best energy resolution to set our constraints.[6] The latter contains 38 events at recoil energies $2 - 100$ keV which will conservatively be treated as potential scatterings of WIMPs.[7]

3.3.2.3 SIMPLE

SIMPLE [16, 17] is a superheated droplet detector in the LSBB laboratory which uses C_2ClF_5 as target material. In stage 2 of the experiment a data set of 6.71 kg d was collected in the period April 12 to July 22 2010 [17]. The energy threshold in this run was set to 8 keV, the nucleation efficiency is given in [17]. No candidate event was observed (see also [107]).

3.3.3 Results

We will now present the confidence regions and constraints for the various dark matter searches discussed previously. For the moment we focus on the case of spin-independent elastic WIMP nucleus scattering and further assume that $f_n = f_p$ (isospin conservation). More exotic scenarios will be discussed in the next section. We are thus left with two free parameters: the WIMP mass m_χ and the WIMP proton cross section σ_p.

The confidence regions of DAMA, CoGeNT and CRESST in the two-parameter-space are calculated by means of a χ^2 metric. For DAMA we will consider the first 12 energy bins ($2 - 8$ keV) shown in figure 3.2. Higher energy bins are ignored as they do not exhibit a significant modulation and, correspondingly, their inclusion would only dilute the power of the statistical test. The CoGeNT data sample allows us to determine two individual confidence regions. For the rate analysis we use the total (time-integrated) number of detected events in the 27 energy bins of figure 3.3. For the modulation

---

[6]The energy resolution and efficiency of the detector T1Z5 can be obtained from [15].

[7]The CDMS collaboration states in [15] that the remaining events can be explained by a combination of zero charge, bulk and surface events. A contrary position was taken by the author of [106] who interprets the low energy events in terms of a WIMP signal.

analysis we use the averaged S_m in two larger energy bins as given in (3.17). Turning to CRESST we use 5 energy bins of 2 keV width between 10 and 20 keV and 4 energy bins of 5 keV width between 20 and 40 keV.[8] This leaves us in total with 9 bins, the number of observed events can be extracted from figure 3.4.

The χ^2 metric is defined by

$$\chi^2 = \sum_i \frac{\left(N_i + N_i^{\text{background}} - N_i^{\text{data}} \right)^2}{(\sigma_i)^2} \ . \tag{3.21}$$

Here, N_i and $N_i^{\text{background}}$ stand for the predicted number of signal and background events in the i-th energy bin. The number of measured events is denoted by N_i^{data}, the statistical error by σ_i. If only the modulated spectrum is considered N has to be replaced by the modulation amplitude S_m in the above formula. In the following we will refer to 90% confidence intervals corresponding to $\chi^2 = 4.6$ (14.7, 18.6, 36.7) for 2 (9, 12, 27) energy bins.

The limits from the null searches XENON, CDMS and SIMPLE are generated by using S. Yellin's maximum gap method [108]. The latter examines the likelihood of observing the gaps in energy between candidate events in the presence of an unknown background. Note that for XENON 10 we provide one constraint, where we use the electron yield Q_y suggested by the collaboration and, additionally, a more conservative constraint, where we set Q_y to zero below 3 keV (see discussion in section 3.3.2.1). The 90% confidence intervals for DAMA, CoGeNT and CRESST as well as the 90% confidence limits from the null searches are depicted in figure 3.5.

The confidence regions of DAMA, CoGeNT and CRESST come intriguingly close at $m_\chi \sim 10$ GeV and $\sigma_p \sim 10^{-40}$ cm^2 which may suggest the existence of rather light WIMPs. This interpretation is, however, challenged by the non-observation of WIMP scatterings at XENON, CDMS and SIMPLE. The corresponding limits seem to exclude the parameter regions preferred by DAMA, CoGeNT and CRESST. Further, there is a slight tension between the CoGeNT modulation and rate analysis. The current status of direct dark matter detection is thus controversial.

3.3.4 Resolving the Experimental Tension

Let us now discuss means to resolve the experimental tension.

Underestimated backgrounds. Several proposals for additional background sources have been made. The flux of atmospheric muons exhibits an annual modulation which

---

[8]The CRESST collaboration has published their data in bins of width 1keV. However, the application of the χ^2 metric requires that the statistical error is approximately Gaussian, i.e. the event number per bin must not be to small. To meet this prerequisite we use the described combination of bins.
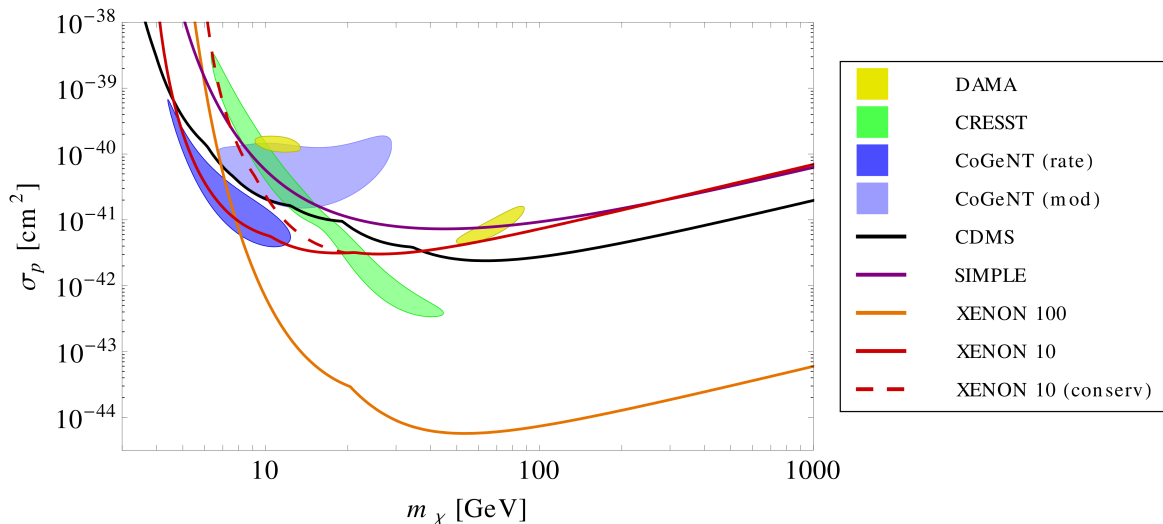
Figure 3.5: Confidence regions and exclusion curves for the experiments described in section 3.3.1 and 3.3.2. Spin-independent WIMP nucleus scattering and $f_n = f_p$ (isospin conservation) is assumed.

is caused by temperature variations in the stratosphere. In [109] it was argued that the observed modulation at DAMA may stem from muon induced neutrons. The same background could be relevant for CoGeNT as both detectors do not use a muon veto. Estimates of the two collaboration [110,111], however, indicate that the muon flux is too low to explain the observed signals. Moreover, in [112] it was found that the modulation phases at DAMA and CoGeNT are inconsistent with muons. There have also been attempts to explain the DAMA signal through the capture of thermal or epithermal neutrons by iodine and the subsequent decay [113]. The corresponding event characteristics seem, however, not to be compatible with the DAMA signal [91]. A number of further background sources for DAMA have been excluded in [7]. The CoGeNT collaboration is currently investigating several possible radioactive backgrounds present in the cavern or the surrounding material of the detector. First estimates indicate, however, that they do not significantly contribute to the signal [111]. In the context of CRESST, ion sputtering caused by ^{206}Pb was recently discussed [114], but quantitative estimates for this background do not yet exist. To recapitulate, there is currently no convincing background model which could explain the observations of DAMA, CoGeNT and CRESST in the absence of dark matter. Still, it is important to remember that the signals appear close to the detector threshold where the proper modeling of backgrounds is extremely challenging. Thus, further investigation on possible background sources is clearly required.

Experimental uncertainties. If we assume that the DAMA, CoGeNT and CRESST signals stem from dark matter, experimental uncertainties may be invoked to weaken the

limits of XENON and CDMS. As we already discussed in section 3.3.2.1 the XENON 100 constraints are affected by the functional form of the scintillation efficiency. While uncertainties in this quantity have been reduced by the recent dedicated measurement [99], one can still considerably diminish the XENON 100 limits by varying L_{eff} within the experimental errors [104]. For XENON 10 the main source of uncertainty is the electron yield Q_y for which we have already accounted by calculating a conservative constraint (see section 3.3.2.1). CDMS has been criticized in [115] for the low energy calibration in the ionization channel and the choice of the nuclear recoil acceptance band in the low threshold analysis. It is, however, hard to imagine, that this has a strong impact on the CDMS limits as – in setting the energy scale of an event – ionization plays only a subleading role in form of the Neganov-Luke effect (see also figure 6 in [15]). The confidence regions of DAMA, CoGeNT and CRESST could also be affected by experimental uncertainties. In our analysis we assumed a sodium quenching factor $Q_{\mathrm{Na}} = 0.3$. However, in [116] it was argued that a slight increase of the quenching factor could move the DAMA region to smaller masses (see also [117]). Additionally, if Q_{Na} was not constant, but rose towards low energies the region would shift to smaller cross sections. Such a behavior of Q_{Na} was indeed predicted from theoretical considerations in [118].

Non-standard astrophysics. The astrophysical input which enters the calculation of WIMP scattering rates is the local dark matter density as well as the local velocity distribution. While the local density only affects the overall normalization of the cross sections, the impact of the velocity distribution is non-trivial. The recoils seen by DAMA, CoGeNT and CRESST appear at energies close to the detector threshold where only WIMPs in the tail of the velocity distribution are energetic enough to contribute to the signal. In our analysis we have made the standard assumption of a Maxwellian velocity distribution. However, it was recently pointed out in [119, 120] that the phase-space distribution of dark matter may be more complex at high velocities due to so-called debris flows. These originate from dark matter particles stripped off from subhalos which have fallen into the Milky Way. The dark matter from subhalos with infall redshift $z \lesssim 4$ is not yet virialized and should add a peak to the local velocity distribution at $v \sim 400 \mathrm{~km~s}^{-1}$ [120]. This would increase the WIMP signal seen by direct searches and thus affect the confidence region and limits shown in figure 3.5. Another important issue is that for an isotropic dark matter velocity distribution the annual modulation of the signal is typically at the per cent level, while the modulation can be enhanced if there are asymmetries in the distribution. An increased modulation seems desirable as it could move the DAMA confidence region in figure 3.5 to smaller cross sections. Further, it could reconcile the CoGeNT rate and modulation analyses. Interestingly, simulations indicate at least some degree of anisotropy between radial and tangential dark matter velocities (see e.g. [121]). Due to the astrophysical uncertainties, there exist attempts to compare the results of direct searches without using any assumptions on the velocity

distribution [122]. These seem to indicate, that the tension between direct searches can be ameliorated but not completely resolved by means of astrophysics [96].

Non-standard WIMPs. There exist numerous proposals to modify the couplings and properties of WIMPs compared to the standard case. As a simple modification one can assume isospin violating WIMP couplings, i.e. $f_n \neq f_p$. The proton to neutron ratio is slightly different for the various target materials used in direct detection. In [19, 20] it was pointed out that if one designs the couplings such that $f_n = -0.7 f_p$ the sensitivity of a xenon target to WIMP scatterings gets greatly reduced. In figure 3.6 we show the confidence regions and constraints for isospin violating dark matter with this particular choice of couplings.
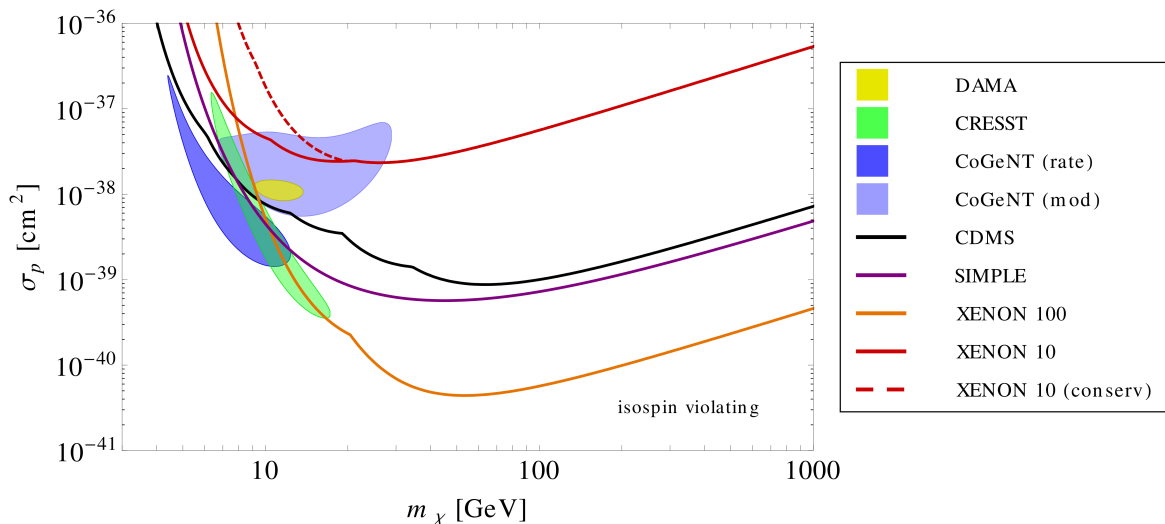
Figure 3.6: Same as figure 3.5 for $f_n = -0.7 f_p$ (isospin violation).

Indeed, it can be seen that there is a better agreement between the DAMA, CRESST and CoGeNT regions, and, further, that the limits from XENON 10 and XENON 100 get substantially weaker. Still, the tension with CDMS and SIMPLE cannot be completely resolved. Moreover, one should note that the improvement only occurs for f_n very close to $-0.7 f_p$ which lacks any theoretical motivation.

Another proposal to explain at least the DAMA signal was to invoke spin-dependent interactions. The DAMA target contains sodium which has an uneven number of protons, i.e. it is very sensitive to spin-dependent WIMP proton couplings. Further, there is no coherent enhancement of the WIMP nucleus cross section in the spin-dependent case, i.e. heavy target materials like germanium and xenon lose sensitivity compared to the spin-independent case. However, the new droplet detectors SIMPLE [16, 17], COUPP [123] and PICASSO [124] are especially sensitive to spin-dependent couplings

and disfavor this explanation for the DAMA signal. Additional strong constraints on spin-dependent interactions which arise from neutrino telescopes will be discussed in section 4.1.

To briefly summarize, there does not yet exist a satisfactory explanation for the observation of possible signals at DAMA, CoGeNT and CRESST and the null results by XENON, CDMS and SIMPLE. Several suggested backgrounds like e.g. muon-induced neutrons have been excluded as a source of the observed signals. If one interprets the signals in terms of light WIMPs, experimental uncertainties, non-standard astrophysics or non-standard couplings of the WIMPs may ameliorate the experimental tension. However, none of the three possibilities alone is able to reconcile all experimental results. In the following we will turn to the indirect search for light WIMPs.

Chapter 4

Indirect Dark Matter Searches

Indirect searches aim to detect the daughter particles stemming from the annihilation on WIMPs in the halo or in celestial bodies. In this chapter we will mainly focus on neutrino and antiproton searches and briefly comment on complementary detection methods. We assume that WIMPs annihilate into pairs of Standard Model particles. But – to keep our analysis as model-independent as possible – we consider all relevant final states including quarks, leptons and gauge bosons. For a given channel the spectra of neutrinos and antiprotons per annihilation are obtained with the PYTHIA Monte Carlo (version 8.1) [125].

4.1 Neutrino Searches

WIMPs on their way through the galaxy traverse celestial bodies like the sun. If – during such a passage – they lose kinetic energy by scattering with nuclei, they may get gravitationally trapped. With a sufficient amount of WIMPs captured they start annihilating. Most final state particles are rapidly stopped due to their interactions with ordinary matter. However, if neutrinos are generated, they can escape even from the interior of stars. The neutrino signals from WIMP annihilation in the sun are potentially observable with earth-bound neutrino telescopes. The following discussion is based on [126].

4.1.1 Dark Matter in the Sun

Dark matter particles are captured in the sun if, by scattering with nuclei, they lose so much kinetic energy that they cannot escape from its gravitational potential. On the other hand, there exist two processes by which the WIMP number in the sun gets reduced: annihilation and evaporation. A consistent treatment of capture, annihilation and evaporation which includes the case of p-wave annihilation has been lacking in the

literature and shall be performed here.

4.1.1.1 Capture

The capture rate of WIMPs in the sun has the same form as the scattering rate in a detector (c.f. (3.3)). The difference is just that WIMPs scattering at the distance r from the center of the sun are trapped only if their velocity after scattering is below the solar escape velocity $v_{\text{esc},\odot}(r)$. Further, it is convenient to reverse the integration order. The differential capture rate thus reads [127]

$$\frac{\mathrm{d}C_\odot}{\mathrm{d}V} = \sum_N \frac{\rho_0\,\rho_{\odot,N}(r)}{2m_\chi\mu_N^2}\,\sigma_N \int\limits_0^\infty \mathrm{d}u\, \frac{f_\odot(u)}{u} \int\limits_{E_{R,\min}}^{E_{R,\max}} \mathrm{d}E_R\,|F(E_R)|^2\,. \tag{4.1}$$

The sum runs over the various nuclear isotopes contained in the sun. While the dominant components are hydrogen and helium, heavier nuclei cannot be neglected. Their low abundance is partly compensated by kinematics: WIMPs typically lose more energy if they scatter off heavier targets and are more likely to be trapped.

We extract the mass density distribution $\rho_{\odot,N}(r)$ of nuclei N from the solar model AGSS09 [128]. The reduced mass of the WIMP nucleus system μ_N, the WIMP nucleus cross section σ_N and the form factor $F(E_R)$ have been introduced in section 3.2.2 for spin-independent and spin-dependent interactions. Note that in the case of spin-independent scattering the cross section grows quadratically with the nucleon number. As a consequence nuclei from hydrogen up to nickel contribute significantly to the capture. In the case of spin-dependent scattering there is no enhancement of the cross section for heavier nuclei and thus only the capture at hydrogen is relevant. The E_R integration runs from the minimal energy transfer $E_{R,\min}$ required to trap the WIMP to the maximal energy transfer $E_{R,\max}$ allowed by kinematics. One finds

$$E_{R,\min} = \frac{1}{2}m_\chi u^2\,, \qquad E_{R,\max} = \frac{2\mu_N^2}{m_N}\left(u^2 + v_{\text{esc},\odot}^2(r)\right)\,. \tag{4.2}$$

Here u denotes the velocity of a WIMP before it enters the gravitational potential of the sun. Its velocity just before scattering is then simply given by $\sqrt{u^2 + v_{\text{esc},\odot}^2(r)}$.

From the astrophysical side, the local dark matter density $\rho_0 \simeq 0.39\,\text{GeV cm}^{-3}$ (see discussion in section 2.3) and the distribution $f_\odot(u)$ of WIMP velocities u in the rest frame of the sun enters (4.1). As shown in section 3.2.1 the latter can be obtained from the velocity distribution $f(v)$ in the galactic rest frame by performing a shift with the velocity of the sun v_{sun}. We assume the same Maxwellian form for $f(v)$ as in (2.14). Due to kinematics, WIMPs in the tail of the velocity distribution are very unlikely to be captured and, therefore, the truncation of $f(v)$ at the escape velocity can be neglected.

This allows us to find an analytical expression for $f_\odot(u)$:

$$\frac{f_\odot(u)}{u} = \frac{1}{\sqrt{\pi}\, v_\odot^2} \left[\exp\left(-\frac{(u - v_{\text{sun}})^2}{v_{\text{sun}}^2} \right) - \exp\left(-\frac{(u + v_{\text{sun}})^2}{v_{\text{sun}}^2} \right) \right] . \tag{4.3}$$

The total capture rate is given by

$$C_\odot = 4\pi \int_0^{R_\odot} \mathrm{d}r\, r^2 \frac{\mathrm{d}C_\odot}{\mathrm{d}V} , \tag{4.4}$$

where $R_\odot$ is the solar radius.

The capture rates for spin-independent (with and without isospin violation) and spin-dependent scattering are shown in figure 4.1.
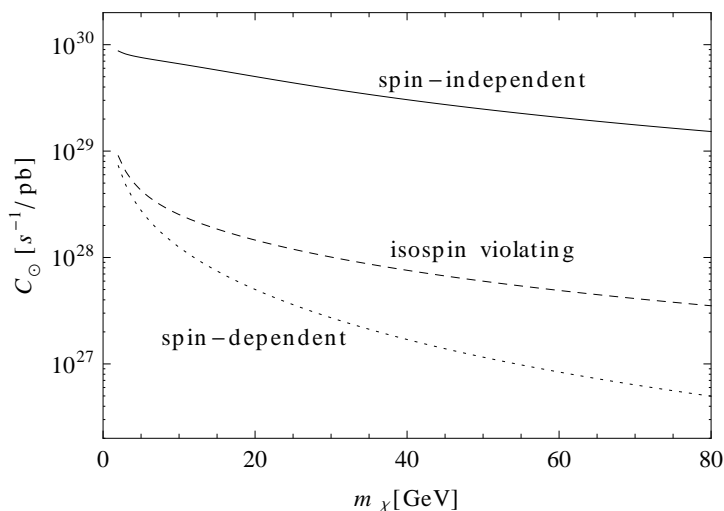
Figure 4.1: Solar WIMP capture rate for spin-independent scattering with $f_n = f_p$ (solid) and $f_n = -0.7\, f_p$ (dashed). Also shown is the rate for spin-dependent scattering (dotted) for which the coupling to neutrons is neglected.

4.1.1.2   Annihilation

Subsequent to their capture, WIMPs continuously undergo scattering with nuclei in the sun and thermalize. Therefore, they follow a Maxwellian velocity distribution with temperature T_χ equal to that of nuclei:

$$f_{\text{solar}}(v) = \sqrt{\frac{2m_\chi^3}{\pi\, T_\chi^3}}\, v^2 \exp\left(-\frac{m_\chi v^2}{2\, T_\chi} \right) . \tag{4.5}$$

It turns out that for all relevant masses the WIMPs reside close to the center of the sun. More specifically, the WIMP number density follows a scaling law very similar to the

barometric formula. One finds [25]

$$n_\chi(r) = n_0 \, \exp\left(-\frac{m_\chi \phi(r)}{T_\chi} \right) . \tag{4.6}$$

In the core region the variations of the solar temperature $T_\odot(r)$ and density $\rho_\odot(r)$ are small and one can approximate both quantities by constants. A reasonable assumption is $T_\chi = T_\odot(\bar{r})$ and $\rho_\odot(r) = \rho_\odot(\bar{r})$ where $\bar{r}$ is the mean WIMP orbit radius. In order to determine $\bar{r}$ we use that for constant density, the gravitational potential with respect to the solar core reads $\phi(r) = 2\pi\rho_\odot(\bar{r})r^2 G/3$ with G being Newton's constant. By averaging r over the WIMP density we arrive at the implicit equation

$$\bar{r} = \sqrt{\frac{6\,T_\odot(\bar{r})}{\pi^2\,G\,\rho_\odot(\bar{r})\,m_\chi}} \tag{4.7}$$

which has to be solved numerically. The solar mass and temperature distribution can be taken from the solar model AGSS09 [128]. The WIMP temperature $T_\chi = T_\odot(\bar{r})$ which we obtain by this procedure is typically very close to the core temperature of the sun $T_{\odot,\mathrm{core}} = 1.5 \times 10^7$ K.

The total annihilation rate of WIMPs in the sun $\Gamma_\odot$ scales quadratically with the total WIMP number N. Therefore it is convenient to define $\Gamma_\odot = A_\odot N^2/2$. The quantity $A_\odot$ can be viewed as annihilation rate per particle. It can be expressed in terms of the WIMP annihilation cross section as

$$A_\odot = \frac{1}{N^2} \int \mathrm{d}r \, 4\pi r^2 \, n_\chi^2(r) \, \langle \sigma v_\mathrm{rel} \rangle_\odot = \left(\frac{\sqrt{2}}{\pi \bar{r}} \right)^3 \langle \sigma v_\mathrm{rel} \rangle_\odot . \tag{4.8}$$

We find that for WIMP masses $m_\chi \gtrsim 1\,\mathrm{GeV}$ the rate is well approximated by

$$A_\odot = 4.5 \cdot 10^{-30}\,\mathrm{cm}^{-3} \left(\frac{m_\chi - 0.6\,\mathrm{GeV}}{10\,\mathrm{GeV}} \right)^{3/2} \langle \sigma v_\mathrm{rel} \rangle_\odot . \tag{4.9}$$

Note that in this expression σv_rel has to be averaged over the WIMP velocity distribution in the sun (4.5) which is markedly different from the velocity distribution at the time of freeze-out. Using the velocity expansion (2.7) one finds

$$\langle \sigma v_\mathrm{rel} \rangle_\odot = \sigma_\mathrm{s\text{-}wave} + \frac{6\,T_\odot(\bar{r})}{m_\chi} \sigma_\mathrm{p\text{-}wave} . \tag{4.10}$$

Indeed the velocity distribution is irrelevant for s-wave annihilation. However, in the case of p-wave annihilation the thermal averaging of σv_rel leads to a cross section which is by a factor $T_\odot(\bar{r})/T_F \sim 10^{-6}$ smaller than at freeze-out.

4.1.1.3 Evaporation

The second process which can reduce the WIMP number in the sun is evaporation [25,26, 129]. The kinetic energy of a WIMP changes statistically by the scattering with nuclei, but in rare cases WIMPs may gain sufficient kinetic energy to reescape or evaporate from the sun. This process is highly sensitive to the WIMP mass: the lighter the WIMP the more likely it is to evaporate. This is partly because light WIMPs have – on average – higher velocities in the sun (c.f. (4.5)) and partly due to the higher energy transfer in their scattering with nuclei. The evaporation rate per particle scales as

$$E_\odot \sim \frac{1}{t_\odot} \exp\left(-\frac{30\,(m_\chi - m_{\text{evap}})}{m_{\text{evap}}}\right) \,, \tag{4.11}$$

where $t_\odot \simeq 4.7\,\text{Gyr}$ is the age of the sun and m_{evap} the evaporation mass. The latter is defined as the mass for which $E_\odot = 1/t_\odot$. Note that if m_χ exceeds m_{evap} by a few percent, evaporation is totally negligible. Conversely, if m_χ falls slightly below m_{evap} virtually all trapped WIMPs escape the sun via evaporation rather than by annihilation. In order to determine the evaporation mass, we use the following approximation for the evaporation rate [129]

$$E_\odot \simeq \frac{8}{\pi^3} \frac{\sigma_{\text{evap}}}{\bar{r}^3} \bar{v} \frac{E_{\text{esc}}}{T_\odot(\bar{r})} \exp\left[-\frac{E_{\text{esc}}}{2T_\odot(\bar{r})}\right] . \tag{4.12}$$

Here E_{esc} denotes the escape energy at the center of the sun and σ_{evap} the evaporation cross section. The latter is the total cross section of all nuclei interior to the radius $r_{0.95}$ which is defined by $T_\odot(r_{0.95}) = 0.95\,T_\odot(\bar{r})$. Finally, the mean WIMP speed $\bar{v}$ for the thermal distribution (4.5) is given by

$$\bar{v} = \sqrt{\frac{8T_\odot(\bar{r})}{\pi\,m_\chi}} \,. \tag{4.13}$$

The estimate (4.12) is only accurate to within a factor of three [129]. The error is due to the fact that the WIMP velocity distribution in the sun shows deviations from a thermal distribution at high velocities which is not taken into account in (4.12) (see discussion in [26]). The precision is, however, sufficient for our purposes as it translates into an uncertainty in the evaporation mass of only 3%. An analytic approximation of the evaporation mass reads

$$m_{\text{evap}} = m_0 + 0.32\,\text{GeV}\,\log_{10}\left(\frac{\sigma_p}{10^{-40}\,\text{cm}^2}\right) \,, \tag{4.14}$$

where $m_0 = 3.5\,\text{GeV}$ ($m_0 = 3.02\,\text{GeV}$) in the case of spin-independent (spin-dependent) interactions.

4.1.1.4 Neutrino Production

The WIMP number in the sun N changes by capture, annihilation and evaporation. The differential equation describing the evolution of N reads

$$\dot{N} = C_\odot - A_\odot N^2 - E_\odot N \ . \tag{4.15}$$

The evaporation rate is exponentially sensitive to the WIMP mass. If $m_\chi < m_{\text{evap}}$ evaporation is typically the dominant WIMP number reducing process. In this case the annihilation signal is highly suppressed and hardly detectable. However, already for $m_\chi \gtrsim 5\,\text{GeV}$, evaporation is negligible and the solution to (4.15) takes the simple form

$$N = \sqrt{\frac{C_\odot}{A_\odot}} \tanh(\sqrt{C_\odot A_\odot}\, t) \ . \tag{4.16}$$

The relevant quantity for the detection of a WIMP signal is the present total annihilation rate which takes the form

$$\Gamma_\odot = \frac{1}{2} A_\odot N^2 = \frac{1}{2} C_\odot \tanh^2\left(\sqrt{C_\odot A_\odot}\, t_\odot\right) \ . \tag{4.17}$$

In the limit $\sqrt{C_\odot A_\odot}\, t_\odot \gg 1$ equilibrium between capture and annihilation is reached and one finds $\Gamma_\odot = C_\odot/2$.

As an example, let us consider a light thermal WIMP ($m_\chi \sim 10\,\text{GeV}$) with a spin-independent cross section in the range favored by direct detection experiments ($\sigma_p \sim 10^{-40}\text{cm}^2$). Such a WIMP would have a capture rate of $C_\odot \sim 10^{26}\,\text{s}^{-1}$ and an annihilation rate of $A_\odot \sim 10^{-55}\,\text{s}^{-1}$ ($A_\odot \sim 5 \times 10^{-61}\,\text{s}^{-1}$) assuming s-wave (p-wave) annihilation. This corresponds to

$$\sqrt{C_\odot A_\odot}\, t_\odot \sim 5 \times 10^2 \qquad \text{(s-wave)} \ , \tag{4.18a}$$

$$\sqrt{C_\odot A_\odot}\, t_\odot \sim 1 \qquad\quad \text{(p-wave)} \ . \tag{4.18b}$$

We can conclude that for s-wave annihilation the equilibrium is safely reached and $\Gamma_\odot = C_\odot/2$. This statement holds even for cross sections as small as $\sigma_p \sim 10^{-44}\,\text{cm}^2$. In the case of pure p-wave annihilation the equilibration time scale is typically of the same order as the life-time of the sun. This implies an $\mathcal{O}(1)$ suppression of $\Gamma_\odot$ compared to the s-wave case.

Note, however, that the thermal average of v_{rel}^2 is markedly different for WIMPs in the sun compared to WIMPs at freeze-out, the ratio is roughly $T_\odot/T_F \sim 10^{-6}$ (see section 4.1.1.2). The suppression for p-wave annihilation in the sun is, therefore, very pronounced. But even in models with p-wave annihilation at freeze-out, there exists a suppressed s-wave contribution, i.e. $\sigma_{\text{s-wave}} \ll \sigma_{\text{p-wave}}$ but $\sigma_{\text{s-wave}} \neq 0$. Indeed, it may happen that, despite its suppression, the s-wave contribution overcomes the p-wave contribution in the sun due to the very small WIMP velocities. In such a case the capture annihilation equilibrium in the sun may still be reached leading to an unsuppressed WIMP annihilation signal.

4.1.2 Neutrino Interactions and Propagation

Most of the WIMP annihilation products are immediately stopped within the sun due to their rather strong interactions with ordinary matter. Neutrinos, however, are so weakly coupled that they can escape the sun and are potentially detectable at the earth. We now want to determine the neutrino flux at the earth stemming from WIMP annihilation in the sun. For this, we have to consider the propagation of neutrinos from their production point in the solar core to the detector. Before we introduce the quantum mechanical formalism for neutrino propagation, let us briefly discuss their interactions.

4.1.2.1 Interactions

Neutrinos traveling through a medium undergo charged current (CC) and neutral current (NC) interactions. While both affect their oscillation probabilities in the sun, mainly the CC interactions are relevant for the detection of neutrinos. For high energy neutrinos ($E_\nu > 10\,\mathrm{GeV}$) the scattering is dominated by deep inelastic interactions with nuclei. In this case simple analytic approximations for the differential neutrino cross sections exist (see e.g. Appendix C in [130]). In this study, however, we are dealing with neutrinos which potentially stem from the annihilation of light WIMPs, i.e. $E_\nu = \mathcal{O}(1\,\mathrm{GeV})$. This implies that the momentum transfer between neutrinos and nuclei is so low that the parton description of nucleons breaks down. In fact, neutrinos in the GeV range dominantly interact via quasi-elastic scattering [131] and single meson production [132, 133]. The latter complicates the calculation of cross sections substantially as a series of intermediate nuclear resonances contributes to this process. Further, the angular distribution of the final state particles is sensitive to the type of interaction. As an analytic treatment of neutrino interactions is hardly feasible, we will perform a simulation with the publicly available code NEUGEN 3.5.5 [134]. The latter automatically takes into account the above-mentioned processes as well as further subleading contributions from coherent meson production. Note that a solid treatment of neutrino interactions is inevitable for the correct calculation of neutrino detection rates. The propagation of GeV neutrinos in the sun is only slightly affected by neutrino interactions, nevertheless we will also extract the cross sections relevant for its description from NEUGEN.

4.1.2.2 Propagation

To determine the local neutrino flux stemming from WIMP annihilations in the sun we have to consider neutrino oscillations and matter effects in the sun. We perform a full quantum mechanical treatment by following the evolution of the density matrix ϱ. The latter specifies the population of flavor eigenstates (diagonal entries) and superpositions of flavors (off-diagonal entries). The matrix formalism is required as neutrino interactions and masses cannot be diagonalized in the same basis. The evolution of ϱ from the

neutrino production point to the detector is determined by the differential equation [130, 135–137]

$$\frac{\mathrm{d}\boldsymbol{\varrho}}{\mathrm{d}r} = -i[\boldsymbol{H}, \boldsymbol{\varrho}] + \frac{\mathrm{d}\boldsymbol{\varrho}}{\mathrm{d}r}\bigg|_{\mathrm{NC}} + \frac{\mathrm{d}\boldsymbol{\varrho}}{\mathrm{d}r}\bigg|_{\mathrm{CC}} - \epsilon[\boldsymbol{H}, [\boldsymbol{H}, \boldsymbol{\varrho}]] \,. \tag{4.19}$$

The first term on the right hand side describes matter and vacuum oscillations with the Hamiltonian

$$\boldsymbol{H} = \frac{\boldsymbol{m}^\dagger \boldsymbol{m}}{2\,E_\nu} + \frac{G_F}{\sqrt{2}} \begin{pmatrix} 2\,n_e(r) - n_n(r) & 0 & 0 \\ 0 & -n_n(r) & 0 \\ 0 & 0 & -n_n(r) \end{pmatrix} \,. \tag{4.20}$$

Here, $\boldsymbol{m}$ denotes the neutrino mass matrix in the flavor basis which is related to the neutrino mixing matrix $\boldsymbol{V}$ by $\boldsymbol{m}^\dagger \boldsymbol{m} = \boldsymbol{V} \operatorname{diag}(m_1^2, m_2^2, m_3^2)\, \boldsymbol{V}^\dagger$, where the m_i are the neutrino mass eigenvalues. For antineutrinos one simply has to replace $\boldsymbol{m}$ by its complex conjugate and flip the sign in the matter term. Note that the absolute mass scale drops out of $[\boldsymbol{H}, \boldsymbol{\varrho}]$, the solar and atmospheric neutrino mixing angles can be taken from [138]. We further set $\theta_{13} = 0$ in our analysis, but a nonzero θ_{13} as suggested by recent reactor experiments [139, 140] only marginally affects the propagation [136, 137, 141]. The electron and neutron number densities $n_e(r)$ and $n_n(r)$ in the sun are taken from the solar model AGSS09 [128].

The second and third term on the right hand side of (4.19) account for neutral and charged current interactions. One finds

$$\frac{\mathrm{d}\boldsymbol{\varrho}}{\mathrm{d}r}\bigg|_{\mathrm{NC}} = -\int_0^{E_\nu} \mathrm{d}E'_\nu \frac{\mathrm{d}\Gamma_{\mathrm{NC}}}{\mathrm{d}E'_\nu}(E_\nu, E'_\nu)\,\boldsymbol{\rho}(E_\nu) + \int_{E_\nu}^\infty \mathrm{d}E'_\nu \frac{\mathrm{d}\Gamma_{\mathrm{NC}}}{\mathrm{d}E'_\nu}(E'_\nu, E_\nu)\,\boldsymbol{\rho}(E'_\nu)\,, \tag{4.21a}$$

$$\frac{\mathrm{d}\boldsymbol{\varrho}}{\mathrm{d}r}\bigg|_{\mathrm{CC}} = -\frac{\{\boldsymbol{\Gamma}_{\mathrm{CC}}, \boldsymbol{\varrho}\}}{2}\,, \tag{4.21b}$$

where in both equations the first term on the right hand side treats absorption. In the case of neutral current interactions, there is also a reinjection term. The latter can be neglected for charged current interactions of neutrinos in the GeV range [142]. The interaction rates are defined as

$$\Gamma_{\mathrm{NC}} = n_p(r)\, \sigma_{\mathrm{NC}}^{\nu\,p} + n_n(r)\, \sigma_{\mathrm{NC}}^{\nu\,n}\,, \tag{4.22a}$$

$$\Gamma_{\mathrm{CC}}^\ell = n_p(r)\, \sigma_{\mathrm{CC}}^{\nu_\ell\,p} + n_n(r)\, \sigma_{\mathrm{CC}}^{\nu_\ell\,n}\,, \quad \boldsymbol{\Gamma}_{\mathrm{CC}} = \operatorname{diag}(\Gamma_{\mathrm{CC}}^e, \Gamma_{\mathrm{CC}}^\mu, \Gamma_{\mathrm{CC}}^\tau)\,. \tag{4.22b}$$

The charged and neutral current cross sections of neutrinos with protons and neutrons can be extracted from NEUGEN [134]. The solar proton and neutron densities are taken from AGSS09 [128]. Note that $\sigma_{\mathrm{CC}}^{\nu_\tau\,p} \neq \sigma_{\mathrm{CC}}^{\nu_{e,\mu}\,p}$ due to phase-space suppression for final state taus. This is the reason one has to keep the distinction between flavors in the CC case and use the matrix form for $\boldsymbol{\Gamma}_{\mathrm{CC}}$.

Finally, one has to include the decoherence effect in neutrino propagation due to the finite energy resolution of any detector. Additionally, the WIMP annihilations produce neutrinos in a region with diameter comparable to or larger than the neutrino oscillation length; and also the distance between sun and earth changes with the orbital movement of the earth. All this implies that individual oscillations cannot be traced, rather the neutrino detection probability has to be averaged over an oscillation period. This is effectively done by the last term in (4.19), where we set $\epsilon = 0.01\,R_\odot$ as suggested in [130].

The evolution equation for the density matrix has to be solved numerically which is conveniently done in two steps. First one propagates the neutrinos from the solar core to the surface of the sun, and then further to the earth. For neutrinos with $E_\nu \lesssim 100\,\mathrm{GeV}$ matter effects in the earth can be neglected. The density matrix at $r = 0$ is given by the initial neutrino spectra obtained from WIMP annihilation.

The following WIMP annihilation channels are considered:

$$\chi\chi \to b\bar{b},\; c\bar{c},\; \tau\bar{\tau},\; \nu\bar{\nu}\;. \tag{4.23}$$

We assume 100% annihilation in one channel, but – for a given model – it is straightforward to rescale our results by the appropriate branching fraction. For the neutrino channel we set $\nu = (\nu_\tau + \nu_\mu + \nu_e)/3$, but – due to neutrino oscillations – the propagated neutrino flux at the earth is not particularly sensitive to this choice. Annihilation into photons, lighter quarks, gluons, electrons and muons is omitted as the corresponding neutrino signals are negligible.[1]

The electron, muon and tau neutrino fluxes which arrive at the earth from WIMP annihilation in the sun may be written as

$$\Phi_{\nu_e,\nu_\mu,\nu_\tau} = \frac{\Gamma_\odot}{4\pi d_\odot^2}\left.\frac{\mathrm{d}N_{\bar{f}f}^{\nu_e,\nu_\mu,\nu_\tau}}{\mathrm{d}E_{\nu_e,\nu_\mu,\nu_\tau}}\right|_{\mathrm{earth}}, \tag{4.24}$$

where $d_\odot$ denotes the distance between earth and sun, $(\mathrm{d}N_{\bar{f}f}^{\nu_e,\nu_\mu,\nu_\tau}/\mathrm{d}E_{\nu_e,\nu_\mu,\nu_\tau})|_{\mathrm{earth}}$ the propagated electron, muon and tau neutrino spectra per annihilation into the final state $\bar{f}f$. The latter are obtained as the diagonal entries of the propagated neutrino density matrix. The expression for the antineutrino fluxes is analogous.

4.1.3 Detection at Super-Kamiokande

Super-Kamiokande is currently the most sensitive experiment for neutrino signals in the GeV range as they arise from light dark matter annihilation. Therefore, we will not consider other neutrino telescopes. The Super-Kamiokande experiment is located 1 km

---

[1]Annihilation into muons would induce a large number of neutrinos. However, as muons are stopped in the sun prior to their decay, the energy of the daughter neutrinos resides below the detection threshold.

underground in the Kamioka-mine (36° 14′ N, 137° 11′ E). It consists of a stainless-steel tank filled with 50000 tons of water. The inner detector has cylindrical shape with a height of 36.2 m and a radius of 16.9 m. The tank wall is equipped with around 13000 photomultipliers which are sensitive to the Cherenkov light emitted by charged particles, especially muons, when they traverse the detector volume. Details on the detector setup can be found in [143].

4.1.3.1   The Neutrino Flux at the Detector

The incident differential muon neutrino flux at Super-Kamiokande arising from solar dark matter annihilation can we written as

$$\frac{\mathrm{d}\Phi_{\nu_\mu}}{\mathrm{d}\cos\theta_\nu} = \Phi_{\nu_\mu} \frac{\mathrm{d}P}{\mathrm{d}\cos\theta_\nu} \; , \tag{4.25}$$

where θ_ν denotes the zenith angle which is the angle between the incoming neutrino and the cylinder axis of the Super-Kamiokande detector. The neutrino flux Φ_{ν_μ} which is a function of E_{ν_μ} can be determined by the formalism developed in section 4.1.2.2. It depends on the total WIMP annihilation rate in the sun and on the annihilation channel. The function $\mathrm{d}P/\mathrm{d}\cos\theta_\nu$ stands for the differential probability for the neutrino beam to arrive with angle $\cos\theta_\nu$ (averaged over the run time of Super-Kamiokande given in [144]). It can be obtained by tracking the orientation of the Super-Kamiokande detector relative to the sun taking into account the orbital and rotational movement of the earth. For this we employ the IDL Astronomy User's Library [145].

4.1.3.2   Event Categories

Due to neutrino oscillations the neutrino flux at the earth is well-mixed among the flavors irrespective of the primary dark matter annihilation channel. Super-Kamiokande is, however, mainly sensitive to muon neutrinos as their charged partners leave long tracks in the detector. Events are classified in the following categories [146] (see figure 4.2 for illustration):

- upward through-going muons,

- upward stopping muons,

- partially contained muon-like events,

- fully contained muon-like events.

The first two event classes refer to muons created in the rock outside Super-Kamiokande which either traverse the detector (through-going muons) or which are stopped in the detector (stopping muons). Only muons traveling in the upward direction are accepted

upward through–going   upward stopping   partially contained   fully contained
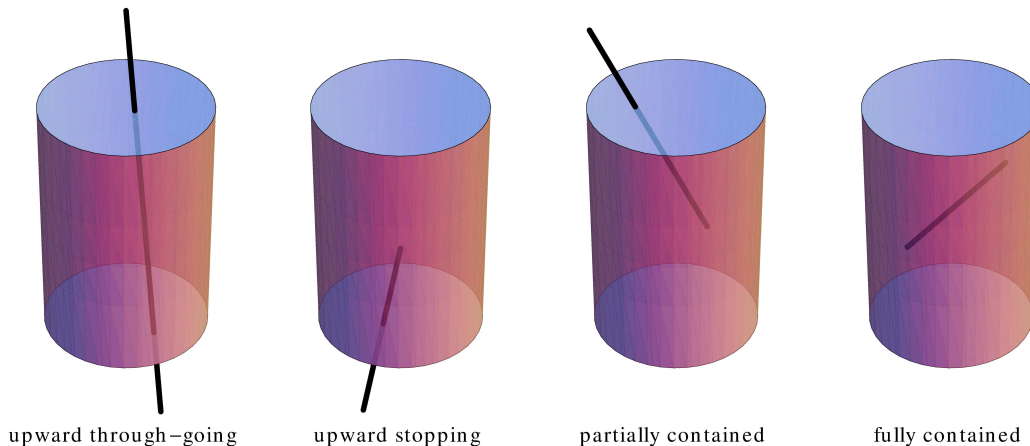
Figure 4.2: Event types at Super-Kamiokande.

such that the earth can be used as a shield against background from cosmic radiation. The last two event categories include muons which are created in the detector and either stopped (fully contained events) or not stopped (partially contained events) inside.

The relative importance of the different event types strongly depends on the neutrino energy (see figure 1 in [146]). Neutrinos with $E_\nu \ll 10$ GeV dominantly induce fully contained events, neutrinos with $E_\nu \sim 10$ GeV partially contained events and stopping muons. Finally, higher energy neutrinos mostly generate muons which traverse the entire detector volume.

In this work, we do not consider upward through-going muons. They have previously been analyzed in the dark matter context in [22] but are hardly relevant for the detection of light WIMPs. We further discard partially contained events as – from the publicly available data – it is impossible to reconstruct the energy dependent efficiency of Super-Kamiokande for this specific category. We are therefore left with fully contained (muon-like) events and stopping muons which we will now discuss in more detail.

For fully contained events Super-Kamiokande uses a particle reconstruction algorithm which distinguishes between electron-like and muon-like events. In our analysis we focus on the latter and neglect the small probability of misidentification. To eliminate backgrounds, several cuts are applied to the raw data: events are discarded if the initial vertex is less than 2 m away from the detector wall or if the momentum of the muon is below a threshold momentum $p_{\mu,\text{th}}$ which depends on the number of observed Cherenkov rings. Multi-ring events are induced if the neutrino charged current interaction gives rise to further charged particles (pions) apart from the muon. The threshold is set to $p_{\mu,\text{th}} = 200$ MeV for single-ring and $p_{\mu,\text{th}} = 600$ MeV for multi-ring events [146]

which corresponds to threshold energies of $E_{\mu,\text{th}} = 226$ MeV and $E_{\mu,\text{th}} = 609$ MeV respectively. In our event simulation we identify quasi-elastic interactions as single-ring all other types of charged current interactions as multi-ring. This procedure induces a small error as in rare cases events with pions are misidentified as single-ring. Therefore, we reject slightly to many events with $p_\mu = 200 - 600$ MeV which, however, only makes our analysis more conservative.

Stopping muons created in the rock surrounding the detector are accepted if they deposit an energy of at least $E_{\mu,\text{th}} = 1.6$ GeV in the detector. This corresponding to a track length of ~ 7 m. As already mentioned, muons traveling in the downward direction are generally discarded.

4.1.3.3 The Event Rate

The fully contained muon-like event rate for an incident differential neutrino flux $\mathrm{d}\phi_{\nu_\mu}/\mathrm{d}\cos\theta_\nu$ at the Super-Kamiokande detector can be written as

$$
R^{\text{FC}} = n_{\text{H}_2\text{O}} \int\limits_{0}^{m_\chi} \mathrm{d}E_{\nu_\mu} \int\limits_{-1}^{1} \mathrm{d}\cos\theta_\nu \, \frac{\mathrm{d}\Phi_{\nu_\mu}}{\mathrm{d}\cos\theta_\nu} \int\limits_{\text{V}_{\text{detector}}} \mathrm{d}^3x \int\limits_{E_{\mu,\text{th}}}^{E_{\nu_\mu}} \mathrm{d}E_\mu
$$

$$
\times \int\limits_{0}^{4\pi} \mathrm{d}\Omega_{\mu\nu} \, \frac{\mathrm{d}^2\sigma_{\text{CC}}^{\nu_\mu \, \text{H}_2\text{O}}}{\mathrm{d}E_\mu \, \mathrm{d}\Omega_{\mu\nu}} \, \delta^{\text{FC}} \left(\vec{x}, E_\mu, \theta_\nu, \Omega_{\mu\nu} \right) \; + \; (\nu_\mu \leftrightarrow \bar{\nu}_\mu) \; . \tag{4.26}
$$

Here, θ_ν denotes the zenith angle of the incoming neutrino, while $\Omega_{\mu\nu}$ stands for the solid angle of the muon relative to the neutrino. The differential neutrino charged current cross section at water molecules $\mathrm{d}\sigma_{\text{CC}}^{\nu_\mu \, \text{H}_2\text{O}}$ is calculated with NEUGEN (see section 4.1.2.1). Further, $n_{\text{H}_2\text{O}}$ is the number density of water molecules and $\vec{x}$ the position of the interaction vertex. The space integral runs over the volume of the detector. The track length of the muon in the detector can be reconstructed by using the appropriate formula for energy loss in water (table II-28 in [147]). The function δ^{FC} takes the value $\delta^{\text{FC}} = 1$ for a muon which is stopped in the detector and passes the event cuts described in section 4.1.3.2, otherwise $\delta^{\text{FC}} = 0$. Simple geometrical considerations allow us to determine δ^{FC} for a given $\vec{x}$, if the energy and angle of the muon in the detector are known. The latter is fixed by θ_ν and $\Omega_{\mu\nu}$. Note that in most analyses performed so far it was assumed that neutrino and muon are collinear which would simplify (4.26) substantially. Unfortunately, this approximation is not valid for the energy range under consideration. Therefore, we keep track of the finite angle between neutrino and muon.

In a slightly modified version (4.26) also holds for upward stopping muons: one simply has to replace $n_{\text{H}_2\text{O}}$ and $\sigma_{\text{CC}}^{\nu_\mu \, \text{H}_2\text{O}}$ by n_{Rock} and $\sigma_{\text{CC}}^{\nu_\mu \, \text{Rock}}$ as in this event class the muons are produced in the rock surrounding the detector. This also implies that the space integration runs over the volume of the rock rather than the detector. The

energy loss of muons in rock is given in table IV-6 of [147]. Further, the function δ^{FC} has to be replaced by an appropriate δ^{Stop} which cuts out events not passing the momentum or the angular cut (remember that only muons traveling in the upward direction are accepted). For simplicity, we assume that the rock consists entirely of silicon and determine the number density as $n_{\mathrm{Rock}} = \rho_{\mathrm{Rock}}/m_{\mathrm{Si}}$ with the density of standard rock $\rho_{\mathrm{Rock}} = 2.65\,\mathrm{g\,cm^{-3}}$ [147] and the silicon mass $m_{\mathrm{Si}} = 26.1\,\mathrm{GeV}$. Note, however, that the actual composition of rock is almost irrelevant as long as the overall neutron to proton ratio is kept fixed. This is because the charged current cross section of neutrinos on a nucleus with mass number A and proton number Z scales – up to very small corrections – as $\sigma_{\mathrm{CC}}^{\nu_\mu\,\mathrm{A}} = Z\,\sigma_{\mathrm{CC}}^{\nu_\mu\,p} + (A - Z)\,\sigma_{\mathrm{CC}}^{\nu_\mu\,n}$.

As a cross-check for our approach we used the HKKMS fluxes [148] to calculate the (non-oscillated) prediction for fully contained events and upward stopping muons from atmospheric neutrinos in Super-Kamiokande I. We find good agreement with [146] concerning the overall normalization and the zenith angle distribution of events. In the fully contained case we systematically underestimate the event number by a few percent. This is exactly what we expect from our implementation of the event cuts (see above) and only makes our analysis slightly more conservative.

4.1.4 Constraints on Dark Matter from Super-Kamiokande

The dominant background for neutrinos from dark matter annihilation are atmospheric neutrinos as they are comparable in energy. Super-Kamiokande is able to measure the angle under which a muon is produced. As muons inherit to some extent the direction of flight from the parent neutrino, one has a handle to distinguish the two sources. By accepting only muon tracks in a small cone around the sun-earth direction, e.g. $\theta_{\mu\odot} < 30°$, the atmospheric background can be efficiently suppressed.[2] This is simply because for neutrinos from the sun $\theta_{\mu\odot} = \theta_{\mu\nu}$ while there is no such correlation for atmospheric neutrinos.

In this work we will use the data sets from the Super-Kamiokande runs I, II and III taken between 1996 and 2007. The number of fully contained (muon-like) events observed at Super-Kamiokande can be taken from figure 1 in [149].[3] We extract that 8596 events of this type have been observed during the time $t^{\mathrm{FC}} = 2806$ d, the Monte Carlo prediction for atmospheric neutrino events was 8610. Unfortunately, there exist no publicly available information on the distribution of events with respect to the angle between muon and sun. Therefore, we set our constraints by use of the total event

---

[2]While for $E_{\nu_\mu} > 10\,\mathrm{GeV}$ neutrino and muon can be considered collinear, their relative angle remains small ($\theta_{\mu\nu} \lesssim 30°$) even for E_{ν_μ} in the GeV range.

[3]The Monte Carlo prediction was calculated for the neutrino oscillation parameters set to the best-fit-point of the Super-Kamiokande analysis. A slight variation of θ_{13} would, however, only marginally affect the prediction as can be seen in the same figure.

number. As atmospheric neutrinos alone are perfectly sufficient to explain the data, we can only put an upper limit on the dark matter induced event rate of stopping muons. Using Poisson statistics the limit at 90% confidence level reads

$$R_{\mathrm{max}}^{\mathrm{FC}} = 13.8\,\mathrm{yr}^{-1}\ . \tag{4.27}$$

The predicted event rate is given by (4.26).

For upward stopping muons the distribution of events with respect to the angle $\theta_{\mu\odot}$ was published in [150, 151]. We restrict our analysis to events with $\theta_{\mu\odot} \leq 30°$, for which the observed number during a run time of $t^{\mathrm{Stop}} = 2828$ d was 53, the Monte Carlo atmospheric neutrino prediction 54 (see figure 1 of [151]). The data are consistent with atmospheric neutrinos, we can again only provide an upper limit $R_{\mathrm{max}}^{\mathrm{Stop,\,30°}}$ on the dark matter induced event rate of stopping muons with $\theta_{\mu\odot} \leq 30°$. The 90% Poissonian upper limit on the rate of dark matter induced stopping muons with $\theta_{\mu\odot} \leq 30°$ takes the value

$$R_{\mathrm{max}}^{\mathrm{Stop,\,30°}} = 1.24\,\mathrm{yr}^{-1}\ . \tag{4.28}$$

The predicted event rate is given by (4.26) with the modifications discussed in section 4.1.3.3 and the $\mathrm{d}\cos\theta_{\mu\nu}$ integration running from $\cos(30°)$ to 1 rather than from -1 to 1.

The limits (4.27) and (4.28) translate into constraints on the WIMP proton cross section which depend on the annihilation channel. We will consider the standard scenario of WIMPs with spin-independent isospin conserving interactions. Additionally, we include the case of isospin violating couplings $f_n = -0.7f_p$ and of spin-dependent interactions. We assume a thermal WIMP annihilation cross section (c.f. figure 2.6) and treat separately the cases of s-wave and p-wave annihilation. The combined limits from fully contained events and upward stopping muons are shown together with confidence regions of DAMA, CoGeNT and CRESST in figure 4.3. For the spin-dependent case we have set the WIMP neutron coupling a_n to zero. A non-zero coupling to neutrons would affect the DAMA confidence region but virtually not the Super-Kamiokande limits (as WIMP capture in the sun is dominated by hydrogen) .

First notice the general shape of the Super-Kamiokande limits: at low WIMP mass the limits arise from fully contained events, at higher WIMP mass from upward stopping muons. Below the evaporation mass all constraints disappear rapidly as the annihilation signal becomes highly suppressed. In general, the constraints are much stronger for WIMP annihilation into neutrinos or taus than for annihilation into quarks.

For spin-independent scattering with $f_n = f_p$ Super-Kamiokande excludes thermal WIMPs with $m_\chi \lesssim 20\,\mathrm{GeV}$ as a source of the DAMA, CRESST and CoGeNT modulation signal if they dominantly annihilate into taus or neutrinos – unless the annihilation cross section is velocity suppressed. This mass region is of utmost importance as the direct detection constraints on light WIMPs, especially from XENON, are subject to
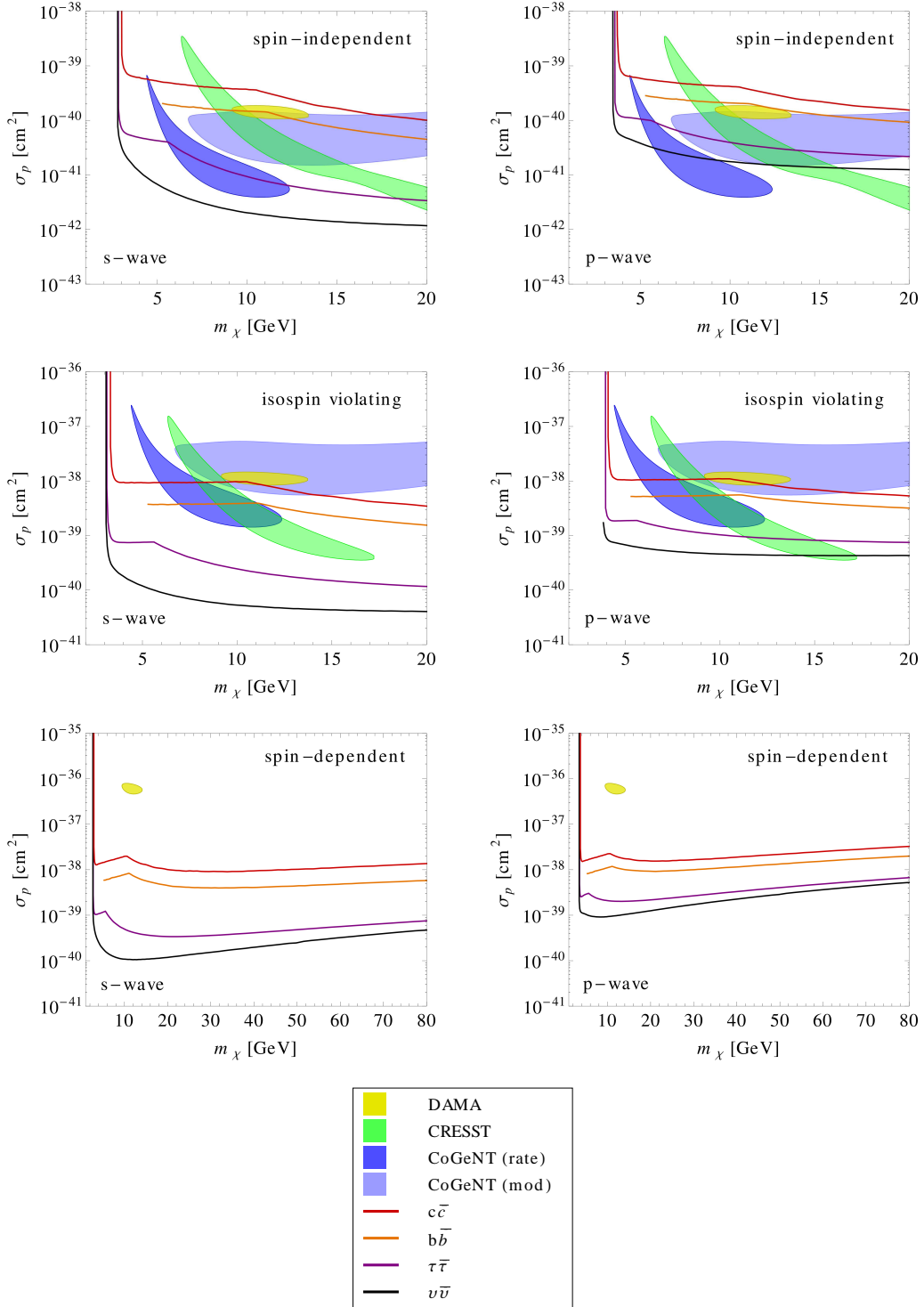
Figure 4.3: The Super-Kamiokande 90% upper limits on the WIMP proton cross section for spin-independent interactions with $f_n = f_p$ (top), $f_n = -0.7 f_p$ (middle) and for spin-dependent interactions. The colors refer to the different WIMP annihilation channels (see legend). S-wave (p-wave) annihilation with a thermal cross section is assumed in the left (right) panels. Also shown are the 90% confidence regions for the direct detection experiments DAMA, CoGeNT and CRESST.

uncertainties (see section 3.3.4). Even for pure p-wave annihilation the DAMA region remains excluded for the two leptonic channels. If the WIMPs annihilate into quarks, the constraints are not yet competitive.

Super-Kamiokande is even more powerful in constraining isospin violating interactions with $f_n = -0.7 f_p$ which were suggested to reconcile the direct detection experiments (see section 3.3.4). For this case, even WIMPs annihilating into the heavy quark species are already at the border of being excluded at least as a source of the DAMA signal. Any explanation for DAMA, CoGeNT and CRESST by WIMPs annihilating into taus or neutrinos is disfavored even for pure p-wave annihilation.

Turning to spin-dependent scattering, the Super-Kamiokande constraints are stronger than those from direct detection for all considered annihilation channels. Especially, a spin-dependent explanation for the DAMA modulation signal is ruled out for WIMPs which annihilate into neutrinos, taus, bottoms or charms, even if the branching fraction is only at the few percent level.

4.2 Antiproton Searches

Neutrino telescopes are sensitive to the tau and neutrino annihilation channels of dark matter. However, for hadronic annihilation the neutrino signals are suppressed and the corresponding constraints are rather weak. On the other hand, in the quark channels a large number of protons and antiprotons is produced during the hadronization process. Charged particles produced in the sun are efficiently stopped and cannot be detected in the vicinity of the earth. However, dark matter annihilations should take place everywhere in the halo surrounding our galaxy. The so-produced protons and antiprotons propagate through the interstellar space and are potentially observable at the earth. In this work we will focus on the antiprotons as the cosmic ray background is substantially lower for antiparticles than for particles. This analysis is based on [152].

4.2.1 Galactic Antiproton Sources

Dark matter annihilations or primordial black holes could be primary sources of antiprotons in our galaxy. While their existence is speculative, the presence of so-called secondary antiprotons is well-established. Their origin lies in the spallation of primary cosmic rays – mainly protons and helium – on the interstellar matter. Balloon and satellite experiments like BESS [153–156], AMS [157] and PAMELA [158] have measured the antiproton flux at the earth, their results are consistent with a purely secondary origin (see e.g. [29,30]) . The experimental situation has, however, recently improved substantially due to the BESS-Polar II antarctic flight [31]. The latter is a dedicated balloon experiment with high sensitivity to antiprotons with kinetic energy $T = 0.2 - 3.5\,\text{GeV}$. With the better precision of the experimental data a reliable parametrization of the

secondary background is indispensable. Therefore, we will now reevaluate the secondary antiproton flux in the standard 2-zone diffusion model of Donato et al. [159]. Different from previous works, we consider a novel determination of the secondary source term [33] and take into account recent updates on the propagation parameters [32].

4.2.1.1   Secondary Antiproton Background

Primary cosmic rays stem from interstellar particles which are accelerated by the magnetic shock waves associated with Supernova explosions [160]. The dominant components of cosmic rays are protons and helium. If they undergo inelastic interactions with nuclei in the interstellar gas, secondary particles including antiprotons may be created. The secondary antiproton source term, which describes the differential $\bar{p}$ production rate in the galactic disc per volume, time and energy, reads

$$q_{\bar{p}}^{\text{sec}}(T) = 2 \sum_{A,\,A'} 4\pi \int\limits_{E_{\text{th}}}^{\infty} \text{d}T' \left(\frac{\text{d}\sigma}{\text{d}T}\right)_{A+A'_{\text{ISM}} \to \bar{p}+X} n_{A'_{\text{ISM}}} \Phi_A(T') \,, \tag{4.29}$$

where the sum runs over the nuclear species A and A' which are present in cosmic rays and the interstellar matter (ISM). The factor of two on the right hand side accounts for $\bar{p}$ production by anti-neutron decay; the threshold energy is given by $E_{\text{th}} = 6\,m_p$. The differential cross section for the reaction $A+A'_{\text{ISM}} \to \bar{p}+X$ is expressed in terms of the kinetic energies T' and T of the incoming nucleus and the outgoing antiproton respectively. In this work we will only consider protons and helium as the interstellar density of heavier nuclei is highly suppressed. The cosmic ray fluxes Φ_p and Φ_{He} can be extracted from [161–163]. The primary fluxes are taken to be constant in the galactic disc. We have verified that the inclusion of the position-dependence would only marginally affect the local secondary antiproton flux.[4] The interstellar densities are taken from [159] ($n_{p\,\text{ISM}} \simeq 0.9\,\text{cm}^{-3}$, $n_{\text{He}\,\text{ISM}} \simeq n_{p\,\text{ISM}}/10$).

The main source of uncertainty for the secondary production arises from the parameterization of the antiproton production cross sections. Proton-proton collisions have been excessively studied at colliders and a reliable analytic expression for the cross section $\sigma_{p+p \to \bar{p}+X}$ exists [166, 167]. In early approaches interactions involving helium were treated in form of a simple energy-independent enhancement factor (see e.g. [168, 169]). This approximation is, however, insufficient as the helium cross sections scale markedly different with energy compared to $\sigma_{p+p \to \bar{p}+X}$. At very low energies antiprotons stem even dominantly from proton helium collisions [33]. In [159, 170] the calculation of cross sections was improved by use of the DTUNUC model. In this work we prefer, however, the semi-analytic ansatz of [33, 171] where cross sections are obtained by fitting

---

[4]The radial dependence of the proton and helium fluxes can be obtained from the Supernova remnant distribution in our galaxy (see e.g. [164, 165]).

the parameterization of Kalinovski et al. [172] to the available experimental data. This method seems more reliable towards lower $\bar{p}$ energies where the DTUNUC model reaches the edge of its validity [33]. The source term can be extracted from figure 9 in [33], a good fit in the range $T = 0.1 - 100\,\mathrm{GeV}$ is given by

$$q_{\bar{p}}^{\mathrm{sec}}(T) = \left(\frac{5.72 \cdot 10^{-30}}{\mathrm{cm}^3\,\mathrm{s}\,\mathrm{GeV}} \right) \times \exp \left\{ \sum_{n=1}^{5} c_n \left[\log \left(\frac{T}{\mathrm{GeV}} \right) \right]^n \right\} , \tag{4.30}$$

with $c_1 = 0.98$, $c_2 = -0.72$, $c_3 = -0.021$, $c_4 = 0.023$ and $c_5 = -0.0021$.

4.2.1.2   Primary Antiprotons from Dark Matter Annihilation

Antiprotons can efficiently be generated by annihilations of WIMPs if their daughter particles involve quarks or gauge bosons. We will consider the channels

$$\chi\chi \to u\bar{u},\, d\bar{d},\, s\bar{s},\, c\bar{c},\, b\bar{b},\, WW,\, ZZ . \tag{4.31}$$

The antiproton energy spectra per annihilation $\mathrm{d}N_{\bar{f}f}^{\bar{p}}/\mathrm{d}T$ in a given channel $\bar{f}f$ are again obtained with the PYTHIA Monte Carlo. We assume 100% annihilation into one channel but one can simply rescale our results with the appropriate branching ratio. Annihilation into tops is omitted as the focus of this analysis is on WIMPs with mass $m_\chi < 200\,\mathrm{GeV}$. Leptonic channels are not included as they do not give rise to an appreciable antiproton production.

The primary antiproton source term at the distance r from the galactic center can be expressed as

$$q_{\bar{p}}^{\mathrm{prim}}(r, T) = \frac{\rho_\chi^2(r)}{m_\chi^2} \frac{\langle \sigma v_{\mathrm{rel}} \rangle_0}{2} \frac{\mathrm{d}N_{\bar{f}f}^{\bar{p}}}{\mathrm{d}T} . \tag{4.32}$$

For the dark matter density we use a Navarro-Frenk-White profile (c.f. (2.13b)) with the parameters from table 2.1. The primary antiproton flux depends quadratically on the local dark matter density, but is virtually insensitive to the choice of the profile. The dark matter annihilation cross section $\langle \sigma v_{\mathrm{rel}} \rangle_0$ averaged over the current velocity distribution (indicated by the index 0) is a free parameter. For thermal WIMPs with s-wave annihilation the cross section is given by the left panel of figure 2.6. For p-wave annihilation the cross section is several orders of magnitude smaller as WIMPs today move much slower than at the time of freeze-out. Therefore, only in the s-wave case appreciable antiproton signals are expected.

4.2.2   Propagation

Antiprotons on their way through the galaxy are affected by various processes which are encoded in the so-called diffusion equation. The latter determines the local flux of antiprotons induced by the sources discussed previously.

4.2.2.1 The Diffusion Equation

If we assume steady state, the diffusion equation can be written in the form [173]

$$\vec{\nabla}(-K\,\vec{\nabla}N_{\bar{p}} + \vec{V}_c\,N_{\bar{p}}) + \partial_T(b_{\text{tot}}\,N_{\bar{p}} - K_{EE}\,\partial_T N_{\bar{p}}) + \Gamma_{\text{ann}}\,N_{\bar{p}} = q_{\bar{p}}^{\text{prim}} + q_{\bar{p}}^{\text{sec}} + q_{\bar{p}}^{\text{tert}} \ , \quad (4.33)$$

where $N_{\bar{p}}$ denotes the antiproton space-energy density. The first term on the left hand side accounts for diffusion on inhomogeneities of the galactic magnetic field. The galactic wind with the velocity vector $\vec{V}_c$ induces convection. The subsequent terms which contain derivatives with respect to the kinetic energy treat energy losses and reacceleration, the last term on the left hand side is due to the disappearance of antiprotons through annihilations. The right hand side includes the primary and secondary antiproton source terms. Additionally, there is a tertiary source term which accounts for inelastic (non-annihilating) scatterings of primary and secondary antiprotons on the interstellar gas.

A full numerical approach to the diffusion equation was performed in [161, 164]. In this work we, however, use the two-zone diffusion model introduced by Donato et al. [159]. The latter employs a few simplifications which permit a semi-analytic solution the diffusion equation. It shall briefly be reviewed in the following.

The halo, in which diffusion and convection occurs, is approximated by a cylinder of half height L and radius R equal to that of the galactic disc, i.e. $R \simeq 20$ kpc. As a boundary condition, a sharp cut-off with vanishing $N_{\bar{p}}$ at the edge of the cylinder is imposed. The coordinate system is chosen such that the z-axis is perpendicular to the galactic disc with the galactic center at the origin. The thickness of the disc (half-height $h \simeq 0.1$ kpc) can be neglected compared to its radius. But in order to keep a proper normalization, all terms in (4.33) which are confined to the galactic disc have to be multiplied by $2\,h\,\delta(z)$. These include energy losses, reacceleration and annihilations as well as the secondary and tertiary source terms.

The diffusion parameter K is taken to be homogeneous over the halo. Magnetohydrodynamics considerations imply the form [174]

$$K = K_0\,\beta\,\left(\frac{p}{\text{GeV}}\right)^{\delta} \ , \quad (4.34)$$

where K_0 is a normalization constant, δ the power law index, β and p the antiproton velocity and momentum respectively. The galactic wind is assumed to be constant and pointing away from the disc, i.e. $\vec{V}_c = \text{sign}(z)\,V_c\,\hat{z}$ with $\hat{z}$ being the unit vector in z-direction.

The term b_{tot} which we take from [175] includes ionization, Coulomb and adiabatic energy losses as well as reacceleration. The latter is related to the Alfvèn speed V_a of magnetic shock waves in the galactic disc. The energy diffusion coefficient is also related to reacceleration, we use the revised form [176]

$$K_{EE} = \frac{4}{3\,\delta\,(4-\delta^2)(4-\delta)}\,V_a^2\,\frac{\beta^2\,p^2}{K} \ . \quad (4.35)$$

The disappearance rate of antiprotons through annihilations with the interstellar protons or helium can be parameterized as $\Gamma_{\text{ann}} = (n_{p\,\text{ISM}} + 4^{2/3}\, n_{\text{He\,ISM}})\, \sigma_{\text{ann}}\, \beta$ with [167, 177]

$$\sigma_{\text{ann}} = \begin{cases} 661\,\text{mb} \times \left(1 + 0.0115\left(\frac{T}{\text{GeV}}\right)^{-0.774} - 0.948\left(\frac{T}{\text{GeV}}\right)^{0.0151}\right) & T < 14.6\,\text{GeV}\,, \\ 36\,\text{mb} \times \left(\frac{T}{\text{GeV}}\right)^{-0.5} & T \geq 14.6\,\text{GeV}\,. \end{cases}$$
(4.36)

The tertiary source term accounts for the redistribution of antiproton energies due to the inelastic (non-annihilating) scattering with the interstellar gas in the disc. It can be written as

$$q_{\bar{p}}^{\text{ter}}(\mathbf{r}, T) = (n_{\text{p\,ISM}} + 4^{2/3}\, n_{\text{He\,ISM}})$$
$$\times \left(\int_T^\infty dT'\, \frac{d\sigma_{\text{non-ann}}}{dT}\, \beta'\, N_{\bar{p}}(\mathbf{r}, T') - \sigma_{\text{non-ann}}\, \beta\, N_{\bar{p}}(\mathbf{r}, T)\right)\,,$$
(4.37)

where primed (unprimed) quantities refer to the antiprotons before (after) scattering while $\mathbf{r}$ denotes the radial distance[5] from the galactic center. The non-annihilating cross section can be extracted from [167].

For the full solution to the diffusion equation for secondaries and primaries we refer to the appendices A.1 and A.2. The interstellar antiproton flux is related to the space-energy density by

$$\Phi_{\bar{p}}^{\text{IS}} = \frac{1}{4\pi}\, \beta\, N_{\bar{p}}\,.$$
(4.38)

4.2.2.2 Propagation Parameters

The solution to the diffusion equation depends on the five propagation parameters K_0, δ, L, V_c and V_a which can partly be fixed by observing the nuclear composition of cosmic rays. In [32, 176, 178] the configurations which correctly reproduce the boron to carbon (B/C) ratio were determined. Unfortunately, due to a degeneracy in the propagation parameters the size of the diffusion halo L is only weakly constrained by the B/C ratio. However, in the last years several complementary techniques have been employed to determine L. These include the observation of radioactive isotopes in cosmic rays [32] as well as studies of radio data from the galactic anti-center [179] and of the diffuse gamma ray background [180] (see also [181] and references therein). As all these studies suggest $L \geq 4\,\text{kpc}$, we will adopt $L = 4\,\text{kpc}$ in the following and take the remaining propagation parameters from the recent B/C analysis [32] (NORM configuration in table 4.1). To be conservative we will also consider a smaller $L = 3\,\text{kpc}$ where we adjust the other parameters according to figure 5 in [32] (SMALL configuration in table 4.1).

---

[5]Note that we are using cylindrical coordinates here. Therefore, the radial distance $\mathbf{r}$ should not be confused with the total distance r. The two quantities are related by $r^2 = \mathbf{r}^2 + z^2$.

model	δ	K_0 (kpc$^2 \cdot$ Myr^{-1})	L (kpc)	V_c (km $\cdot$ s^{-1})	V_a (km $\cdot$ s^{-1})
NORM	0.86	0.0042	4	18.7	35.5
SMALL	0.86	0.0031	3	18.6	30.5

Table 4.1: Propagation parameters consistent with the B/C ratio.

The secondary antiproton flux is only mildly affected by uncertainties in the propagation parameters, especially the choice of L. This is different for primaries which are produced everywhere in the halo and not just in the galactic disc. To discuss this in more detail, we neglect for the moment low energy effects on antiprotons – namely energy losses, reacceleration and tertiaries. This allows us to write the primary antiproton space energy density in the simple form (see appendix A.2)

$$N_{\bar{p}}^{\text{prim}} \simeq q_{\bar{p}}^{\text{prim}}(r_\odot, T) \, \mathcal{R}_\odot \; , \tag{4.39}$$

where $\mathcal{R}_\odot$ denotes the propagation function. Note that we only use this estimate to illustrate the impact of the propagation parameters. In our analysis we will always use the full solution to the diffusion equation.

In figure 4.4 we depict $\mathcal{R}_\odot$ for the NORM and the SMALL configurations. To allow for comparison with earlier work we also show the propagation functions for the commonly used MIN, MED and MAX configurations [182] which make use of the propagation parameters derived in an earlier B/C analysis [178].[6]
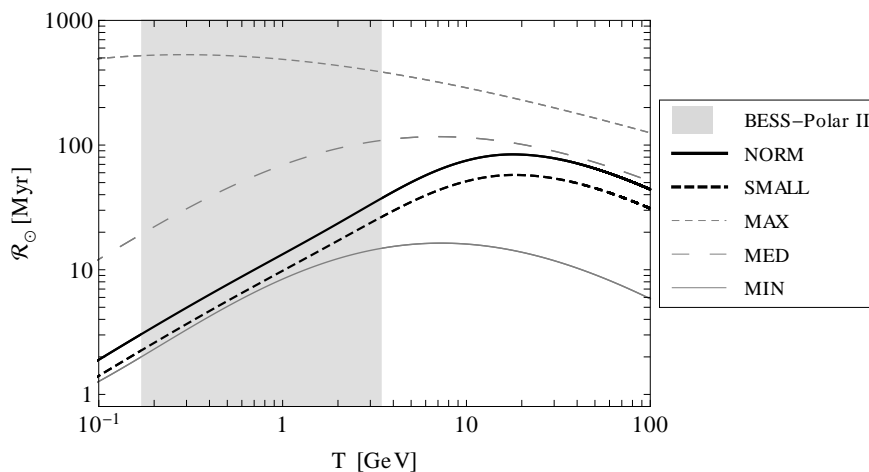

Figure 4.4: Propagation function for different choices of the propagation parameters. The NORM and SMALL configurations are used in this work. They were derived from a more recent B/C analysis [32] compared to MIN, MED and MAX. The shaded band refers to the energy range of BESS-Polar II.

---

[6]The propagation function for the MIN, MED and MAX configurations was extracted from [71].

At high energies cosmic ray propagation is dominated by diffusion, the primary fluxes grow with the size of the halo. The propagation functions for the NORM and MED configurations come very close as they both have $L = 4\,\text{kpc}$. The MIN (MAX) configuration employs a halo size of $L = 1\,\text{kpc}$ ($L = 15\,\text{kpc}$) and the corresponding $\mathcal{R}_\odot$ is considerably smaller (larger) compared to the other configurations. Note, however, that such extreme values for L are now strongly disfavored especially by radio data [179]. At low energies, the process of convection rapidly gains importance. As suggested by the new B/C analysis [32], NORM and SMALL assume a larger galactic wind than MIN, MED and MAX. Correspondingly, the propagation functions for NORM and SMALL decrease more rapidly towards low energies. In the energy range of BESS-Polar II – indicated by the shaded band in figure 4.4 – we therefore obtain primary antiproton fluxes in our analysis which are similar to those in the MIN configuration.

4.2.2.3 Solar Modulation

In the previous sections we have discussed the propagation of antiprotons through the galaxy. The interstellar antiproton flux $\Phi_{\bar{p}}^{\text{IS}}$ can be obtained by use of the diffusion equation. Satellite and balloon experiments, however, measure the antiproton flux at the top of the earth atmosphere $\Phi_{\bar{p}}^{\text{TOA}}$. The latter is affected by the rapidly changing magnetic fields in the heliosphere (solar modulation). In principle, one can define a new diffusion equation to describe the propagation of antiprotons from outside the solar system to the earth. This, however, turns out to be quite challenging as the evolution of the magnetic fields is extremely complicated and correlated with the solar activity. The transport parameters change with time and are only partly accessible to experiments.

The best analytic description of solar modulation is currently achieved in drift models like those presented in [183, 184]. It turns, however, out that in periods of lowest solar activity the predictions from these sophisticated models converge with the much simpler force-field approximation [185, 186]. The latter relates the interstellar and the top-of-the-atmosphere antiproton flux as

$$\Phi_{\bar{p}}^{\text{TOA}}(T) \simeq \frac{2\,m_{\bar{p}}\,T + T^2}{2\,m_{\bar{p}}\,(T + \phi) + (T + \phi)^2}\, \Phi_{\bar{p}}^{\text{IS}}(T + \phi)\,. \tag{4.40}$$

For a given experiment the value of the force-field ϕ can be determined through observation of the proton flux as particles and antiparticles are modulated in the same way. Note, however, that this only holds if the force-field approximation is applicable as, in general, drift effects introduce a charge sign dependence into solar modulation.

4.2.3 Comparison with Experimental Results

We will now turn to a comparison of the calculated antiproton flux with the available experimental data. Thereby, we will first consider the secondary antiproton background

in order to check whether secondaries are already sufficient to explain the measurements or whether there is need to include primaries from dark matter annihilation.

4.2.3.1 Secondary Flux

The best-precision search for antiprotons in the GeV range was performed by BESS-Polar II. The latter consists of a high resolution magnetic-rigidity spectrometer attached to a balloon. It was launched in December 2007 from Williams Field in the Antarctica and took data for 24.5 days in an altitude of 34 to 38 km. Around 8000 antiprotons were detected [31]. As the experiment was run during a short time period around the solar minimum, solar modulation can be accounted for by means of the force-field approximation. To determine the force field ϕ, we modulate the interstellar proton flux from [162] and compare it to the TOA proton flux at BESS-Polar II which can be extracted from [187]. In doing so we find $\phi = 0.5\,\mathrm{GV}$.

While the main focus of our analysis is on the BESS-Polar II data set we additionally include the antiproton search by PAMELA [158] to check against the secondary antiproton flux at energy $T > 5\,\mathrm{GeV}$. The value of the force field $\phi = 0.5\,\mathrm{GV}$ is also suitable for PAMELA. In figure 4.5 we depict the measured TOA antiproton fluxes from the two experiments and the antiproton flux from our calculation.[7] For comparison, we have also included the secondary flux from the original work of Donato et al. [159, 175]. For the latter, we also show the nuclear physics uncertainty band which accounts for the fact that the total antiproton production cross sections are not fixed within the DTUNUC model. This results in an uncertainty in the normalization of the secondary flux.

First note, that the antiproton flux measured by PAMELA is slightly higher compared to BESS-Polar II which might have its origin in solar modulation. The $\bar{p}/p$ ratio at PAMELA is, however, also larger than at BESS-Polar II (see [187]). Therefore the difference cannot be explained within the force-field approximation. On the other hand, the more sophisticated drift models [183, 184] predict an increase of the $\bar{p}/p$ ratio at higher solar activity. While BESS-Polar II was operating in a short time window around the solar minimum, PAMELA took its data from 2006 to 2008, i.e. partly at intermediate solar activity. Therefore, the small discrepancy between PAMELA and BESS-Polar II may originate from drift effects. Similar variations in the e/p ratio correlated with the solar activity were also measured by the Ulysses spacecraft (see e.g. [188] and the discussion in [189]). As we use the PAMELA data only for illustration our analysis is not affected by the corresponding uncertainties.

It can, further, be seen that the shape of the secondary antiproton flux from our calculation deviates from that of Donato et al. [159, 175] although our calculation is based on the same propagation setup. The main reason for this is that we used a different

---

[7]The secondary antiproton fluxes for the NORM and SMALL configurations are virtually indistinguishable. Therefore, they are not discussed separately.
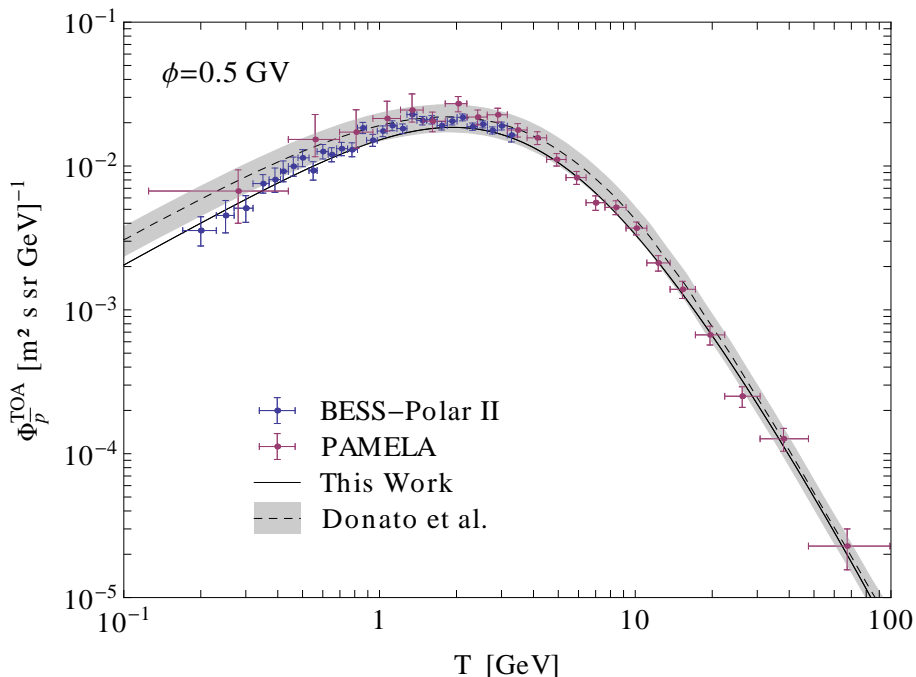
Figure 4.5: TOA antiproton flux measured by BESS-Polar II and PAMELA together with the predicted secondary flux from our calculation (solid) and from Donato et al. [159, 175] (dashed). For the latter we also show the nuclear physics uncertainty band (shaded). Solar modulation is included through the force field approximation with $\phi = 0.5$ GV.

source term compared to Donato et al. which is smaller especially towards low energies (see discussion in section 4.2.1.1). Further, we took the propagation parameters from the recent B/C analysis [32] which especially suggests a higher galactic wind velocity V_c than assumed in [159, 175]. This also leads to a slight decrease of the local flux towards low energies as more antiprotons can escape from the halo via convection.

The spectral shape of $\Phi_{\bar{p}}^{\mathrm{TOA}}$ from our calculation fits nicely to the measurement, while the flux of Donato et al. is a bit too shallow to well reproduce the low energy data points even if one allows for an arbitrary normalization factor (see also figure 3 in [31]). On average, our flux is slightly below the measured flux. A χ^2-analysis gives $\chi^2/\mathrm{d.o.f.} = 2.1$ and $\chi^2/\mathrm{d.o.f.} = 0.86$ if we would normalize our flux by a factor of 1.1. Note, however, that the small underestimation of the flux can partly be explained by the fact that we have neglected antiproton production on nuclei heavier than helium which may increase the antiproton flux by $\sim 5\%$ [170]. Further, the interstellar densities of p, He, the propagation parameters as well as our treatment of solar modulation are subject to uncertainties. Therefore – in agreement with [31] – we conclude that secondary antiprotons are sufficient to explain the experimental searches. Nevertheless, a small primary contribution to the antiproton flux is still conceivable and the latter shall be

constrained in the following. We restrict our analysis to BESS-Polar II which is more sensitive than PAMELA for WIMP masses $m_\chi \lesssim 200$ GeV. PAMELA limits on dark matter annihilation have been discussed in [30].

4.2.3.2   Primary Flux

As we have previously shown, consistency with the BESS-Polar II measurement requires any primary contribution to the antiproton flux to be subdominant. This raises the question, whether the annihilation of thermal WIMPs in the halo is already in tension with the experimental data. The answer depends on the WIMP mass and on the annihilation channel. Only WIMPs with hadronic annihilation give rise to measurable antiproton signals.
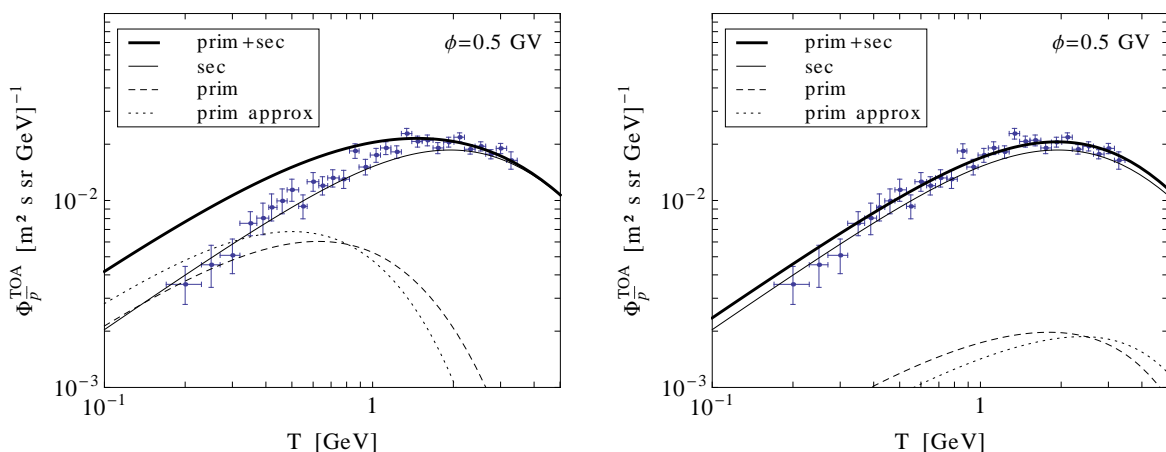

Figure 4.6: Secondary (sec), primary (prim) and total antiproton fluxes for the case of a WIMP annihilating into bottom quarks with mass $m_\chi = 8$ GeV (left) and $m_\chi = 30$ GeV (right). S-wave annihilation with a thermal cross section is assumed, where the latter can be extracted from figure 2.6. Propagation parameters are chosen according to the NORM configuration from table 4.1. Also shown are the primary fluxes without taking into account low energy effects (prim approx).

In figure 4.6 we show the primary antiproton flux expected from a thermal WIMP annihilating into bottom quarks, where we assume s-wave annihilation and consider two different masses. In order to illustrate the impact of energy losses, reacceleration and tertiaries, we also depict the primary flux without taking into account these low energy effects. This corresponds to the approximation (4.39) which is commonly employed in the literature. It can clearly be seen that it is indispensable to use the full solution to the diffusion equation, the approximation only provides a rough estimate. Note also that the low energy effects may – on average – either increase or decrease the antiproton energies depending on the steepness and the curvature of the injection spectrum.

We have also included the secondary and the total antiproton fluxes as well as the BESS-Polar II data points in figure 4.6. Apparently, the 8 GeV WIMP induces a primary flux inconsistent with the data. The 30 GeV WIMP is, however, still viable.

4.2.4 Constraints on Dark Matter from BESS-Polar II

We will now perform a quantitative analysis in order to provide constraints on the WIMP annihilation cross section for all relevant hadronic channels. One could in principle carry out a standard χ^2 analysis comparing the total predicted (primary + secondary) and the measured antiproton flux. However, we have pointed out in section 4.2.3.1 that the secondary antiproton flux alone is capable to explain the BESS-Polar II measurement, no primary component is required. Therefore, in our statistical test, we use a slightly modified version of the χ^2-metric which provides upper limits on the dark matter annihilations rather than inspecting the goodness-of-fit. We define

$$
\chi^2_{\mathrm{mod}} = \sum_i \begin{cases} \frac{\left(\Phi^{\mathrm{TOA}}_{\bar{p},i} - \Phi^{\mathrm{data}}_{\bar{p},i}\right)^2}{\sigma_i^2} & \Phi^{\mathrm{TOA}}_{\bar{p},i} > \Phi^{\mathrm{data}}_{\bar{p},i} \;, \\ 0 & \Phi^{\mathrm{TOA}}_{\bar{p},i} < \Phi^{\mathrm{data}}_{\bar{p},i} \;. \end{cases} \tag{4.41}
$$

Here $\Phi^{\mathrm{TOA}}_{\bar{p},i}$ denotes the predicted flux averaged over the bin i, $\Phi^{\mathrm{data}}_{\bar{p},i}$ the measured flux and σ_i the statistical error in the bin.

The difference of χ^2_{mod} compared to an ordinary χ^2 is that it only punishes a given configuration if the total flux exceeds the data. This implies that χ^2_{mod} does not follow an ordinary χ^2 probability distribution. For 29 d.o.f. (the number of energy bins of BESS-Polar II) the 95% upper limit corresponds to $\chi^2_{\mathrm{mod}} = 25.5$.

In figure 4.7 we provide 95% upper limits on the current dark matter annihilation cross section $\langle \sigma v_{\mathrm{rel}} \rangle_0$ for the hadronic channels. We have restricted our attention to WIMP masses in the range $m_\chi = 3 - 200 \, \mathrm{GeV}$. For lower m_χ the hadronization process cannot be reliably traced due to threshold effects in the antiproton production. For higher m_χ the PAMELA antiproton search, which we do not consider in our analysis, becomes more powerful than BESS-Polar II.

We consider separately the two sets of propagation parameters from table 4.1. In the NORM configuration the size of the diffusion halo is set to $L = 4 \, \mathrm{kpc}$ compared to $L = 3 \, \mathrm{kpc}$ in the SMALL configuration. The smaller diffusion halo results in the more conservative constraints. For comparison we also show the annihilation cross section of a thermal WIMP assuming s-wave annihilation. Note that no competitive constraints on dark matter annihilations can be set if the latter are velocity-suppressed. This is because the WIMP velocities in the halo are highly suppressed compared to at the time of freeze-out.

It can be seen that a thermal WIMP with s-wave annihilation into quarks is excluded in the mass range $3 - 20 \, \mathrm{GeV}$ even in the SMALL configuration. The limits for the light
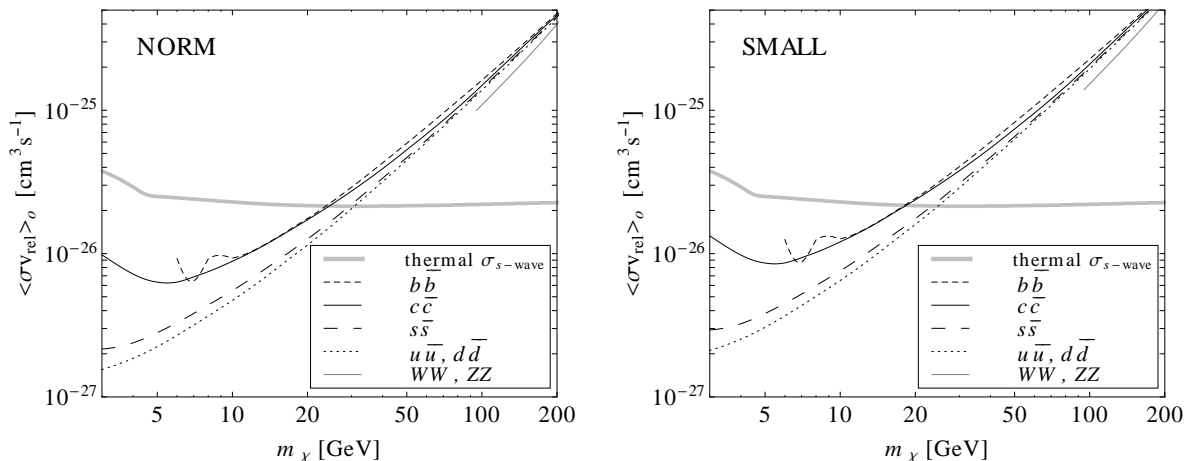
Figure 4.7: Limits (95% confidence level) on the present dark matter annihilation cross section for various hadronic annihilation channels (see legend). Propagation parameters are chosen according to the NORM (left panel) and SMALL (right panel) configurations from table 4.1. The thick gray line refers to the annihilation cross section of a thermal WIMP in the case of s-wave annihilation (see text).

quark channels are stronger than for the bottom and charm channels, especially towards low WIMP masses. The reason is that the antiproton generation by heavy quarks is less efficient as the latter must first undergo family transitions or accumulate light quarks. Additionally, due to the more indirect production, the antiprotons from heavy quarks typically have lower energies, i.e. more of them reside below the detection threshold.

Heavier dark matter particles may still give rise to an appreciable antiproton production. The primary antiproton flux from a WIMP with mass $m_\chi = 100$ GeV annihilating into W pairs is still to $\sim 30\%$ in the energy range of BESS-Polar II ($0.2 - 3.5$ GeV). However, the limits become weaker as the number density of dark matter is inversely proportional to its mass. Therefore, dark matter particles with $m_\chi > 30$ GeV can only be constrained if their annihilation cross section is enhanced compared to the thermal one. This can occur in scenarios with Sommerfeld enhancement or with non-thermal WIMPs.

4.3   Summary of Indirect Dark Matter Detection

Let us briefly summarize the constraints on dark matter annihilation from neutrino and antiproton searches: the Super-Kamiokande telescope excludes thermal WIMPs as a source of the DAMA, CoGeNT and CRESST excess if they dominantly annihilate into taus or neutrinos, while the BESS-Polar II antiproton search exclude any thermal WIMP with dominantly hadronic annihilations and mass $m_\chi = 3 - 20$ GeV. These statements hold as long as the annihilation cross section of dark matter is not velocity suppressed.

For p-wave annihilation the limits from antiproton searches are not competitive while the limits from neutrino searches get weaker by an $\mathcal{O}(1)$ factor. In the tau and neutrino channels an explanation to DAMA and CRESST is still in tension with the Super-Kamiokande data.

Apart from antiproton and neutrino searches there exist several complementary techniques of indirect dark matter detection. The FERMI-LAT collaboration has derived constraints on dark matter annihilations by investigating the corresponding gamma ray signals. In [190] they perform a combined analysis including 10 dwarf spheroidal galaxies. The limits on hadronic annihilations are slightly weaker than those from antiprotons for $m_\chi < 50\,\text{GeV}$, but, additionally, the tau channel can be constrained. In summary, the dwarf spheroidals exclude thermal WIMPs with mass $m_\chi = 5 - 15\,\text{GeV}$ and $m_\chi = 5 - 30\,\text{GeV}$ for s-wave annihilation into quarks and taus respectively.

Further, dark matter annihilations may modify the CMB power spectra [191–193]. By their energy injection around recombination they would enhance the fraction of free electrons which in turn increases the surface of last scattering. This leads to suppression of the power spectrum at scales smaller than the width of the last scattering surface. As this effect is not observed by WMAP one can again set limits on the dark matter annihilation cross section. Given a thermal cross section, these exclude WIMPs with mass $m_\chi = 1 - 8\,\text{GeV}$ if they annihilate into electrons [193], again with the exception of velocity suppression. The corresponding limits for the muon, tau and quark channels are slightly weaker as a significant fraction of the energy is carried away by neutrinos which do not affect the recombination [192].

Let us also mention some cosmic ray anomalies which have been interpreted as possible hints for light WIMPs. These include a gamma ray excess in an extended region around the galactic center [194–196]. The latter is consistent with WIMPs of mass $m_\chi = 7 - 12\,\text{GeV}$ or $m_\chi = 25 - 45\,\text{GeV}$ depending on whether their annihilation is dominantly leptonic or hadronic. The required cross section depends strongly on the dark matter density profile in the galactic center, but is roughly of the order of a thermal cross section. Extended gamma ray emission was also observed in several galaxy clusters and has been tentatively interpreted in terms of WIMPs with mass $m_\chi = 2 - 10\,\text{GeV}$ ($m_\chi = 20 - 60\,\text{GeV}$) which annihilate into muons (bottom quarks) [197]. Last but not least, the ARCADE-2 telescope [198] has measured an isotropic radio background significantly above expectation [199, 200]. In [201] the latter was found to be consistent with leptonically annihilating WIMPs of mass $m_\chi = 5 - 50\,\text{GeV}$. We should note, however, that an astrophysical origin of these signals can currently not be excluded (see [202–206]). Additionally, parts of the parameter space preferred by the dark matter explanation is already excluded by other searches (see above).

If we put the constraints on dark matter annihilations together, we find that thermal WIMPs are only viable as an explanation to the DAMA, CoGeNT and CRESST signals if they either

- annihilate dominantly into muons, electrons or particles outside the Standard Model, or

- their annihilation cross section is velocity-suppressed.

Finally, let us mention that the constraints from indirect detection are – although based on rather conservative assumptions – generally subject to astrophysical uncertainties. The constraints from antiproton searches depend quadratically on the local dark matter density which was calculated rather precisely in [72]. Nevertheless, there could occur systematic errors in the determination if the initial assumptions were not met. Further, the neutrino signal from Super-Kamiokande effectively depends on the capture rate averaged over the equilibration time scale. While the latter is assumed to be constant in our analysis, it could in principle vary with time if the shape of the dark matter halo deviated strongly from isotropy [207]. This could affect the Super-Kamiokande limits, especially for the case of p-wave annihilation where the equilibration time is large. The constraints from dwarf galaxies depend to some extent to the modeling of their dark matter profile.

But let us also point out that the uncertainties of the different indirect detection techniques are widely uncorrelated. In this sense, the exclusion of light thermal WIMPs with s-wave annihilation into quarks or taus seems rather robust as it appears as a result of independent indirect detection methods.

Chapter 5

A Supersymmetric Model with Light WIMPs

We will now present a particle physics model which offers a candidate for the light WIMPs possibly observed in direct detection experiments. The model is a supersymmetric extension of the Standard Model; the concept of Supersymmetry (SUSY) [208] shall briefly be reviewed in the following section. So-called singlinos are introduced as possible constituents of the dark matter. It is shown that – for a certain choice of parameters – their abundance from thermal production matches the dark matter abundance. Simultaneously, their cross section with nucleons is in the correct range to explain the signals of DAMA, CoGeNT and CRESST. We also consider constraints on the model from collider searches, flavor physics and indirect dark matter detection.

5.1   Supersymmetry and the MSSM

Supersymmetry extends the Poincaré group by new generators Q_α and $\bar{Q}_{\dot{\beta}}$ which schematically act on fermions and bosons as

$$Q|\text{Boson}\rangle = |\text{Fermion}\rangle\,, \qquad Q|\text{Fermion}\rangle = |\text{Boson}\rangle\,. \tag{5.1}$$

In contrast to the generators of internal groups, Q_α and $\bar{Q}_{\dot{\beta}}$ are Weyl spinors transforming in the $(1/2, 0)$ and $(0, 1/2)$ representations of the Lorentz group respectively. The transformation properties imply that fermions and bosons come in the same irreducible representations of Supersymmetry, i.e. a supersymmetric Lagrangian contains a bosonic superpartner for each fermion and vice versa. We will now briefly review the main motivation and some theoretical aspects of Supersymmetry. Then we construct the minimal supersymmetric extension of the Standard Model (MSSM).

5.1.1   Motivation for Supersymmetry

The Standard Model of particle physics describes our microphysical world with tremendous precision. The recent discovery of its last – so far undetected – component, the Higgs boson [209, 210], has completed its long history of success. At the same time, the Higgs boson is related to its deepest theoretical shortcoming: the hierarchy problem [211]. Its origin lies in the fact that the Standard Model does not offer a mechanism to protect scalar masses against large quantum corrections.
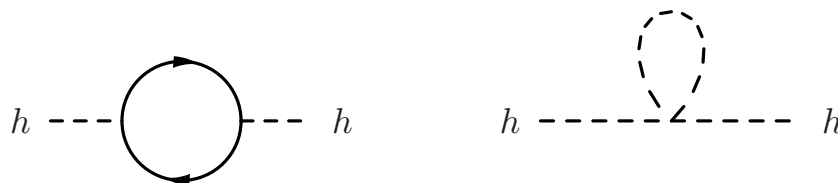

Figure 5.1: One-loop contribution to the Higgs mass from a fermion (left panel) and a scalar (right panel).

The one-loop contribution to the Higgs boson mass through the fermion loop in the left panel of figure 5.1 reads

$$\Delta m_h^2 = -\frac{y_f^2}{8\pi^2}\Lambda^2 + \mathcal{O}(\log\Lambda) , \tag{5.2}$$

where y_f is the Yukawa coupling of the fermion f and Λ the cut-off momentum used to regulate the loop-integral. If the Standard Model was the correct description of nature for energies up to the Planck scale, one would expect $\Lambda \sim M_P$. In order to obtain a Higgs boson mass $m_h \simeq 126$ GeV as suggested by [209, 210] one would thus have to invoke cancellations at the level of $1 : 10^{30}$ between the bare mass and the loop-induced mass.

In a supersymmetric theory fermions and bosons come in pairs. Thus, for the fermion f there is a complex scalar superpartner ϕ which couples to the Higgs boson via the term $-y_\phi h^2|\phi|^2$. The scalar – by the diagram in the right panel of figure 5.1 – induces another loop-correction to the Higgs mass

$$\Delta m_h^2 = \frac{y_\phi}{16\pi^2}\Lambda^2 + \mathcal{O}(\log\Lambda) . \tag{5.3}$$

Invariance of the action under SUSY transformations fixes the coupling $y_\phi = 2\,y_f^2$, i.e. the quadratically divergent contributions to the Higgs mass exactly cancel. This solution to the hierarchy problem is the main motivation for Supersymmetry.

5.1.2 Constructing Supersymmetric Lagrangians

The new SUSY generators Q_α and $\bar{Q}_{\dot{\beta}}$ fulfill anticommutation relations which extend the Lie-Algebra of the Poincaré group to a graded Lie algebra:

$$\left\{Q_\alpha, \bar{Q}_{\dot{\beta}}\right\} = 2\sigma^\mu_{\alpha\dot{\beta}} P_\mu \,, \tag{5.4a}$$

$$\left\{Q_\alpha, Q_\beta\right\} = \left\{\bar{Q}_{\dot{\alpha}}, \bar{Q}_{\dot{\beta}}\right\} = 0 \,, \tag{5.4b}$$

where P_μ is the four-momentum generator of spacetime translations and $\sigma^\mu = (1, \sigma^a)$ with σ^a being the Pauli matrices ($a = 1, 2, 3$). A supersymmetric Lagrangian must be constructed from the irreducible representations of the symmetry group (see e.g. [212]). These include the chiral Superfield $\Phi = (\phi, \psi, F)$ which contains a complex scalar ϕ, a chiral fermion ψ and an auxiliary field F, as well as the vector superfield $V = (A_\mu, \lambda, D)$ which consists of a gauge boson A_μ, a Majorana fermion λ and an auxiliary field D. In the Standard Model, fermions come in both chiralities, while in a supersymmetric theory it is conventional to use only left chiral fields. Right chiral fermions and their bosonic partners are expressed through their charge conjugate fields which are left chiral. The superfields have to be combined in such a way that the action remains invariant under SUSY transformations, i.e. the Lagrangian must transform into a total spacetime derivative.

In a globally supersymmetric and renormalizable[1] theory the interactions and masses of particles are determined by their properties under gauge transformations and by the superpotential $\mathcal{W}$. The latter is an analytic function of the scalar components of the left chiral superfields, its form is restricted by the symmetries of the theory. In a supersymmetric model, the scalar potential which contains all mass and interaction terms of the scalars ϕ_i can be written as

$$V(\phi_i, \phi_i^*) = |F_i|^2 + \frac{1}{2} D^a D^a \,, \tag{5.5}$$

where a is a gauge group index. The auxiliary fields F_i and D^a can be eliminated by their equations of motion which read

$$F_i^* = -\frac{\partial \mathcal{W}}{\partial \phi_i} \,, \tag{5.6a}$$

$$D^a = -g(\phi_i^* T_{ij}^a \phi_j) \,. \tag{5.6b}$$

Here the T^a are the generators of the gauge group. The Yukawa interactions between scalars and fermions follow from

$$\mathcal{L}_{\text{Yukawa}} = -\frac{1}{2} \frac{\partial^2 \mathcal{W}}{\partial \phi_i \, \partial \phi_j} \psi_i \psi_j + \text{h.c.} \,, \tag{5.7}$$

---

[1]In a non-renormalizable theory one must further consider the Kähler potential, a real function of the complex scalar fields.

where $\psi_{i,j}$ are the fermionic superpartners of $\phi_{i,j}$. We have implicitly used the contraction $\psi_i \psi_j = \psi_i^\alpha \epsilon_{\alpha\beta} \psi_j^\beta$ with the antisymmetric tensor ϵ. For the evaluation of Feynman diagrams it is sometimes useful to rewrite the Weyl fermions in terms of the four-component Majorana fermions $\Psi = (\psi_\alpha, \bar{\psi}^{\dot{\alpha}})$. The Yukawa terms then read

$$\mathcal{L}_{\text{Yukawa}} = -\frac{1}{2} \frac{\partial^2 \mathcal{W}}{\partial \phi_i \, \partial \phi_j} \bar{\Psi}_i \Psi_j \,. \tag{5.8}$$

Supersymmetric gauge interactions play a minor role for our analysis and we only refer to [212].

5.1.3 The MSSM

According to naive expectations, the minimal supersymmetric extension of the Standard Model should add the corresponding superpartners to its field content and contain all mass and interaction terms which are supersymmetric, gauge-invariant and renormalizable. However, it turns out that several modifications are required to arrive at a phenomenologically viable model.

Different from the Standard Model, the MSSM contains two Higgs doublets as in a supersymmetric theory Yukawa interactions with up- and down-type fermions cannot be mediated by the same Higgs field. The second Higgs doublet is also required by anomaly cancellation. The field content of the MSSM is listed in table 5.1.[2]

Invariance of the action under SUSY and gauge transformations would in principle allow for terms e.g. of the form $u_{\text{R}\,i}^c \, d_{\text{R}\,j}^c \, \widetilde{d}_{\text{R}\,k}^*$ and $Q_i \, L_j \, \widetilde{d}_{\text{R}\,k}^*$ (see e.g. [213]). These would induce rapid proton decay and wash out the baryon asymmetry in the early universe [214], unless the corresponding couplings were highly suppressed. In the MSSM one forbids these terms completely by introducing a new discrete symmetry called R-parity [6] under which the Standard Model particles transform even, their superpartners odd. A consequence of R-parity is that superpartners can only be produced in pairs. Further, the lightest superpartner (LSP) is stable and a promising dark matter candidate.

The superpotential of the MSSM with R-parity reads (see e.g. [213])

$$\mathcal{W}_{\text{MSSM}} = \bar{u} \, \boldsymbol{y}_u \, QH_u - \bar{d} \, \boldsymbol{y}_d \, QH_d - \bar{e} \, \boldsymbol{y}_e \, LH_d + \mu \, H_u H_d \,, \tag{5.9}$$

where we have introduced $\bar{u} = (\widetilde{u}_{\text{R}\,1}^*, \widetilde{u}_{\text{R}\,2}^*, \widetilde{u}_{\text{R}\,3}^*)$ and $Q, d, \bar{e}, L$ analogously. The Yukawa matrices in the quark and lepton sector are denoted by $\boldsymbol{y}_{u,d}$ and $\boldsymbol{y}_e$ respectively. The SU(2) indices of the doublets are contracted by the antisymmetric tensor ϵ.

Finally, Supersymmetry cannot be realized exactly in nature as it would require the Standard Model particles to be mass-degenerate with their superpartners – clearly in contradiction with observation. It is therefore suggestive to assume that SUSY is spontaneously broken by a mechanism similar to the Higgs mechanism of electroweak symmetry

---

[2]Note that right-handed fields are expressed through their charge conjugates.

Gauge sector

Name	Boson	Fermion	$(\mathrm{SU(3)_c},\mathrm{SU(2)_L})_Y$
B-boson, bino	B_μ^a	$\widetilde{B}$	$(\mathbf{1},\mathbf{1})_0$
W-boson, wino	W_μ^a	$\widetilde{W}^a$	$(\mathbf{1},\mathbf{3})_0$
gluon, gluino	G_μ^a	$\widetilde{g}^a$	$(\mathbf{8},\mathbf{1})_0$

Quark/Lepton sector

Name	Boson	Fermion	$(\mathrm{SU(3)_c},\mathrm{SU(2)_L})_Y$
slepton, lepton	$\widetilde{L}_i$	L_i	$(\mathbf{1},\mathbf{2})_{-1}$
	$\widetilde{e}_{\mathrm{R}\,i}^*$	$e_{\mathrm{R}\,i}^c$	$(\mathbf{1},\mathbf{1})_{+2}$
squark, quark	$\widetilde{Q}_i$	Q_i	$(\mathbf{3},\mathbf{2})_{+\frac{1}{3}}$
	$\widetilde{u}_{\mathrm{R}\,i}^*$	$u_{\mathrm{R}\,i}^c$	$(\overline{\mathbf{3}},\mathbf{1})_{-\frac{4}{3}}$
	$\widetilde{d}_{\mathrm{R}\,i}^*$	$d_{\mathrm{R}\,i}^c$	$(\overline{\mathbf{3}},\mathbf{1})_{+\frac{2}{3}}$

Higgs sector

Name	Boson	Fermion	$(\mathrm{SU(3)_c},\mathrm{SU(2)_L})_Y$
Higgs, higgsino	H_d	$\widetilde{H}_d$	$(\mathbf{1},\mathbf{2})_{-1}$
	H_u	$\widetilde{H}_u$	$(\mathbf{1},\mathbf{2})_{+1}$

Table 5.1: Fields of the MSSM with their gauge properties (representation under $\mathrm{SU(3)_c}$ and $\mathrm{SU(2)_L}$, hypercharge).

breaking. Due to phenomenological requirements, the MSSM fields can, however, not be the source of SUSY breakdown. Rather, our current understanding is that SUSY is broken in a new hidden sector of particles which is then transmitted to the MSSM either by messenger fields or by Planck suppressed operators. In the MSSM the effect of SUSY breaking is included by a so-called soft Lagrangian which comprises mass terms for the superpartners and the Higgs bosons as well as trilinear scalar interactions of the form $a_{ijk}\,\phi_i\phi_j\phi_k$, where a_{ijk} is a massive coupling [5]. This effective parameterization holds irrespective of the SUSY breaking scheme, but the relative size of the soft terms depends on it.

By electroweak symmetry breaking the neutral components of $H_u = (H_u^+, H_u^0)$ and $H_d = (H_d^0, H_d^-)$ receive vacuum expectation values (VEVs) $\langle H_u^0 \rangle = v_u$, $\langle H_d^0 \rangle = v_d$. One

introduces

$$\tan\beta = \frac{v_u}{v_d} \tag{5.10}$$

with $v_{\text{EW}} = \sqrt{v_u^2 + v_d^2} \simeq 174\,\text{GeV}$. It is convenient to decompose the neutral Higgs bosons into the CP even states h and H as well as the CP odd state a (the forth neutral degree of freedom is 'eaten up' by the Z boson). If $m_H \gtrsim 250\,\text{GeV}$ the lighter state h becomes Standard Model-like (MSSM decoupling limit). Note that electroweak symmetry breaking also induces mixing effects between particles with the same electric charge. The bino mixes with the neutral wino and higgsinos forming four neutralinos. Analogously the charged winos and higgsinos yield the so-called charginos.

5.1.4 Dark Matter in the MSSM

The MSSM contains several neutral superpartners, the neutralinos and the sneutrino. If one of them was the LSP, it could in principle play the role of dark matter. However, the sneutrino has full gauge strength interactions with nuclei which are mediated by the Z boson. Constraints from direct detection experiments therefore exclude the sneutrino as the dominant dark matter component. For the lightest neutralino this problem is absent as its coupling to the Z is typically suppressed. Even in simple supersymmetric settings there exist parameter regions where the thermal neutralino abundance matches the dark matter abundance [215, 216].

We now want to figure out whether MSSM neutralinos could be responsible for the signals observed by the direct detection experiments DAMA, CoGeNT and CRESST. This would require a mass $m \simeq 5 - 10\,\text{GeV}$ of the lightest neutralino and a cross section $\sigma_p = \mathcal{O}(10^{-40}\,\text{cm}^2)$ with protons. As discussed in the previous section, the lightest neutralino is a mixture of the gauginos and higgsinos. Due to the non-observation of charged winos and higgsinos at colliders and due to precision measurements of the Z boson width, a neutralino with mass $m \simeq 5 - 10\,\text{GeV}$ is only viable if it is dominantly composed of the bino. Still, a sizable higgsino admixture is required to enhance its annihilation cross section and the scattering cross section with nuclei. Otherwise, its abundance from thermal productions would exceed the dark matter abundance. Even with a significant higgsino component, the annihilation cross can only reach the thermal cross section if the pseudoscalar Higgs a is rather light ($m_a \lesssim 100\,\text{GeV}$) and $\tan\beta \gtrsim 50$. This would stimulate the annihilation into bottom quarks through an intermediate a. A cross section anywhere close to $\sigma_p = 10^{-40}\,\text{cm}^2$ requires both CP even Higgs bosons to be light. In [217–219] it was found that the corresponding parameter region is now ruled out by flavor constraints and Higgs searches.

5.2 A Singlet Extension of the MSSM

We will now turn to a simple extension of the MSSM in which we find a new light dark matter candidate in terms of a singlet fermion.

5.2.1 The Model

We consider the MSSM extended by a gauge singlet superfield S which contains a complex scalar s and a singlet fermion $\widetilde{s}$ (singlino). The superpotential for the Higgs sector of the model can be written as [220]

$$\mathscr{W} = \mu\, H_u H_d + \lambda\, s\, H_u H_d + \frac{\mu_s}{2}\, s^2 + \frac{\kappa}{3}\, s^3 \,. \tag{5.11}$$

Here we have neglected a possible linear term in s which can be absorbed into the quadratic and cubic terms. In the next-to-minimal supersymmetric Standard Model (NMSSM) one imposes an additional Z_3 symmetry which forbids the μ and μ_s terms. The NMSSM has the appealing feature that μ can be generated dynamically at the electroweak scale when the singlet scalar obtains a vacuum expectation value. In this sense it offers a solution to the so-called μ problem, the lacking explanation for the smallness of μ in the MSSM. Unfortunately, the breaking of the Z_3 symmetry at such a low scale gives rise to a disastrous cosmological domain wall problem [221].

In this work we do not employ the Z_3 symmetry and allow for the μ and μ_s terms in the superpotential. This has the advantage that the domain wall problem is automatically absent, but it seems to double the μ-problem of the MSSM. On the other hand, a superpotential of the form (5.11) has recently been obtained in the context of discrete R-symmetries [222]. In this scheme, suppressed μ and μ_s terms were explained by non-perturbative effects.[3]

In addition, we include the following soft terms

$$
\begin{aligned}
V_{\text{soft}} \;=\;& m_{H_u}^2\, |H_u|^2 + m_{H_d}^2\, |H_d|^2 + m_s^2\, |s|^2 \\
&+ \left(B\mu\, H_u H_d + \lambda\, A_\lambda\, s\, H_u H_d + \frac{B\mu_s}{2}\, s^2 + \frac{\kappa}{3}\, A_\kappa s^3 + \text{h.c.} \right) \,.
\end{aligned}
\tag{5.12}
$$

The interactions within the singlet sector are controlled by the coupling κ, those between the singlet and the MSSM sector by the parameter λ. In order to explain the direct detection signals, we are interested in the case where the singlino is light ($m_{\widetilde{s}} = 5 - 10\,\text{GeV}$). As we shall see, a sizable cross section of the singlino with nucleons further requires a correspondingly small mass for the lightest CP even scalar. In the absence of fine-tuning, such a situation can only arise if the coupling λ is suppressed. Otherwise the

---

[3]Note, however, that a large linear term in s which could destabilize the model [223] is not forbidden by the charge assignment given in [222], i.e. additional symmetries may be required to guarantee its absence.

interactions of h_s with the MSSM sector would pull the scalar masses to the electroweak scale. We will now focus on the region in parameter space where

- λ is suppressed, more precisely $\lambda \sim 10^{-3}...10^{-2}$,

- all singlet mass terms including μ_s^2, $B\mu_s$, m_s^2 are set by a scale $m_{\text{singlet}}^2 \sim (10\,\text{GeV})^2$.

Suppressed soft masses of singlets can e.g. be motivated in schemes with gaugino mediated Supersymmetry breaking [224, 225].

The smallness of λ allows us – at least to some extent – to treat the mixing between the MSSM sector and the singlets as a perturbation. The F-terms and soft terms of the Higgs bosons induce a term $\lambda\,\mu_{\text{eff}}\,v_{\text{EW}}^2\,s$ in the Lagrangian, where we have introduced $\mu_{\text{eff}} = \mu - v_d\,v_u A_\lambda/v_{\text{EW}}^2$. This linear term in s implies that s itself receives a vacuum expectation value $x = \langle s \rangle$ by the breaking of the electroweak symmetry. With the singlet mass terms $m_{\text{singlet}} \sim 10\,\text{GeV}$ one finds

$$x \sim \lambda\,\frac{v_{\text{EW}}^2}{m_{\text{singlet}}^2}\,\mu_{\text{eff}} \sim v_{\text{EW}}\ . \tag{5.13}$$

The smallness of λ is compensated by the suppressed singlet masses, such that we typically obtain a weak scale singlet VEV. The latter also induces new singlet mass terms such as $\kappa^2 x^2\,s^2$ and $\kappa A_\kappa x\,s^2$. In order to keep the singlet sector light, we assume that the self-coupling κ is not too large, $\kappa \lesssim 0.1$, and that the trilinear coupling $A_\kappa \lesssim m_{\text{singlet}}$. Note that the singlet also induces a shift of the electroweak minimum in the H_u and H_d direction compared to the MSSM. This effect is, however, negligibly small.

Let us now take a closer look at the Higgs sector of the model. We decompose the complex scalar s into a CP even state h_s and a CP odd state a_s. As interactions between MSSM fields and singlets are suppressed, it is reasonable to start our discussion for the CP even states in the basis (H, h, h_s), i.e. the basis of the MSSM Higgs bosons extended by the singlet. We impose the MSSM decoupling limit where h shares the properties of the Standard Model Higgs, while H becomes heavy. This implies that we can neglect the mixing between h_s and H in the following discussion.[4] Keeping only h and h_s the scalar mass matrix reads

$$\boldsymbol{m}_H^2 = \begin{pmatrix} m_h^2 & m_{hh_s}^2 \\ m_{hh_s}^2 & m_{h_s}^2 \end{pmatrix} \tag{5.14}$$

with

$$m_{h_s}^2 \simeq \kappa\,x\,(A_\kappa + 4\kappa x + 3\mu_s) - \lambda\,\frac{\mu_{\text{eff}}}{x}\,v_{\text{EW}}^2\ , \tag{5.15a}$$

$$m_{hh_s}^2 \simeq 2\lambda\,v_{\text{EW}}\,\mu_{\text{eff}}\ , \tag{5.15b}$$

---

[4]Note that a very large A_λ could increase the mixing between singlet and heavy MSSM Higgs. In this regime our analytic formulas would have to be modified.

Here, we have already used the minimization conditions of the Higgs potential in order to eliminate the soft masses. Note that with the assumptions introduced previously we expect $m_{hh_s} \sim m_{\text{singlet}} \sim 10\,\text{GeV}$. The mixing is strongly suppressed as the off-diagonal entry of the mass matrix is much smaller than the MSSM Higgs mass. The light physical mass eigenstate is dominantly h_s with a tiny admixture from h. We define

$$h_1 = \cos\theta\, h_s - \sin\theta\, h \,, \tag{5.16}$$

where we can approximate the mixing angle as

$$\cos\theta \simeq 1 \,, \tag{5.17}$$

$$\sin\theta \simeq \frac{m_{hh_s}^2}{m_h^2} \,. \tag{5.18}$$

The heavier state h_2 essentially coincides with the MSSM Higgs h. The mass of h_1 can be written as

$$m_{h_1}^2 \simeq m_{h_s}^2 - \frac{m_{hh_s}^4}{m_h^2} \,. \tag{5.19}$$

While the mixing in the CP even sector is small, it turns out to be highly relevant in the context of direct dark matter detection. The light scalar h_1 couples to nuclei only by its small MSSM Higgs component. In the CP odd sector the mixing between a_s and the MSSM pseudoscalar a is even stronger suppressed in the decoupling limit. Further, pseudoscalars only mediate spin-dependent interactions with nuclei. As discussed in section 3.3.4, these are excluded as the source of the observed direct detection signals. We therefore neglect the mixing between CP odd states and take the lightest pseudoscalar to be a pure singlet. Using again the minimization conditions, its mass can be expressed as

$$m_{a_s}^2 \simeq -2B\mu_s - x\,\kappa\,(3A_\kappa + \mu_s) - \lambda\,\frac{\mu_{\text{eff}}}{x}\,v_{\text{EW}}^2 \,. \tag{5.20}$$

For similar reasons we also neglect the mixing between the singlet fermion and the MSSM neutralinos. The singlino mass reads

$$m_{\widetilde{s}} = \mu_s + 2\kappa\,x \,. \tag{5.21}$$

The singlino is the LSP and thus stable in our model.[5]

The couplings in the singlet sector are all controlled by κ. The trilinear interaction terms follow from (5.5) and (5.8). They read

$$\mathscr{L} \supset -\frac{1}{2}\,g_{h_1\widetilde{s}\widetilde{s}}\,h_1\,\overline{\widetilde{s}}\,\widetilde{s} - \frac{1}{2}\,g_{a_s\widetilde{s}\widetilde{s}}\,a_s\,\overline{\widetilde{s}}\gamma_5\widetilde{s} - \frac{1}{6}\,g_{h_1h_1h_1}\,h_1{}^3 - \frac{1}{2}\,g_{h_1a_sa_s}\,h_1\,a_s^2 \tag{5.22}$$

---

[5]We reject the case where the bino is lighter than the singlino.

with

$$g_{h_1 \widetilde{s}\widetilde{s}} \simeq \sqrt{2}\kappa \, , \tag{5.23a}$$

$$g_{a_s \widetilde{s}\widetilde{s}} \simeq -\mathrm{i}\,\sqrt{2}\,\kappa \, , \tag{5.23b}$$

$$g_{h_1 h_1 h_1} \simeq \sqrt{2}\kappa \, (3\,m_{\widetilde{s}} + A_\kappa) \, , \tag{5.23c}$$

$$g_{h_1 a_s a_s} \simeq \sqrt{2}\kappa \, (m_{\widetilde{s}} - A_\kappa) \, . \tag{5.23d}$$

The coupling of h_1 to quarks and leptons is the Standard Model Higgs coupling suppressed by a factor of $\sin\theta$.

In summary, the described model includes light singlet states – a fermion, a scalar and a pseudoscalar – which only weakly interact with the MSSM sector. Given that the MSSM decoupling limit holds, the light scalar couples to ordinary matter like the Standard Model Higgs with a universal suppression factor $\sin\theta$. The singlet fermion, the singlino, is the lightest superpartner and hence stable. As we shall see in section 5.3, its interactions with the light scalar h_1 can lead to a coherent picture of singlino dark matter in which the direct detection signals find an explanation. Before we discuss this in detail we turn to the experimental constraints on the model.

5.2.2 Experimental Constraints

Strong constraints on the presented model arise from searches for Higgs-like particles by LEP. In a collider experiment, the scalar h_1 acts as a light Standard Model Higgs with reduced coupling. Therefore, the limits on the cross section for the process $e^+e^- \to Z+h$ can directly be translated into constraints on $\sin\theta$. The most relevant data set was presented by the L3 collaboration.[6]

If $m_{h_1} \lesssim 10\,\mathrm{GeV}$ it may further be produced in meson decays. Specifically it could mediate the radiative decay of upsilon mesons $\Upsilon \to \gamma + \ell^+\ell^-$, where the lepton pair $\ell^+\ell^-$ stems from an intermediate h_1 (see left panel of figure 5.2). Currently, the corresponding limits are not competitive compared to those from LEP (see e.g. [226]).

This situation changes if m_{h_1} is below the B meson threshold. Then it could enhance certain inclusive and exclusive decay modes of B mesons. Most interesting is the inclusive process $B \to h_1 + X_s$ followed by the decay $h_1 \to \mu^+\mu^-$ (see right panel of figure 5.2). The branching ratio for the first subprocess can be taken from [227],

$$\mathrm{Br}(B \to h_1 + X_s) = 0.058 \left(\frac{\sin\theta}{0.1}\right)^2 \left(1 - \frac{m_{h_1}^2}{m_b^2}\right)^2 \, , \tag{5.24}$$

the branching ratio for $\mathrm{Br}(h_1 \to \mu^+\mu^-)$ is equal to that of a Standard Model Higgs with mass m_{h_1}, it can e.g. be extracted from [226]. If one compares the measurement

---

[6]Note that the branching ratios of h_1 would be affected if $2m_{a_s} < m_{h_1}$. In this case the constraints on h_1 are altered.
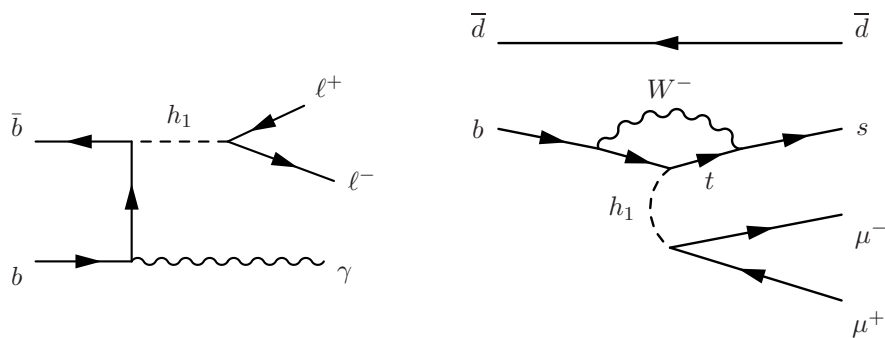
Figure 5.2: Meson decays mediated by the light scalar h_1: radiative Υ decay (left), inclusive B decay (right).

of the inclusive B decay by Belle [228] and the calculation of the Standard Model background [229, 230] for this process one finds an upper limit

$$\mathrm{Br}(B \to h_1 + X_s) \times \mathrm{Br}(h_1 \to \mu^+\mu^-) < 2.5 \times 10^{-6} \ . \tag{5.25}$$

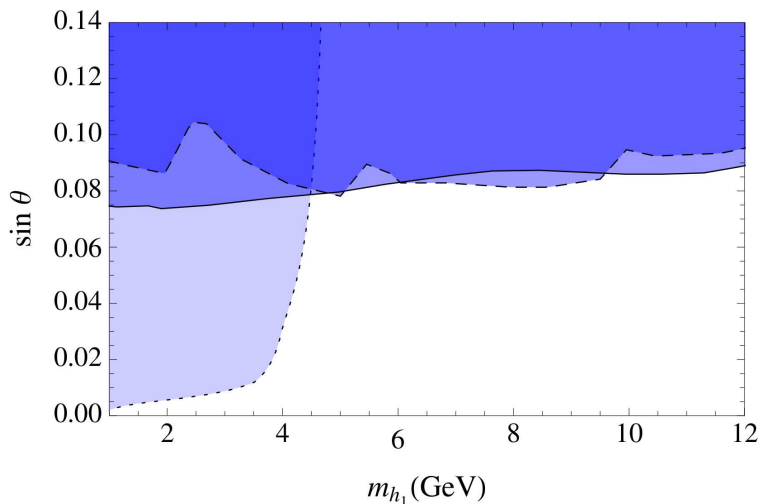The corresponding constraints on $\sin\theta$ together with those from LEP are depicted in figure 5.3.

Figure 5.3: Limits on $\sin\theta$ from LEP (solid line for neutrino channel, dashed line for all channels). The neutrino channel refers to the case where the final state Z boson decays into neutrinos. The limits from B decays are also shown (dotted line). The shaded region is excluded.

In the considered model, the heavier Standard Model-like Higgs h_2 would correspond to the new boson, recently observed by ATLAS and CMS at a mass of 126 GeV [209, 210]. As the coupling λ between singlet and MSSM sector is suppressed, the decay fraction of h_2 into singlets is negligibly small. This implies that the decay rates of h_2 do virtually not

differ from those of the Standard Model Higgs and it will be very difficult do distinguish the two.

The detection prospects of the singlino at the LHC depend strongly on the mass spectrum of the other superpartners. Very promising are signatures with many leptons and reduced transverse missing energy which arise from the cascade decays of heavier neutralinos or charginos into the singlino [231, 232].

5.3 Singlinos as Dark Matter

In this section we want to determine whether singlinos can play the role of thermal WIMPs. We will therefore consider the main annihilation channels of singlinos and calculate their thermal relic density. Then, we will study singlino interactions with nuclei in order to figure out whether singlinos can be responsible for the direct detection anomalies observed by DAMA, CoGeNT and CRESST.

5.3.1 The Relic Density

Singlinos are only very weakly coupled to the fields of the MSSM. Therefore, the annihilation rate into MSSM particles is so low that it would lead to a singlino abundance strongly in excess of the dark matter abundance. On the other hand, interactions within the singlet sector can be quite sizable. If the singlet scalars or pseudoscalars are lighter than the singlinos they may appear as final states in the annihilation process (see figure 5.4 for the Feynman diagrams).
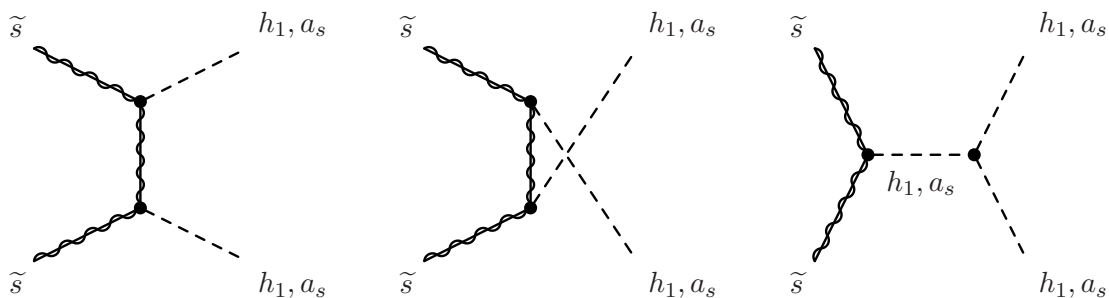

Figure 5.4: Singlino annihilation into (pseudo)scalars.

Due to the CP properties of the initial and final states it turns out that the annihilation into either a pair of scalars or a pair of pseudoscalars is velocity suppressed (p-wave). Only the diagrams with one scalar and one pseudoscalar in the final state give rise to s-wave annihilation. If kinematically accessible they dominate over the p-wave processes. We therefore distinguish three different cases for which we separately calculate the anni-

hilation cross section to leading order in a velocity expansion.[7] In the following formulas we have set the scalar masses to zero. The full expressions can be found in appendix B.

Case 1: Only $\widetilde{s}\,\widetilde{s} \rightarrow h_1\,h_1$ kinematically accessible,

$$\sigma\,v_{\rm rel} \simeq \frac{g_{h_1\widetilde{s}\widetilde{s}}^2}{128\,\pi\,m_{\widetilde{s}}^2}\left(3\,g_{h_1\widetilde{s}\widetilde{s}}^2 - \frac{5}{6}\,g_{h_1\widetilde{s}\widetilde{s}}\frac{g_{h_1h_1h_1}}{m_{\widetilde{s}}} + \frac{1}{16}\frac{g_{h_1h_1h_1}^2}{m_{\widetilde{s}}^2}\right)\,v_{\rm rel}^2\; + \mathcal{O}(v_{\rm rel}^4)\,. \qquad (5.26)$$

Case 2: Only $\widetilde{s}\,\widetilde{s} \rightarrow a_s\,a_s$ kinematically accessible,

$$\sigma\,v_{\rm rel} \simeq \frac{g_{h_1\widetilde{s}\widetilde{s}}^2}{128\,\pi\,m_{\widetilde{s}}^2}\left(\frac{1}{3}\,g_{h_1\widetilde{s}\widetilde{s}}^2 + \frac{1}{6}\,g_{h_1\widetilde{s}\widetilde{s}}\frac{g_{h_1a_sa_s}}{m_{\widetilde{s}}} + \frac{1}{16}\frac{g_{h_1a_sa_s}^2}{m_{\widetilde{s}}^2}\right)\,v_{\rm rel}^2\; + \mathcal{O}(v_{\rm rel}^4)\,. \qquad (5.27)$$

Case 3: $\widetilde{s}\,\widetilde{s} \rightarrow h_1\,a_s$ kinematically accessible,

$$\sigma\,v_{\rm rel} \simeq \frac{g_{h_1\widetilde{s}\widetilde{s}}^2}{16\,\pi\,m_{\widetilde{s}}^2}\left(g_{h_1\widetilde{s}\widetilde{s}} - \frac{g_{h_1a_sa_s}}{4\,m_{\widetilde{s}}}\right)^2 + \mathcal{O}(v_{\rm rel}^2)\,. \qquad (5.28)$$

The couplings $g_{h_1\widetilde{s}\widetilde{s}}$, $g_{h_1h_1h_1}$ and $g_{h_1a_sa_s}$ were defined in (5.23). We can now compare the annihilation cross sections from above with the thermal ones shown in figure 2.6. For a singlino mass $m_{\widetilde{s}} \simeq 5 - 10\,\mathrm{GeV}$ either a s-wave cross section $\sigma_{\rm s\text{-}wave} \simeq 2.4 \times 10^{-26}\,\mathrm{cm^3\,s^{-1}}$ or a p-wave cross section of $\sigma_{\rm p\text{-}wave} \simeq 1.6 \times 10^{-25}\,\mathrm{cm^3\,s^{-1}}$ is required to obtain a singlino density matching the dark matter density. This implies a singlet coupling $\kappa \sim 0.1$ in case 1 or 2 and $\kappa \sim 0.02$ in case 3. Thus we have proven that thermal singlino dark matter is perfectly viable within the singlet-extended MSSM.

5.3.2 Direct Detection

We will now show that singlinos may have an interaction strength with nucleons in the regime favored by the direct detection experiments DAMA, CoGeNT and CRESST. The cross section of singlinos with nucleons is dominated by the exchange of the light scalar h_1. The Feynman diagram is depicted in figure 5.5.

Indeed, this process is suppressed by the mixing angle $\sin\theta$. However, the correspondingly small coupling of h_1 to nucleons is overcompensated by the smallness of m_{h_1} which enters the cross section to the forth power. Exchange of heavier particles like Z or h_2 is relatively suppressed, while exchange of a_s can be neglected due to its spin-dependent nature.

The singlino proton cross section for the h_1 exchange diagram can be approximated by

$$\sigma_p \simeq \frac{4\,m_{\widetilde{s}}^2\,m_p^2}{\pi\,(m_{\widetilde{s}} + m_p)^2}\,f_p^2 \simeq \frac{4\,m_p^2}{\pi}\,f_p^2\,. \qquad (5.29)$$

---

[7]Note that the velocity expansion is a valid approximation unless in the case of a resonance.
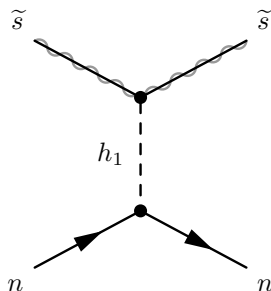
Figure 5.5: Singlino nucleon elastic scattering.

Here m_p denotes the proton mass and f_p the effective singlino proton coupling which can be expressed as

$$f_p = m_p f_q \left(f_u^p + f_d^p + f_s^p + \frac{6}{27} f_G^p \right) , \qquad (5.30)$$

where f_q is the singlino quark coupling divided by the quark mass. Note that f_q is universal in our model as the scalar h_1 couples to quarks in the same way as the Standard Model Higgs – up to the suppression factor $\sin\theta$. By evaluating the Feynman diagram in figure 5.5 one finds

$$f_q = g_{h_1 \widetilde{s}\widetilde{s}} \frac{\sin\theta}{\sqrt{2}\, v_{\text{EW}}} \frac{1}{m_{h_1}^2} . \qquad (5.31)$$

The coefficients f_u^p, f_d^p, f_s^p and f_G^p specify the up, down, strange quark and gluon contribution to the proton mass. They can in principle be determined in scattering experiments involving pions and nucleons. If we use the cross sections from [233], we find $f_u^p \simeq 0.03$, $f_d^p \simeq 0.04$, $f_s^p \simeq 0.38$ and $f_G^p \simeq 0.55$. Unfortunately, there exist large uncertainties on these quantities which translate into an $\mathcal{O}(1)$ uncertainty in our determination of the singlino proton cross section. Numerically we find

$$\sigma_p \simeq 10^{-40}\,\text{cm}^2 \left(\frac{\kappa}{0.08} \right)^2 \left(\frac{\sin\theta}{0.03} \right)^2 \left(\frac{4\,\text{GeV}}{m_{h_1}} \right)^4 . \qquad (5.32)$$

As singlinos mainly scatter off the strange quarks and gluons in the nucleon, the singlino proton and singlino neutron cross sections are virtually identical, i.e. $f_n = f_p$. Given this, a cross section of $\sigma_p \sim 10^{-40}$ cm^2 is required to explain the DAMA, CoGeNT and CRESST signals. The above formula suggests that such a large cross section can indeed be realized in the singlet-extended MSSM if m_{h_1} is slightly below 10 GeV. To arrive simultaneously at a consistent picture with singlinos as thermal dark matter, one must, however, require that only the annihilation channel $\widetilde{s}\widetilde{s} \to h_1 h_1$ is kinematically accessible (case 1 in section 5.3.1). Otherwise the value of κ required for a thermal cross section would be too small to obtain a large enough singlino proton cross section.

Let us finally emphasize that in the discussed scheme, singlinos are standard WIMPs which have spin-independent isospin conserving interactions with nuclei. Therefore, the tension of the direct detection signals with the experiments XENON, CDMS and SIMPLE cannot be resolved by means of particle physics.

5.3.3 Indirect Detection

Indirect searches strongly constrain the annihilation of dark matter in the galactic halo and in the sun. The corresponding limits which were derived in chapter 4 depend on whether the annihilation is s- or p-wave and on the annihilation channel. The scheme with thermal singlino dark matter in which the direct detection signals find an explanation requires a singlino mass $m_{\widetilde{s}} \simeq 5 - 10 \, \text{GeV}$. Further, the dominant annihilation channel should be $\widetilde{s}\,\widetilde{s} \rightarrow h_1 \, h_1$. Antiproton searches are insensitive to this particular process as it is velocity suppressed. Relevant constraints, however, arise from neutrino telescopes. If $m_{h_1} \simeq 3.5 - 10 \, \text{GeV}$ the light scalar would subsequently decay into tau and charm pairs with very similar branching fractions while other channels can be neglected. The limits on such p-wave annihilations are related to the tau channel limit in the upper right panel of figure 4.3 rescaled by the appropriate branching fraction.[8] However, the energy shift due to the larger number of final state taus has to be considered. Taking this into account we find

$$\sigma_p \leq 2 \times 10^{-40} \, \text{cm}^2 \tag{5.33}$$

for $m_{\widetilde{s}} = 5 - 10 \text{GeV}$. This implies that our setup is not excluded by indirect searches, but it could probably be tested with the next generation neutrino telescopes. A loop-hole is the case $m_{h_1} < 2 \, m_\tau$ where neutrino signals are suppressed. But notice that a very small m_{h_1} requires considerable fine-tuning as the naive expectation is $m_{h_1} \sim m_{\text{singlet}} \sim 10 \text{GeV}$. Further, meson decays are particularly sensitive to very light h_1.

Up to now we have assumed that the p-wave process $\widetilde{s}\,\widetilde{s} \rightarrow h_1 \, h_1$ still dominates the WIMP annihilation in the sun. But even with the singlino freeze-out being p-wave, there could arise a situation where a suppressed s-wave process overcomes the p-wave process for the low particle velocities in the sun. Singlinos may e.g. perform s-wave annihilation into Standard Model fermions through an intermediate pseudoscalar. The corresponding cross section is strongly suppressed by the very small mixing between MSSM and singlet pseudoscalars, but in some region of parameter space it becomes dominant in the sun. In this case our considerations from above do not hold. The final states would mainly be bottom quarks, but taus would also contribute with a branching fraction ~ 0.1. If the s-wave annihilation in the sun was strong enough to enforce equilibrium with capture,

---

[8]We can neglect the charm final states as they do not considerably contribute to the neutrino flux compared to the tau final states

the limits from the upper left panel of figure 4.3 would hold – up to corrections close to the evaporation mass. This implies that cross sections up to $\sigma_p \simeq 10^{-40}$ cm^2 could be probed. But if the s-wave process was weaker, one would need to include an additional suppression factor.

Let us finally mention that the annihilation channel $\widetilde{s}\,\widetilde{s} \rightarrow a_s\, h_1$ if kinematically accessible would induce an antiproton flux already in some tension with observation (see figure 4.7). But a consistent picture with thermal singlino dark matter as the source of the direct detection signals, anyway, only arises if this channel is kinematically forbidden.

5.3.4 A Benchmark Scenario

Let us briefly summarize the phenomenology of the model we introduced. We made the assumptions of a singlet mass scale $m_{\text{singlet}} \sim 10$ GeV and of a suppressed coupling between MSSM and singlet sector, but allowed for sizable interactions among the singlets. This setup leads to singlino LSPs as viable dark matter candidates. To illustrate this, we have chosen a set of benchmark parameters according to our assumptions (left column in table 5.2). The corresponding singlet mass spectrum, the mixing angle of the singlet scalar with the light MSSM Higgs, the relic singlino density and the singlino proton cross section are shown in the right column of table 5.2.

(a) Input parameters.		(b) Predictions.	
Quantity	Value	Quantity	Value
μ_{eff}	370 GeV	m_{a_s}	29 GeV
x	169 GeV	$m_{\widetilde{s}}$	8.0 GeV
A_κ	-10 GeV	m_{h_1}	4.0 GeV
μ_s	-19 GeV	$\sin\theta$	0.024
$B\mu_s$	0	σ_p	6×10^{-41} cm^2
λ	-0.003	$\Omega\, h^2$	0.1
κ	0.08		

Table 5.2: Parameters of a phenomenologically viable benchmark point. We assume $m_h = 126$ GeV.

In the benchmark scenario, singlino annihilation is dominated by the p-wave process $\widetilde{s}\,\widetilde{s} \rightarrow h_1\, h_1$, final states which include the singlet pseudoscalar are kinematically forbidden. The cross section is determined by (B.1), we find $\sigma_{\text{p-wave}} = 1.6 \times 10^{-25}$ cm^3 s^{-1}, i.e. the singlino density matches the dark matter density (c.f. figure 2.6). As the annihilation is velocity suppressed, the constraints from indirect detection are satisfied. At the same time, the singlino interactions with nuclei mediated by the light scalar h_1 are in the correct range to explain the signals of DAMA, CoGeNT and CRESST. The singlino proton cross section is inside the confidence region for the modulated CoGeNT signal, it is slightly above the region for the CoGeNT rate analysis and slightly below DAMA and

CRESST (see figure 3.5). It is further in tension with the CDMS and XENON searches. Therefore, as in any model which tries to explain the direct detection signals by WIMP scattering, one has to invoke experimental and/or astrophysical uncertainties in order to arrive at a consistent picture (see section 3.3.4). Let us finally note that the light scalar, due to its small mixing with the MSSM Higgs, is consistent with collider and flavor constraints (c.f. figure 5.3). There exist, however, good prospects to detect it in the near future e.g. via radiative Υ meson decays.

Chapter 6

Conclusion

In this work we have analyzed the possible signals for light dark matter which were obtained by the direct detection experiments DAMA, CoGeNT and CRESST. Under standard particle and astrophysics assumptions we found the corresponding confidence regions in the WIMP parameter space to be intriguingly close. This suggests a common origin of all three signals. Still, the favored regions are not fully compatible and further, the null searches XENON, CDMS and SIMPLE seem to exclude the dark matter interpretation. We considered possibilities to resolve the experimental tension in terms of astrophysical and experimental uncertainties or WIMPs with non-standard couplings. However, we had to conclude that the question whether a consistent explanation of the direct detection data in terms of light WIMPs arises can currently not be answered conclusively. The situation is expected to improve in the near future. Ongoing runs of the CoGeNT and CRESST experiments with reduced background levels will hopefully clarify the dark matter interpretation of their nuclear recoil spectra in the near future. Additionally, a dedicated measurement of the electron yield at XENON below energies of $3\,\mathrm{keV}$ could reliably establish the sensitivity of the XENON experiment for light dark matter.

Turning to indirect dark matter detection we did not find indications for WIMP annihilations in the sun or the galactic halo in the data of the neutrino telescope Super-Kamiokande and the antiproton search BESS-Polar II. The absence of a signal was used to derive stringent constraints on the cross sections especially of light WIMPs. These suggest that thermal WIMPs may only account for the direct detection anomalies if their annihilation is either velocity suppressed or proceeds dominantly into electron or muon final states. We note that neutrino telescopes are especially suitable to search for WIMPs with velocity suppressed annihilation in the future. The expected signals are only mildly suppressed compared to the s-wave case and may already be in reach for upcoming detectors like Hyper-Kamiokande [234]. Any other indirect detection technique suffers from the low velocity of WIMPs in the galaxy and is, therefore, hardly sensitive to

p-wave annihilation.

Finally, we considered a theoretical model, in which light WIMPs can be accounted for. The latter is based on the concept of Supersymmetry but its particle content is augmented, compared to the MSSM, by an additional singlet superfield. A very interesting phenomenology arises in the regime where singlet and MSSM sector are only weakly coupled. A generic prediction is the presence of a light scalar which would in some sense act as a light Standard Model Higgs with universally suppressed couplings. It is accompanied by the singlino whose interactions with nuclei, mediated by the light scalar, are sizable enough to explain the direct detection signals. Annihilations within the singlet sector further ensure that relic singlinos may indeed constitute the dark matter. It is proven that the model is consistent with experimental constraints and the above-mentioned limits from indirect dark matter searches.

The prospects to soon test the presented model are very promising. B factories offer the possibility to search for the light scalar in meson decays. Moreover, singlinos give rise to very distinct event signatures at the LHC which often include many leptons and reduced missing transverse energy. Finally, the neutrinos induced by singlino annihilation in the sun can be detected at future neutrino telescopes.

Appendix A

Solving the Diffusion Equation

A.1 Secondary Antiprotons

The diffusion equation can be solved semi-analytically within the two-zone diffusion model. The method was described in [159, 178] and shall be reviewed here. One uses cylinder coordinates and Bessel expands the space-energy density and the source terms to get rid of the dependence on the radial distance $\mathbf{r}$:

$$N_{\bar{p}}(\mathbf{r}, T) = \sum_{i=1}^{\infty} N_{\bar{p},i}(T) \, J_0\left(\zeta_i \frac{\mathbf{r}}{R}\right) \;, \quad q_{\bar{p}}(\mathbf{r}, T) = \sum_{i=1}^{\infty} q_{\bar{p},i}(T) \, J_0\left(\zeta_i \frac{\mathbf{r}}{R}\right) \;. \tag{A.1}$$

Here $R \simeq 20$ kpc denotes the radius of the galactic disc and ζ_i the i-th zero of the Bessel function J_0. The expansion automatically satisfies the boundary condition that $N_{\bar{p}} = q_{\bar{p}} = 0$ at $\mathbf{r} = R$. The Bessel coefficients for the secondary source term read

$$q_{\bar{p},i}^{\text{sec}}(T) = \frac{2}{J_1^2(\zeta_i) \, R^2} \int_0^R \mathrm{d}\mathbf{r} \, \mathbf{r} \, q_{\bar{p}}^{\text{sec}}(\mathbf{r}, T) \, J_0\left(\zeta_i \frac{\mathbf{r}}{R}\right) \;. \tag{A.2}$$

We assume a constant source term in the galactic disc, i.e. $q_{\bar{p}}^{\text{sec}}(\mathbf{r}, T) = q_{\bar{p}}^{\text{sec}}(T) \, \Theta(R - \mathbf{r})$, where Θ denotes the Heaviside function and $q_{\bar{p}}^{\text{sec}}(T)$ is given by (4.30).

In the next step, one plugs the Bessel expansions into the diffusion equation and performs the approximations described in section 4.2.2.1. The axial part of the diffusion equation can then be solved analytically and one arrives at a differential equation in energy which reads (at $z = 0$)

$$A_{\bar{p},i}(N_{\bar{p},i} - N_{\bar{p},i}^0) + 2h \, \partial_T(b_{\text{tot}} \, N_{\bar{p},i} - K_{EE} \, \partial_T N_{\bar{p},i}) = 2h q_{\bar{p},i}^{\text{ter}} \tag{A.3}$$

with

$$A_{\bar{p},i} = 2h\Gamma_{\text{ann}} + V_c + K S_i \coth\left(\frac{S_i L}{2}\right), \qquad S_i = \sqrt{\frac{V_c^2}{K^2} + 4\frac{\zeta_i^2}{R^2}} \tag{A.4}$$

and

$$N_{\bar{p},i}^0 = \frac{2\,h\,q_{\bar{p},i}^{\text{sec}}}{A_{\bar{p},i}}\;. \tag{A.5}$$

The last differential equation can only be solved numerically. At high antiproton energies $(T \gg 10\,\text{GeV})$ energy losses, reacceleration as well as tertiaries can be neglected and $N_{\bar{p},i}$ approaches $N_{\bar{p},i}^0$.

A.2 Primary Antiprotons

The diffusion equation for primary antiprotons can be solved in the same way as for secondaries. Within the two-zone diffusion model, this was first done in [182, 235]. The main difference compared to secondaries is that primary sources are not only located in the galactic disc but are distributed over the entire halo. Still, one arrives at the same differential equation (A.3), however, the Bessel coefficients are defined differently. On finds (see [182, 235])

$$N_{\bar{p},i}^0 = q_{\bar{p}}^{\text{prim}}(r_\odot, T)\,\mathcal{R}_i \tag{A.6}$$

with

$$\mathcal{R}_i = \frac{1}{\rho_0^2}\,\frac{2\int_0^L \mathrm{d}z'\,\exp\left(\frac{V_c(L-z')}{2K}\right)\sinh\left(\frac{S_i(L-z')}{2}\right)(\rho_\chi^2)_i}{A_{\bar{p},i}\sinh\left(\frac{S_iL}{2}\right)}\,\exp\left(\frac{-V_cL}{2K}\right)\;. \tag{A.7}$$

Here the $(\rho_\chi^2)_i$ are the Bessel coefficients for the dark matter density distribution which can be obtained analogous to the $q_{\bar{p},i}^{\text{sec}}$ in (A.2).

Again the differential equation in energy (A.3) has to be solved numerically. In the high energy limit $N_{\bar{p},i}$ approaches $N_{\bar{p},i}^0$ and the local antiproton space-energy density reads

$$N_{\bar{p}} \simeq q_{\bar{p}}^{\text{prim}}(r_\odot, T)\,\mathcal{R}_\odot\;, \qquad \mathcal{R}_\odot = \sum_{i=1}^{\infty} \mathcal{R}_i J_0\left(\zeta_i\frac{r_\odot}{R}\right)\;. \tag{A.8}$$

We use this approximation only to illustrate the impact of the propagation parameters in section 4.2.2.2. In the derivation of antiproton constraints on dark matter annihilations we always consider the full numerical solution to the diffusion equation.

Appendix B

Cross Sections for Singlino Annihilation

Here we state explicitly the singlino annihilation cross sections to leading order in a velocity expansion. We find:

Channel: $\widetilde{s}\,\widetilde{s} \to h_1\, h_1$

$$
\begin{aligned}
\sigma\, v_{\rm rel} =\ & \frac{g_{h_1\widetilde{s}\widetilde{s}}^2 \sqrt{m_{\widetilde{s}}^2 - m_{h_1}^2}}{128\,\pi}\, v_{\rm rel}^2 \\
& \times \left(\frac{16}{3}\, g_{h_1\widetilde{s}\widetilde{s}}^2\, \frac{m_{\widetilde{s}}\,(9\,m_{\widetilde{s}}^4 - 8\,m_{\widetilde{s}}^2\,m_{h_1}^2 + 2\,m_{h_1}^4)}{(2\,m_{\widetilde{s}}^2 - m_{h_1}^2)^4} \right. \\
& \quad - \frac{8}{3}\, g_{h_1\widetilde{s}\widetilde{s}}\, g_{h_1 h_1 h_1}\, \frac{(5\,m_{\widetilde{s}}^2 - 2\,m_{h_1}^2)}{(2\,m_{\widetilde{s}}^2 - m_{h_1}^2)^2\,(4\,m_{\widetilde{s}}^2 - m_{h_1}^2)} \\
& \quad \left. + g_{h_1 h_1 h_1}^2\, \frac{1}{m_{\widetilde{s}}\,(4\,m_{\widetilde{s}}^2 - m_{h_1}^2)^2} \right) \quad + \mathcal{O}(v_{\rm rel}^4)\ .
\end{aligned}
\tag{B.1}
$$

Channel: $\widetilde{s}\,\widetilde{s} \to a_s\, a_s$

$$
\begin{aligned}
\sigma\, v_{\rm rel} =\ & \frac{g_{h_1\widetilde{s}\widetilde{s}}^2 \sqrt{m_{\widetilde{s}}^2 - m_{a_s}^2}}{128\,\pi}\, v_{\rm rel}^2 \\
& \times \left(\frac{16}{3}\, g_{h_1\widetilde{s}\widetilde{s}}^2\, \frac{m_{\widetilde{s}}\,(m_{\widetilde{s}}^2 - m_{a_s}^2)^2}{(2\,m_{\widetilde{s}}^2 - m_{a_s}^2)^4} \right. \\
& \quad + \frac{8}{3}\, g_{h_1\widetilde{s}\widetilde{s}}\, g_{h_1 a_s a_s}\, \frac{(m_{\widetilde{s}}^2 - m_{a_s}^2)}{(2\,m_{\widetilde{s}}^2 - m_{a_s}^2)^2\,(4\,m_{\widetilde{s}}^2 - m_{h_1}^2)} \\
& \quad \left. + g_{h_1 a_s a_s}^2\, \frac{1}{m_{\widetilde{s}}\,(4\,m_{\widetilde{s}}^2 - m_{h_1}^2)^2} \right) \quad + \mathcal{O}(v_{\rm rel}^4)\ .
\end{aligned}
\tag{B.2}
$$

Channel: $\widetilde{s}\,\widetilde{s} \rightarrow h_1\,a_s$

$$\sigma\,v_{\mathrm{rel}} \;=\; \frac{g_{h_1\widetilde{s}\widetilde{s}}^2\,m_{\widetilde{s}}\,\sqrt{m_{\widetilde{s}}^2 - m_{h_1}^2}}{4\,\pi}$$

$$\times \left(\frac{g_{h_1\widetilde{s}\widetilde{s}}}{2\,m_{\widetilde{s}}^2 - m_{h_1}^2} - \frac{g_{h_1 a_s a_s}}{2\,m_{\widetilde{s}}\,(4\,m_{\widetilde{s}}^2 - m_{h_1}^2)} \right)^2 \;+\; \mathcal{O}(v_{\mathrm{rel}}^2)\,. \tag{B.3}$$

For the process $\widetilde{s}\,\widetilde{s} \rightarrow h_1\,a_s$ we have set $m_{h_1} = m_{a_s}$ for simplicity.

Acknowledgments

I would like to thank Michael Ratz for the supervision of this thesis, for his strong support and for his advice. I am further grateful to him as well as to many people in Munich and beyond for the inspiring discussions about physics, in particular to Rolf Kappl, Kai Schmidt-Hoberg, Stefan Vogl, David Tran, Jean Lanfranchi, Cristoforo Simonetto, Andrzej Buras, Hans Peter Nilles, Sven Krippendorf and Koichi Hamaguchi.

I would also like to express my gratitude to the DFG cluster of excellence "Origin and Structure of the Universe", the SFB-Transregio 27 "Neutrinos and Beyond" by Deutsche Forschungsgemeinschaft and the DFG-Graduiertenkolleg "Particle Physics at the Energy Frontier of New Phenomena" for providing the optimal funding for my research and for giving me the opportunity to visit conferences and summer schools all over the world.

For creating a very pleasant and relaxed atmosphere at the department, I would like to thank my present and former colleagues of T30e, T30d and T31, especially Rolf Kappl, Björn Petersen, Roland Schieren, Kai Schmidt-Hoberg, David Tran, Cristoforo Simonetto, Christian Staudt, Maximilian Fallbacher and Stefan Vogl.

I am indebted to Christian Staudt, Maximilian Fallbacher, Stefan Vogl, Rolf Kappl and Björn Petersen for proofreading this manuscript, and to Jesús Torrado Cacho for his assistance in handling the IDL Astronomy User's Library. Then, my thanks go to Karin Ramm for all the help in organization and bureaucracy.

Last but not least, I am deeply grateful to Ulrike, to my family and to all the people who enriched my private life throughout the last years.

Bibliography

[1] J.H. Oort, Bulletin of the Astron. Inst. of the Netherlands **6** (1932), 249.

[2] D.A. Dicus, E.W. Kolb and V.L. Teplitz, Phys. Rev. Lett. **39** (1977), 168.

[3] P. Hut, Phys. Lett. **B69** (1977), 85.

[4] B.W. Lee and S. Weinberg, Phys. Rev. Lett. **39** (1977), 165.

[5] S. Dimopoulos and H. Georgi, Nucl. Phys. **B193** (1981), 150.

[6] G.R. Farrar and P. Fayet, Phys. Lett. **B76** (1978), 575.

[7] R. Bernabei et al., Eur. Phys. J. **C56** (2008), 333.

[8] R. Bernabei et al., Eur. Phys. J. **C67** (2010), 39.

[9] C.E. Aalseth et al., Phys. Rev. Lett. **106** (2011), 131301.

[10] C. Aalseth et al., Phys. Rev. Lett. **107** (2011), 141301.

[11] G. Angloher et al., Eur. Phys. J. **C72** (2012), 1971.

[12] E. Aprile et al., Phys. Rev. Lett. **107** (2011), 131302.

[13] J. Angle et al., Phys. Rev. Lett. **107** (2011), 051301.

[14] Z. Ahmed et al., Science **327** (2010), 1619.

[15] Z. Ahmed et al., Phys. Rev. Lett. **106** (2011), 131302.

[16] M. Felizardo et al., Phys. Rev. Lett. **105** (2010), 211301.

[17] M. Felizardo et al., Phys. Rev. Lett. **108** (2012), 201302.

[18] J. Collar, Talk at TAUP 2011, Munich, September 5-9 (2011).

[19] S. Chang et al., JCAP **1008** (2010), 018.

[20] J.L. Feng et al., Phys. Lett. **B703** (2011), 124.

[21] W.H. Press and D.N. Spergel, Astrophys. J. **296** (1985), 679.

[22] S. Desai et al., Phys. Rev. **D70** (2004), 083523.

[23] R. Abbasi et al., Phys. Rev. Lett. **102** (2009), 201302.

[24] J. Silk, K.A. Olive and M. Srednicki, Phys. Rev. Lett. **55** (1985), 257.

[25] K. Griest and D. Seckel, Nucl. Phys. **B283** (1987), 681.

[26] A. Gould, Astrophys. J. **321** (1987), 560.

[27] J. Silk and M. Srednicki, Phys. Rev. Lett. **53** (1984), 624.

[28] M. Fradkin and Z. Eksperim, Teor. Fiz. **29** (1955), 147.

[29] A. Bottino et al., Phys. Rev. **D72** (2005), 083518.

[30] F. Donato et al., Phys. Rev. Lett. **102** (2009), 071301.

[31] K. Abe et al., Phys. Rev. Lett. **108** (2012), 051102.

[32] A. Putze, L. Derome and D. Maurin, Astron. Astrophys. **516** (2010), A66.

[33] R. Duperray et al., Phys. Rev. **D71** (2005), 083013.

[34] H.K. Dreiner et al., Eur. Phys. J. **C62** (2009), 547.

[35] A.V. Belikov et al., Phys. Lett. **B705** (2011), 82.

[36] A.H. Guth, Phys. Rev. **D23** (1981), 347.

[37] F. Zwicky, Helv. Phys. Acta **6** (1933), 110.

[38] V.C. Rubin, N. Thonnard and J. Ford, W. K., Astrophys. J. **238** (1980), 471.

[39] T. van Albada et al., Astrophys. J. **295** (1985), 305.

[40] M. Milgrom, Astrophys. J. **270** (1983), 365.

[41] D. Clowe, A. Gonzalez and M. Markevitch, Astrophys. J. **604** (2004), 596.

[42] D. Clowe et al., Astrophys. J. **648** (2006), L109.

[43] D.S. Graff and K. Freese, Astrophys. J. **456** (1996), L49.

[44] C. Alcock et al., Astrophys. J. **542** (2000), 281.

[45] P. Tisserand et al., Astron. Astrophys. **469** (2007), 387.

[46] V.F. Mukhanov and G. Chibisov, JETP Lett. **33** (1981), 532.

[47] J. Silk, Astrophys. J. **151** (1968), 459.

[48] R. Sachs and A. Wolfe, Astrophys. J. **147** (1967), 73.

[49] G.F. Smoot et al., Astrophys. J. **396** (1992), L1.

[50] C. Bennett et al., Astrophys. J. Suppl. **148** (2003), 1.

[51] C. Reichardt et al., Astrophys. J. **694** (2009), 1200.

[52] M. Brown et al., Astrophys. J. **705** (2009), 978.

[53] N. Jarosik et al., Astrophys. J. Suppl. **192** (2011), 14.

[54] W.J. Percival et al., Mon. Not. Roy. Astron. Soc. **401** (2010), 2148.

[55] A.G. Riess et al., Astrophys. J. **699** (2009), 539.

[56] A.G. Riess et al., Astron. J. **116** (1998), 1009.

[57] S. Perlmutter et al., Astrophys. J. **517** (1999), 565.

[58] E. Komatsu et al., Astrophys. J. Suppl. **192** (2011), 18.

[59] B. Fields and S. Sarkar, J. Phys. G **G33** (2006), 1.

[60] M. Laine and Y. Schroder, Phys.Rev. **D73** (2006), 085009.

[61] M. Drees, M. Kakizaki and S. Kulkarni, Phys. Rev. **D80** (2009), 043505.

[62] G. Steigman, B. Dasgupta and J.F. Beacom, arXiv:1204.3622 [hep-ph] (2012).

[63] E.W. Kolb and M.S. Turner, The Early Universe, Westview Press (1990).

[64] J. Jeans, Phil. Trans. R. Soc. Lond. A **199** (1902), 1.

[65] D. Lynden-Bell, Mon. Not. Roy. Astron. Soc. **136** (1967), 101.

[66] V. Springel et al., Nature **435** (2005), 629.

[67] V. Springel et al., Mon. Not. Roy. Astron. Soc. **391** (2008), 1685.

[68] J. Diemand et al., Nature **454** (2008), 735.

[69] J.F. Navarro, C.S. Frenk and S.D. White, Astrophys. J. **462** (1996), 563.

[70] A.W. Graham et al., Astron. J. **132** (2006), 2685.

[71] M. Cirelli et al., JCAP **1103** (2011), 051.

[72] R. Catena and P. Ullio, JCAP **1008** (2010), 004.

[73] P. Salucci et al., Astron. Astrophys. **523** (2010), A83.

[74] A.S. Eddington, Mon. Not. Roy. Astron. Soc. **76** (1916), 572.

[75] W. Dehnen and J. Binney, Mon. Not. Roy. Astron. Soc. **298** (1998), 387.

[76] M.C. Smith et al., Mon. Not. Roy. Astron. Soc. **379** (2007), 755.

[77] M. Vogelsberger et al., Mon. Not. Roy. Astron. Soc. **395** (2009), 797.

[78] K. Schmidt-Hoberg and M.W. Winkler, JCAP **0909** (2009), 010.

[79] E. Aprile and L. Baudis, Particle Dark Matter, Cambridge University Press (2010).

[80] G. Gerbier and J. Gascon, Particle Dark Matter, Cambridge University Press (2010).

[81] J. Lewin and P. Smith, Astropart.Phys. **6** (1996), 87.

[82] G. Gelmini and P. Gondolo, Phys.Rev. **D64** (2001), 023504.

[83] J. Binney and S. Tremaine, Galactic Dynamics, Princeton University Press (2008).

[84] D.R. Tovey et al., Phys. Lett. **B488** (2000), 17.

[85] H. De Vries, C.W. De Jager and C. De Vries, Atom. Data Nucl. Data Tabl. **36** (1987), 495.

[86] G. Fricke et al., Atomic Data and Nuclear Data Table **60** (1995), 177.

[87] G. Duda, A. Kemper and P. Gondolo, JCAP **0704** (2007), 012.

[88] M.T. Ressell and D.J. Dean, Phys. Rev. **C56** (1997), 535.

[89] R. Bernabei et al., Phys. Lett. **B389** (1996), 757.

[90] R. Bernabei et al., Nucl.Instrum.Meth. **A592** (2008), 297.

[91] R. Bernabei et al., arXiv:1007.0595 [astro-ph.CO] (2010).

[92] Z. Ahmed et al., arXiv:1203.1309 [astro-ph.CO] (2012).

[93] D. Barker and D.M. Mei, arXiv:1203.4620 [astro-ph.IM] (2012).

[94] C. Aalseth et al., Phys. Rev. Lett. **101** (2008), 251301.

[95] C. Kelso, D. Hooper and M.R. Buckley, Phys.Rev. **D85** (2012), 043515.

[96] M.T. Frandsen et al., JCAP **1201** (2012), 024.

[97] J. Angle et al., Phys. Rev. Lett. **100** (2008), 021303.

[98] A. Manzur et al., Phys.Rev. **C81** (2010), 025808.

[99] G. Plante et al., Phys.Rev. **C84** (2011), 045805.

[100] J.I. Collar and D.N. McKinsey, arXiv:1005.0838 [astro-ph.CO] (2010).

[101] C. Savage et al., Phys.Rev. **D83** (2011), 055002.

[102] F. Bezrukov et al., Astropart.Phys. **35** (2011), 119.

[103] C. Arina, J. Hamann and Y.Y. Wong, JCAP **1109** (2011), 022.

[104] J.H. Davis et al., arXiv:1203.6823 [hep-ph] (2012).

[105] J. Collar, arXiv:1106.0653 [astro-ph.CO] (2011).

[106] J. Collar and N. Fields, arXiv:1204.3559 [astro-ph.CO] (2012).

[107] M. Farina et al., JCAP **1111** (2011), 010.

[108] S. Yellin, Phys.Rev. **D66** (2002), 032005.

[109] K. Blum, arXiv:1110.0857 [astro-ph.HE] (2011).

[110] R. Bernabei et al., arXiv:1202.4179 [astro-ph.GA] (2012).

[111] M. Kos, Talk at UCLA Dark Matter 2012, Los Angeles, February 22-24 (2012).

[112] J. Pradler, arXiv:1205.3675 [hep-ph] (2012).

[113] J.P. Ralston, arXiv:1006.5255 [hep-ph] (2010).

[114] M. Kuzniak, M. Boulay and T. Pollmann, arXiv:1203.1576 [astro-ph.IM] (2012).

[115] J. Collar, arXiv:1103.3481 [astro-ph.CO] (2011).

[116] D. Hooper et al., Phys.Rev. **D82** (2010), 123509.

[117] P. Belli et al., Phys.Rev. **D84** (2011), 055014.

[118] V. Tretyak, Astropart.Phys. **33** (2010), 40.

[119] M. Lisanti and D.N. Spergel, arXiv:1105.4166 [astro-ph.CO] (2011).

[120] M. Kuhlen, M. Lisanti and D.N. Spergel, arXiv:1202.0007 [astro-ph.GA] (2012).

[121] M. Fairbairn and T. Schwetz, JCAP **0901** (2009), 037.

[122] P.J. Fox, J. Liu and N. Weiner, Phys.Rev. **D83** (2011), 103514.

[123] E. Behnke et al., arXiv:1204.3094 [astro-ph.CO] (2012).

[124] S. Archambault et al., Phys. Lett. **B711** (2012), 153.

[125] T. Sjostrand, S. Mrenna and P.Z. Skands, Comput. Phys. Commun. **178** (2008), 852.

[126] R. Kappl and M.W. Winkler, Nucl. Phys. **B850** (2011), 505.

[127] G. Wikstrom and J. Edsjo, JCAP **0904** (2009), 009.

[128] A. Serenelli et al., Astrophys. J. **705** (2009), L123.

[129] A. Gould, Astrophys. J. **356** (1990), 302.

[130] V. Barger et al., Phys. Rev. **D76** (2007), 095008.

[131] C.H. Llewellyn Smith, Phys. Rept. **3** (1972), 261.

[132] G.L. Fogli and G. Nardulli, Nucl. Phys. **B160** (1979), 116.

[133] D. Rein and L.M. Sehgal, Annals Phys. **133** (1981), 79.

[134] H. Gallagher, Nucl. Phys. Proc. Suppl. **112** (2002), 188.

[135] G. Raffelt, G. Sigl and L. Stodolsky, Phys. Rev. Lett. **70** (1993), 2363.

[136] M. Cirelli et al., Nucl. Phys. **B727** (2005), 99.

[137] A. Strumia and F. Vissani, hep-ph/0606054 (2006).

[138] T. Schwetz, M. Tortola and J. Valle, New J.Phys. **13** (2011), 063004.

[139] F. An et al., Phys. Rev. Lett. **108** (2012), 171803.

[140] J. Ahn et al., Phys. Rev. Lett. **108** (2012), 191802.

[141] M. Blennow, J. Edsjo and T. Ohlsson, JCAP **0801** (2008), 021.

[142] V. Niro et al., Phys. Rev. **D80** (2009), 095019.

[143] Y. Fukuda et al., Nucl.Instrum.Meth. **A501** (2003), 418.

[144] C. Ishihara, Ph.D. Thesis (2010).

[145] W.B. Landsman, Astronomical Data Analysis Software and Systems II, A.S.P. Conference Series **52** (1993), 246.

[146] Y. Ashie et al., Phys. Rev. **D71** (2005), 112005.

[147] D.E. Groom, N.V. Mokhov and S.I. Striganov, Atom. Data Nucl. Data Tabl. **78** (2001), 183.

[148] M. Honda et al., Phys. Rev. **D75** (2007), 043006.

[149] R. Wendell et al., Phys. Rev. **D81** (2010), 092004.

[150] T. Tanaka, J. Phys. Conf. Ser. **136** (2008), 042087.

[151] T. Tanaka, Proceedings of the 31st ICRC, Łódź (2009).

[152] R. Kappl and M.W. Winkler, Phys.Rev. **D85** (2012), 123522.

[153] S. Orito et al., Phys. Rev. Lett. **84** (2000), 1078.

[154] T. Maeno et al., Astropart. Phys. **16** (2001), 121.

[155] Y. Asaoka et al., Phys. Rev. Lett. **88** (2002), 051101.

[156] K. Abe et al., Phys. Lett. **B670** (2008), 103.

[157] M. Aguilar et al., Phys. Rept. **366** (2002), 331.

[158] O. Adriani et al., Phys. Rev. Lett. **105** (2010), 121101.

[159] F. Donato et al., Astrophys. J. **563** (2001), 172.

[160] E. Fermi, Phys. Rev. **75** (1949), 1169.

[161] I.V. Moskalenko et al., Astrophys. J. **565** (2002), 280.

[162] Y. Shikaze et al., Astropart. Phys. **28** (2007), 154.

[163] O. Adriani et al., Science **332** (2011), 69.

[164] A. Strong and I. Moskalenko, Astrophys. J. **509** (1998), 212.

[165] L. Bergstrom, J. Edsjo and P. Ullio, Astrophys. J. **526** (1999), 215.

[166] L.C. Tan and L.K. Ng, Phys. Rev. **D26** (1982), 1179.

[167] L.C. Tan and L.K. Ng, J. Phys. **G9** (1983), 227.

[168] W. Webber and M. Potgieter, Astrophys. J. **344** (1989), 779.

[169] T. Gaisser and R. Schaefer, Astrophys. J. **394** (1992), 174.

[170] M. Simon, A. Molnar and S. Roesler, Astrophys. J. **499** (1998), 250.

[171] R.P. Duperray et al., Phys. Rev. **D68** (2003), 094017.

[172] A.N. Kalinovski, N.V. Mokhov and Y.P. Nikitin, Passage of High-Energy Particles through Matter, AIP (1989).

[173] V.S. Berezinskii et al., Astrophysics of Cosmic Rays, Elsevier Science (1990).

[174] V.S. Ptuskin et al., Astron. Astrophys. **321** (1997), 434.

[175] D. Maurin et al., astro-ph/0212111 (2002).

[176] D. Maurin, R. Taillet and F. Donato, Astron. Astrophys. **394** (2002), 1039.

[177] R.J. Protheroe, Astrophys. J. **251** (1981), 387.

[178] D. Maurin et al., Astrophys. J. **555** (2001), 585.

[179] T. Bringmann, F. Donato and R.A. Lineros, JCAP **1201** (2012), 049.

[180] M. Ackermann et al., arXiv:1205.6474 [astro-ph.CO] (2012).

[181] J. Lavalle, Phys. Rev. **D82** (2010), 081302.

[182] F. Donato et al., Phys. Rev. **D69** (2004), 063501.

[183] J.W. Bieber et al., Phys. Rev. Lett. **83** (1999), 674.

[184] S.E.S. Ferreira and M.S. Potgieter, Astrophysical J. **603** (2004), 744.

[185] L.J. Gleeson and W.I. Axford, Astrophys. J. **154** (1968), 1011.

[186] L.A. Fisk, M.A. Forman and W.I. Axford, J. Geophys. Res. **78(7)** (1973), 995.

[187] K. Sakai, Talk at ICRC 2011, Beijing, August 11-18 (2011).

[188] B. Heber et al., Astrophys. J. **699** (2009), 1956.

[189] E. Cliver, I. Richardson and A. Ling, Space Science Reviews (2010), 1.

[190] M. Ackermann et al., Phys. Rev. Lett. **107** (2011), 241302.

[191] T.R. Slatyer, N. Padmanabhan and D.P. Finkbeiner, Phys.Rev. **D80** (2009), 043526.

[192] G. Hutsi et al., Astron. Astrophys. **535** (2011), A26.

[193] S. Galli et al., Phys. Rev. **D84** (2011), 027302.

[194] L. Goodenough and D. Hooper, arXiv:0910.2998 [hep-ph] (2009).

[195] D. Hooper and L. Goodenough, Phys. Lett. **B697** (2011), 412.

[196] D. Hooper and T. Linden, Phys. Rev. **D84** (2011), 123005.

[197] J. Han et al., arXiv:1201.1003 [astro-ph.HE] (2012).

[198] D. Fixsen et al., arXiv:0901.0555 [astro-ph.CO] (2009).

[199] M. Seiffert et al., arXiv:0901.0559 [astro-ph.CO] (2009).

[200] N. Fornengo et al., Phys. Rev. Lett. **107** (2011), 271302.

[201] D. Hooper et al., arXiv:1203.3547 [astro-ph.CO] (2012).

[202] A. Boyarsky, D. Malyshev and O. Ruchayskiy, Phys. Lett. **B705** (2011), 165.

[203] M. Chernyakova et al., Astrophys. J. **726** (2011), 60.

[204] T. Vernstrom, D. Scott and J. Wall, arXiv:1102.0814 [astro-ph.CO] (2011).

[205] T. Linden, E. Lovegrove and S. Profumo, Astrophys. J. **753** (2012), 41.

[206] L. Bergstrom, Ann. Phys. **524** (2012).

[207] P.D. Serpico and G. Bertone, Phys. Rev. **D82** (2010), 063505.

[208] J. Wess and B. Zumino, Nucl. Phys. **B70** (1974), 39.

[209] CMS collaboration, CMS-PAS-HIG-12-020 (2012).

[210] ATLAS collaboration, ATLAS-CONF-2012-093 (2012).

[211] S. Weinberg, Phys.Rev. **D13** (1976), 974.

[212] J. Wess and J. Bagger, Supersymmetry and supergravity, Princeton University Press (1992).

[213] S.P. Martin, hep-ph/9709356 (1997).

[214] B.A. Campbell et al., Phys. Lett. **B256** (1991), 457.

[215] H. Goldberg, Phys. Rev. Lett. **50** (1983), 1419.

[216] J.R. Ellis et al., Nucl. Phys. **B238** (1984), 453.

[217] L. Calibbi, T. Ota and Y. Takanishi, JHEP **1107** (2011), 013.

[218] D.T. Cumberbatch et al., arXiv:1107.1604 [astro-ph.CO] (2011).

[219] L. Calibbi, T. Ota and Y. Takanishi, arXiv:1112.0219 [hep-ph] (2011).

[220] M. Drees, Int. J. Mod. Phys. **A4** (1989), 3635.

[221] S. Abel, S. Sarkar and P. White, Nucl. Phys. **B454** (1995), 663.

[222] H.M. Lee et al., Nucl. Phys. **B850** (2011), 1.

[223] S. Abel, Nucl.Phys. **B480** (1996), 55.

[224] D.E. Kaplan, G.D. Kribs and M. Schmaltz, Phys.Rev. **D62** (2000), 035010.

[225] Z. Chacko et al., JHEP **0001** (2000), 003.

[226] D. McKeen, Phys.Rev. **D79** (2009), 015007.

[227] M. Alam et al., Phys.Rev. **D40** (1989), 712.

[228] M. Iwasaki et al., Phys.Rev. **D72** (2005), 092005.

[229] A. Ali et al., Phys.Rev. **D66** (2002), 034002.

[230] A. Ali, hep-ph/0210183 (2002).

[231] V. Barger, G. Shaughnessy and B. Yencho, Phys.Rev. **D83** (2011), 055006.

[232] D. Das, U. Ellwanger and A.M. Teixeira, JHEP **1204** (2012), 067.

[233] M.M. Pavan et al., PiN Newslett. **16** (2002), 110.

[234] K. Nakamura, Int. J. Mod. Phys. **A18** (2003), 4053.

[235] A. Barrau et al., Astron. Astrophys. **388** (2002), 676.